MECHANICAL INFLUENCE OF PRESSURE, TOPOGRAPHY, AND DIFFUSION ON CELL PHYSIOLOGY AND FUNCTION

BY

CASEY LANE DYCK

THESIS

Submitted in partial fulfillment of the requirements
for the degree of Master of Science in Mechanical Engineering
in the Graduate College of the
University of Illinois at Urbana-Champaign, 2012

Urbana, Illinois

Adviser:

Professor K. Jimmy Hsia

ABSTRACT

This thesis aims to explore the effects of pressure, topography, and diffusion on cellular function and physiology. Pressure is one form of mechanical stimuli that occurs naturally within a cellular microenvironment yet is largely overlooked in day to day cell culture. Here we present two different pressurized incubation chambers which allow for the study of cells under hydrostatic pressure up to 150 psi. HepG2 cells are shown to have an altered cell cycle for pressures of 14.5 psi (100 kPa). In the second part of this thesis, the effect of topography and cellular mechanics is explored. This field of research has received a lot of attention recently using photolithography based techniques to produce nano and micro scaled topographical features. Photolithography techniques have very little control over the radius of curvature of the edges so we use a buckling substrate to create periodic topographies with controlled curvatures. The C2C12 cells used for this experiment show alignment with 2 μm features after 24 hours however no alignment with 833 nm and 417 nm features until after 48 hours. In the final part of the thesis, a cell encapsulating microvascular stamp is introduced. This stamp delivers blood vessel growth factors, via diffusion, to the target tissue in order to guide blood vessel formation in the same pattern as inscribed in the stamp. To explore the mechanics behind the diffusional growth factor delivery, a finite element model was created to simulate the process. The numerical model developed in this study will help to better understand the interactions between cells, extracellular matrix, media, and the target tissue.

ACKNOWLEDGMENTS

The author wishes to express appreciation to Professor Hsia for his guidance through this research and words of encouragement for continually learning and growing. Thanks to my girlfriend, family and friends who have helped me through the demanding process of earning my Master's Degree.

TABLE OF CONTENTS

Table of Figures v

Chapter 1: Introduction 1
1.1. Mechanical Influence on Cell Physiology and Function 1
1.2. Overview 5

Chapter 2: Cell Mechanics Using Hydrostatic Pressure 6
2.1. Scope of Research 6
2.2. Pressurized Incubation Chamber Designs 13
2.3. Materials and Methods 24
2.4. Results and Discussion 27

Chapter 3: Cellular Response to Surface topography 34
3.1. Scope of Research 34
3.2. Materials and Methods 40
3.3. Results and Discussion 44

Chapter 4: Diffusion Modeling of Hydrogel Encapsulated cells 51
4.1. Scope of Research 51
4.2. Finite Element Diffusion Modeling 53
4.3. Results and Discussion 57

Works Cited 65

Appendix A: Pressurized Incubation Chamber One FEA 72
Appendix B: Pressurized Incubation Chamber Two FEA 75
Appendix C: AFM Data Analysis Matlab Code 81

TABLE OF FIGURES

Figure 1 - Process flow diagram for PIC-1. The arrows represent the pathway for the 5% CO_2 air. 14

Figure 2 - PIC-1 inside standard incubator. Below the shelf which the pressure system is sitting on, there is room for control samples. 15

Figure 3 - Outside of VWR incubator with pump and insulated hoses going through the 1 inch access port built into the side of the incubator. 16

Figure 4 - CAD drawing of PIC-1 17

Figure 5 - Process Flow Diagram for PIC-2. Arrows represent the pathway for the 5% CO_2 air. 18

Figure 6 - Alternative PIC-2 process flow diagram for atmospheric pressure experiments. Arrows represent the pathway for the 5% CO_2 air. 19

Figure 7 - Photo of PIC-2 sitting on microscope stage. 5% CO_2 air enters from the left port and exits through the right port. Pressure gage gives accurate reading directly from inside the chamber. The RTD measures temperature inside chamber. The Heater is wrapped around the base and held firmly in place with a worm-drive clamp. 20

Figure 8 - PIC-2 installed on microscope. Temperature and flow rate controllers are located in box sitting to the left of microscope. Humidification chamber is at the very left of picture. 21

Figure 9 - CAD drawing of incubation chamber for PIC-2 22

Figure 10 - CAD drawing of humidification chamber for PIC-2. Coiled tubing connects to a through wall connection in the lid. 23

Figure 11 - CO_2 and Temperature for PIC-1 27

Figure 12 - Relative Humidity and Pressure for PIC-1 28

Figure 13 - HepG2 cell counting results. Error bars represent 1 standard deviation. 29

Figure 14 - DNA quantification for HepG2 cells 30

Figure 15 - Sample of Modfit Data analysis for 5 day pressurized sample. 31

Figure 16 - Flow Cytometry results 31

Figure 17 - Time lapse photos of HepG2 with 100 kPa of pressure 32

Figure 18 - CAD drawing of strain device 40

Figure 19 - Brightfield Image of Buckled surface. Buckled waves are parallel to the Y direction and 2 cracks can be seen parallel to the X direction. Merger Defects can be are all of the lighter colored spots throughout the image. PDMS with 10% pre-strain and 1 minute of oxygen plasma treatment at 100 Watts. Amplitude ~54 nm and wavelength ~500. 44

Figure 20 - AFM results for buckled surfaces. (A) PDMS with 10% pre-strain and 1 minute of oxygen plasma treatment at 100 Watts. Amplitude ~54 nm and wavelength ~500 nm. (B) PDMS with 25% pre-strain and 1 minutes of oxygen plasma treatment at 100 Watts. Amplitude ~25 nm and wavelength ~187 nm. 45

Figure 21 - Effect of Pre-strain amount on Wavelength and Amplitude. Error bars represent one standard deviation. 45

Figure 22 - Buckled surface Wavelength and Amplitude with Various exposure times. Error bars represent one standard deviation. 46

Figure 23 - AFM images of; (A) untreated PDMS, (B) Oxygen Plasma treated PDMS, (C) Fibronectin coated PDMS. Gray level scale bar indicates height of surface. 47

Figure 24 - C2C12 cells aligning with 2 μm waves after 24 hours. 48

Figure 25 - C2C12 cells on (A) 833 nm and (B) 417 nm waves showing no alignment after 24 hours. Scale bars are 100 μm. 48

Figure 26 - C2C12 cells on (A) 833 nm and (B) 417 nm waves showing significant alignment after 48 hours. Scale bars are 100 μm. 49

Figure 27 - 3D CAD model of microvascular stamp. 52

Figure 28 - Schematic of the Implantation of Microvascular Stamp onto CAM 52

Figure 29 - Schematic of model setup 53

Figure 30 - Model Setup 54

Figure 31 - Formation of patterned neovessels on chick chorioallantoic membrane (CAM). a) The bright field images of neovessels formed under PEGDA-MA hydrogels containing microchannels of diameters at 0 μm (a-1), 300μm (a-2), 500 μm (a-3), and 1,000 μm (a-4). The implant sites shown in (a) were further magnified in (b) (scale bars represent 500 μm). These images were captured seven days after implantation. 57

Figure 32 - Concentration of VEGF after 7 days of diffusion. Top view images show radial VEGF concentration 20 μm below the surface of the CAM. 59

Figure 33 - Plot showing the concentrations of VEGF for each microchannel size at 20 micrometers below the CAM surface after 7 days. 60

Figure 34 - Seven Day time lapse of concentrations in 500 micrometer channel. 61

Figure 35 - Vector field showing mass flow rate of diffusing VEGF. Larger arrows represent higher mass flow rate. 62

Figure 36 - Plot showing mass flow rate for all microchannel sizes at 20 micrometers below the surface of the CAM after 7 days.....63

Figure 37 - PIC-1 CAD drawing, Bill of Materials with material properties, and Exploded view. 73

Figure 38 - FEA of chamber wall for PIC-1. 74

Figure 39 - FEA of lid for PIC-1.....74

Figure 40 - CAD drawing of PIC-2 76

Figure 41 - Bill of Materials and exploded view for PIC-2 77

Figure 42 - FEA results for PIC-2 chamber wall 78

Figure 43 - FEA results for PIC-2 lid 78

Figure 44 - Dimension drawing for 316 stainless steel base. 79

Figure 45 - FEA for base and quartz view port. 79

Figure 46 - Cut through middle of base and close up of stress concentration location. 80

Figure 47 - Close up of FEA for quartz disc. 80

CHAPTER 1: INTRODUCTION

1.1. Mechanical Influence on Cell Physiology and Function

1.1.1. Framework for Mechanobiology

It has been shown that there is a very structured and active 'musculoskeletal system' within a cell called the cytoskeleton to which organelles attach and move along. [1] The cytoskeleton contains myosin molecules that are capable of exerting forces within the cell, on the cell membrane, and through the membrane to the extracellular matrix. These mechanically active connections made up of microtubules, intermediate filaments, and microfilaments run between the inner workings of a cell and the cell membrane. [2] This active relationship from the cell center to cell exterior and beyond is the framework from which the scientific field of mechanobiology has evolved.

In the early 1980's it had become widely accepted within the scientific community that intracellular cytoskeleton was linked to its extracellular environment through adhesive matrix proteins. These cell adhesions consist of multi-molecular protein complexes called focal adhesion (FA) complexes that cross through the cell membrane to adhesion receptors anchoring intracellular cytoskeletal structural proteins and signal transduction molecules. More recent advances reveal that components of cell adhesion complexes display multiple interactions and functions, which cooperate to mediate cell adhesion, migration, and signaling. [3] Cell-matrix and cell-cell adhesions can serve as both recipients and generators of signaling information, using molecular interactions regulated by aggregation, conformational changes, phosphorylation, and mechanical stimuli. [3] This framework links the nucleus to the cytoskeleton which connects to the focal adhesion molecules inside the membrane and through the membrane with integrin's, and then to the external collagen matrix itself via proteoglycans such as fibronectin. Through these connections, mechnoregulatory processes occur from the extracellular matrix (ECM) onto the cell (outside in) and from the cell onto the extracellular matrix (inside out). For better or worse, the mechanical environment of a cell affects cell function.

For nearly all types of cells, the ability to respond to mechanical stimulation in their environment is critical to their function. Therefore, an understanding of cellular mechanosensitivity is critical to the understanding of cellular processes and the requirements for successful biomedical device design at the micro and nano scale. Mechanotransduction is the process by which cells convert mechanical stimulus into electrical or chemical activity. Common mechanotransduction driven senses include touch, hearing and balance. The importance on mechanotransduction is being seen to have a role in a wide variety of diseases including asthma, osteoporosis, heart failure, atherosclerosis and stroke along with more obvious mechanical problems such as back and joint pain. [4]

One very clear instance that exemplifies the importance of mechanotransduction is in the culture of mice mammary epithelial cells. [5] Epithelial cells in general form the skin and lining of most body cavities. The cells will form in a monolayer on a specialized matrix called the basal lamina. The mammary epithelial cell produces milk in response to hormonal stimulation. However, when the cells have been removed from mice and are cultured on petri dishes, they lose their regular, cuboidal shape and the ability to make milk proteins. When laminin, the basic adhesive protein in the basal lamina, is added to the growth environment, the cells regain their usual form, organize a basal lamina, and assemble into gland-like structures capable once again of producing milk. [5] The mechanical receptors and ECM proteins communicate into the cell through integrin's to regulate cell physiology and function.

The in vivo environment of a cell includes a wide variety of mechanical signals that potentially regulate cellular mechanisms. To understand the implications of mechanical signals in everyday life, think about a simple action such as extending your arm. As the arm moves through its range of motion, the skin stretches, the extracellular matrix extends, cells distort and the interconnected molecules that makeup the internal framework of the cell feel the pull. [6] Tissue deformation can cause compression, tension, and shear strain directly onto a cell or through cell-matrix interactions. Tissue deformation can also induce fluid flow causing fluid induced shear strains and fluid

pressures. Ionic potentials across membranes can cause fluid to flow into or out of a cell creating an osmotic pressure. The way in which a cell responds to these various mechanical stimuli depends on many factors including their state at the moment and the specific makeup of the matrix. [5] Cells have many different response types. They may change shape, migrate, proliferate, differentiate, or the changes may be more subtle such as gene activity alteration. Cells are connected to and actively adapting within a responsive and changing matrix that is communicating meaningful information to the cells. The connections throughout the entire body create a network of cells and ECM which is constantly changing in response to the body's activities.

The detection of mechanical cues by a cell is highly complex and involves a system of signaling which has evolved over thousands of years. Cell signaling pathways are a part of an interconnected system of communication that governs basic cellular activities and harmonizes cell actions. [7] Cells use a large number of signaling pathways to regulate their activity. These signaling pathways fall into two main groups depending on how they are activated. Most of them are activated by external stimuli and function to transfer information from the cell surface to internal effector systems. However, some of the signaling systems respond to information generated from within the cell, usually in the form of metabolic messengers. [7] For all of these signaling pathways, information is conveyed either through adhesion complexes as discussed earlier or it is transmitted by diffusible elements. Cells often employ a number of these signaling pathways in response to a single stimulus, and this cross-talk between them is an important feature in the robust design of cell signaling. Most research in cellular mechanics point at two mechanisms responsible for cellular mechanotransduction signaling. The first being mechanosensitive channels/receptors on the lipid membrane. [8] These channels or receptors directly translate mechanical stimuli into chemical signals such as Ca^{2+} influx and the resulting kinase activation. The second mechanism is the cytoskeleton-integrin connection where the external mechanical forces are transferred through this connection to induce internal mechanical and chemical changes such as cytoskeleton reorganization, focal adhesion complex formation, and activation of a kinase cascade.

Mechanical signals combine with chemical signals to tell a cell what to do, when to do it, and how do it. Very flat cells with a stretched cytoskeleton sense that more cells are needed and that cell division is necessary. Rounding and pressure indicates that too many cells are competing for space on the matrix and those cells are proliferating too much. Growth must slow and some must die in order to prevent the formation of a tumor. In between these two extremes is where normal tissue function is established and maintained. Understanding all the mechanisms involved with this action and reaction system will lead to new approaches in cancer therapy, tissue repair, and tissue replacement.

1.1.2. Motivation for Research

The study of cellular mechanics is a fast growing research topic in recent years. Many techniques and approaches have been taken to understanding the mechanisms and tools used by cells to transduce mechanical inputs. However, many aspects of mechanobiology still elude researchers. With a mechanical engineering background, this thesis explores techniques not commonly used in cell research with the goal of shedding more light on the complicated world of cell mechanics. Hydrostatic pressure is a relatively unexplored mechanical loading mechanism in cell research. Pressurized incubation chambers have endless possibilities in research because of the simple mechanism used for applying mechanical loading to cells and because of the in vivo pressure on cells is rarely replicated for in vitro experiments. The study of surface topography impact on cell physiology has been explored extensively using the plethora of micro and nano fabrication techniques available today. While these techniques are well suited to the MEMS and Integrated circuit industry, they lack the three dimensional control necessary to truly explore the interaction that a living cell has with its topography. This thesis looks at a simple yet effect technique for creating surface topographies with controlled curvature and feature size. Finally, the use of computer modeling in biological systems is emerging as a useful tool for scientists in the prediction, optimization, and understanding of complicated processes. This thesis looks at experimental results from a cell encapsulating stamp and proposes a finite element diffusion model to help explain the directed blood vessel formation resulting from the stamp geometry.

1.2. Overview

1.2.1. Thesis Structure

This thesis is broken up into several chapters that contribute to different research approaches relating to the study of cell mechanics. Chapter 2 discusses hydrostatic pressure, its use in cellular mechanics, and the implications of mechanosensitive channels in a pressurized environment. Current research involving the use of hydrostatic pressure is reviewed and is compared to alternative mechanical stimulation methods. We discuss some of the theory behind and reasons for using hydrostatic pressure as a means for studying cellular mechanosensitivity. The design and fabrication of two distinctly different pressurized incubation chambers is reviewed and there use in these studies is covered along with the materials and procedures used for the cell culture and analysis. Finally, the results and testing of the pressure chambers is discussed. Chapter 3 explores the mechanical influence of topography on cellular function. This chapter looks at recent developments in the study of cellular mechanics using topographical influences. A novel topography fabrication technique is explored which may have several interesting future applications in the study of cell mechanics. Chapter 4 looks at a novel living microvascular stamp that has be used for direct blood vessel growth. A finite element model is created to predict the diffusive properties of the microvascular stamp. The results of the model are compared to the experimental results and implications of future modeling are discussed.

CHAPTER 2: CELL MECHANICS USING HYDROSTATIC PRESSURE

2.1. Scope of Research

2.1.1. Introduction

The cellular environment consists of complex biochemical signals and a diverse range of biomechanical influences. Cell response to variations in chemical and mechanical forces is critical in homeostasis and diseases. The mechanisms involved in molecular and biochemical responses to mechanical stimuli have been studied extensively in recent years but many aspects remain unclear. Unraveling this mystery will without doubt provide new insight into disease prevention, tissue regeneration, and overall better health. In this chapter of the thesis we will explore hydrostatic pressure as one technique used to apply controlled mechanical stress on living cells and tissues to probe mechanotransduction. Pressure is one of the main physiological stimuli naturally present in organisms. In vivo Pressure on a cell can be induced by fluids or extra cellular matrix. [9] A natural pressure even exists inside all cells due to osmosis and this pressure is what gives shape to a cell. [10] Many techniques in addition to hydrostatic pressure have been employed to study cellular mechanics and these will be briefly reviewed in the next section.

2.1.2. Techniques for Studying Mechanosensitivity of Cells

Exploration of cellular mechanics relies on the use of different methods to apply mechanical forces to living cells. Several carefully designed devices and techniques have been developed to impose these mechanical forces. There are 2 general approaches to studying cellular mechanics which every technique falls into. The first approach is to study individual cells with precisely imposed forces. Single cell assays have the advantage of being able to determine the mean response while preserving the variability of data from individual cells. [11] The second is the use of an entire culture of cells where all cells are subjected to some deformation or physical stress and then assayed as a group. These methods allow for the behavior of entire cellular systems to be evaluated using many commonly used cell biology techniques.

One example of the single cell approach is micropipette aspiration which involves using suction applied to the surface of a cell through a small glass tube while tracking the leading edge of its surface. [12] The difference in pressure across the cell membrane during the aspiration is related to its deformation. A second technique is magnetic force application where a linear force or twisting torque is applied to a particle. In magnetic twisting cytometry, a mechanical stress is applied through integrin receptors on the apical surfaces of adherent cells using RGD-coated ferromagnetic micro beads in conjunction with a magnetic twisting device. [13] A third single cell technique is optical tweezers which consist of a laser directed at a micrometer-scale object, such as beads or organelles, and is used to move the object thus creating a force. [11] Atomic force microscopy (AFM) is another technique used in probing single cells. The commercially available imaging devices use a pyramidal tip attached to a cantilever that flexes as the tip pushes into the sample surface. By measuring the deflection of the cantilever, it is possible to calculate the upwards force acting on the tip. Using AFM, the geometrical information of the surface can be obtained as well as the local stiffness of the surface. [14] Each of these techniques provide unique and important information that when looked at collectively, provides the most thorough understanding of cellular mechanics.

To study the physical response of groups of cells, techniques were developed to mimic stresses of a cells native environment. Shear stress, stretch or compression, and pressure are types of mechanical stimuli that can be applied to entire groups of cells. Shear stress is typically accomplished by flowing fluid through a flow chamber which cells have been adhered to. Flows can be steady or varying and the magnitude of the shear can be varied but is normally in the 0.1 – 2 Pascal range. [15] Stretch involves culturing adherent cells on an elastic substrate and the applying a known strain to the substrate. [16] As with shear, stretch can be constant or cyclical and strains usually range from 1% to 45%. For compression, cells may be encapsulated in a 3D collagen matrix and a direct force from and external mechanism can apply compression to the matrix which then transfers the force to the cells. [17] This approach is similar to hydrostatic pressure however; there is an intrinsic problem of non-uniform pressure because of the contact mode between the cell and the soft 3D matrix. This non-uniform compressive loading may be avoided

through the use of elevated hydrostatic pressure. The simplest method for applying this pressure is through compressed air which can be well controlled and applied cyclically or constantly. Hydrostatic pressure is naturally present in cellular environments, including cancerous tumors, and therefore is a very important aspect of cell research that needs to be better understood. [18] In the next section we will review some of the current work that has been done in this field.

2.1.3. Studies of Pressure in Cell Mechanics

In studying the effects of pressure, in vitro approaches are most commonly used because of simplicity, reliability, and controllability. In vitro experiments provide an ideal approach in which the physical stimulus can be applied to cells and the mechanism of response can be studied under precisely controlled conditions. Many naturally occurring sources of pressure can be found in cellular environments. For example, blood pressure is a well-known and medically monitored necessity for life which results in pressure on not only blood cells but also the epithelial cells which line blood vessels. Pressure will also exist in the womb during pregnancy which is caused by the stretching abdominal tissues of the mother and thus, the entire development of an unborn fetus is subject to hydrostatic pressure. Bone and cartilage experience hydrostatic fluid pressure from deformation of the extracellular matrix which acts to squeeze intercellular fluid, thus creating a cellular pressure.

Several researchers have explored the influence of hydrostatic pressure and cellular response of chondrocytes to magnitude and frequency of the applied pressure. One experiment found that intermittent hydrostatic pressure inhibited proliferation but increased collagen secretion under cyclic 200 kPa pressure with 30 minutes of load followed by 2 minutes of atmospheric pressure. In contrast, increased proliferation and decreased collagen expression was a result of 200kPa pressure with 2 minutes of load followed by 30 minutes of atmospheric pressure. [19] Others found that 10 MPa intermittent hydrostatic pressures caused increased mRNA signals compared to constant 10 MPa hydrostatic pressures. [20] The effect of frequency on mRNA signals was also explored with a significant increase in mRNA signal levels for type II collagen resulting

from 4 hours of 10 MPa loading once a day for 4 days. [21] Sulfate incorporation was shown to be significantly inhibited in cell cultures subjected to 5 MPa cyclic loading at 0.05, 0.25, and 0.5 Hz for 1.5 hours. However when these same experiments were run for 20 hours, the loading showed a stimulation of sulfate incorporation. [22]

Pressure has also been investigated in bone cells. Pressure that arises from the functional loading of bone tissue has been shown to be a critical regulator of skeletal mass and morphology. [23] Experimental results show that osteoblasts that experienced no pressure loading expressed lower levels of mRNA for type-I collagen (the main constituent of the organic phase of bone) when compared to osteoblasts exposed to cyclic pressures of 10 – 40 kPa at 1 Hz for 1 hour daily for 19 days. The pressurized cells also had an increased deposition of collagen and accumulation of calcium (one of the major components of the inorganic phase of bone). [24] Continuously applied hydrostatic pressure suppressed alkaline phosphate activity in mouse osteoblast-like cells (MC3T3-E1). This activity was quickly restored when the pressure was removed from the cells suggesting that the effect of hydrostatic pressure is reversible. [25] Intermittent hydrostatic pressure of 13 kPa at 0.3 Hz was shown to promote the osteoblastic phenotype in osteoblasts. Alkaline phosphate activity, collagen expression, and actin expression were all increased but collagen expression in osteoprogenitor cells decreased. [26] Bone marrow cells exposed to cyclic pressure of 10 – 40 kPa at 1 Hz for 1 hour a day for 7 days resulted in significantly lower osteoclastic bone resorption, lowered mRNA expression for interleukin-1 (IL-1), and lowered tumor necrosis factor-α (TNF-α). Both of which are cytokines that are known activators of osteoclast function. [27] The basic underlying theory behind all these results is that stress on bone causes fluid flow and pressure in the lacunar-canalicular system, which stimulates the osteocytes to produce factors that regulate bone metabolism. [28]

Few studies involving hydrostatic pressure have been conducted outside of bone and cartilage cells. Endothelial cells were found to be non-responsive to cyclic pressures of 10 – 40 kPa at 1 Hz but fibroblast proliferation was increased under similar test conditions. [29] However, other research showed that endothelial cells can sense and respond to physiologic levels of cyclic pressure ranging from 20 – 140 mmHg at 1 Hz by altering cell

proliferation and apoptosis. [30] Human mesenchymal progenitor cells were subjected to 5 MPa cyclical pressures and found to have no difference in DNA content and no difference in proteoglycan content. However, the same experiment found a significant increase in glycosaminoglycan content. [31] With so many different cell types and their accompanying extracellular environments, it is clear even from only a few experiments that the same level of pressure applied to different cell types will exhibit different responses. Furthermore, different levels of pressure and frequencies of pressure can also induce different responses for the same cell type. This makes the research into pressure effects essential in understanding cell mechanics as it appears that multiple mechanisms within each cell line are sensitive to different loading criteria. In the following section, we will look at cellular mechanisms associated with mechanical sensing and their relationship to pressure sensing.

2.1.4. Mechanical Force Sensing Mechanisms

It is clear from the many mechanical stimulation experiments that cells respond to mechanical forces. The next important thing to consider is how a cell responds to these mechanical forces and from the various techniques it is evident that there are a variety of mechanisms used by cells. Of these, mechanosensitive ion channels have been the most extensively studied and involve the transport of ions from the extracellular environment to the intracellular compartment. Mechanical signals can be translated to chemical signals through these mechanosensitive channels by altering the transport of ions across the cell membrane. There are 2 categories of mechanosensitive channels: mechanosensitive channel of large conductance (MscL) and mechanosensitive channel of small conductance (MscS). [8] MscL have been shown to be regulated by changes in membrane tension. This was shown by using a micropipette technique where membrane tension was controlled by the suction of the pipette and a change in conductivity across the membrane was measured in relation to the changing membrane tension. [32] Molecular dynamic simulations of MscL based on crystal structure have shown that changes in membrane tension are capable of changing pore dimension on the order of 0.5 nm. [33] Mechanical forces are essentially acting as gate keepers and thus opening and closing the ion channels.

Another method of mechanosensing is the structural change in intracellular proteins that can be a result of tension or compression. In fibronectin, many binding sites are hidden from being activated by the complex folded structure of the protein. Upon force induced lengthening, the protein will begin unfolding, therefore exposing the binding sites. [34] Many other intracellular proteins such as Src family kinases, vinculin, mDia, etc. have been identified as possible molecular switches undergoing conformational change that exposes protein binding sites in response to external forces. [35] Essentially, any extracellular matrix and cytoskeleton load bearing protein is a candidate for being a mechanosensor through unfolding mediated adhesion sites.

The well-established finding that force can lead to changes in gene expression, combined with the observation that externally applied forces also impose nuclear deformation has led to the speculation that force may directly influence DNA transcription through force mediated conformational changes in chromatin. [11] In this case, the force from an external stimulus would be transmitted to the nucleus by the cytoskeleton network. Other, more recent studies have found that the Hippo signaling pathway which is responsible for controlling organ size through cell proliferation and apoptosis is linked to cell-cell adhesion proteins. [36] Other studies have shown that external forces acting on a cell can rupture microtubules which in turn can initiate a biochemical signaling response. [37] All these mechanosensitive signaling mechanism suggests that even some of the most primal activities of cells, such as a life and death fate decision, are mediated by mechanical forces.

2.1.5. Pressure and Cell Mechanics

The scientific endeavor that is mechanobiology is relatively young despite the fact that nature has been perfecting it since the time of the earliest organisms. There are clear challenges that remain in understanding cellular mechanics. In this thesis we propose the further use of hydrostatic pressure as a means for studying cell response. Pressure is one of the main mechanical stimuli naturally present in organisms, yet it is largely overlooked in the day to day cell culture techniques used in scientific pursuits. Many of the above mentioned mechanisms may also be subject to activation by hydrostatic pressure but to

this point, research involving pressure has focused exclusively on the end results of the pressure rather than looking into how these responses were happening. The future research possibilities for hydrostatic pressure and cell culture are extensive. In the following section, the design, fabrication, and operation of 2 different pressurized incubation chambers will be covered.

2.2. Pressurized Incubation Chamber Designs

2.2.1. Design Introduction

Many commercially available incubation chambers exist for atmospheric pressure cell culture. There is however no commercially available incubation chamber designed for elevated hydrostatic pressure experiments. The basic requirement of a standard atmospheric pressure cell culture incubator is a steady 37°C temperature, high humidity, and controllable CO_2 concentration typically in the 5% - 10% range. The challenge faced during the design process was to maintain these 3 vital factors in addition to the elevated hydrostatic pressure requirement. This lead to the design and fabrication of two very different pressurized incubation systems. The first, which we will call Pressurized Incubation Chamber 1 (PIC-1), was designed to fit inside a commercially available incubator and therefore depends on the incubator for most of the control mechanisms. The second, which we will call Pressurized Incubation Chamber 2 (PIC-2), is completely independent of any commercial incubator and is designed to be mounted on a microscope for live imaging of the cells inside the chamber. The following sections will outline the design of each chamber.

2.2.2. Pressurized Incubation Chamber 1 (PIC-1)

This system takes advantage of the environmental control provided by commercially available incubators. The chamber was designed to sit inside a standard incubator using the temperature, humidity and CO_2 that is already being maintained at the desired set points. The elevated pressure is provided by a pump which sits outside of the incubator with 2 tubes attached that both lead inside the incubator. The atmospheric pressure air is withdrawn from the incubator through one tube and the pressurized air is feed into the incubator through the second tube. The pressurized air then goes through a water capture chamber to control the excess water that is present after the compression due to the high humidity content of the air before the compression. The pressurized air exits the water capture chamber and is feed through a 0.2 µm filter which performs 2 required tasks. The filter removes contaminants that could negatively affect the experimental results and contaminants that could clog the orifices of the regulators. Once the air is through the

filter it is split into 2 different paths. Part of the air goes to the reference pressure regulator (Equilibar Precision Pressure Control – Type 10 Precision Regulator 2 – 60 psig) which controls the set point for the back pressure regulator. The rest of the air enters the pressurized incubation chamber which contains the experimental specimens. The air inside the pressurized chamber is maintained at the desired pressure, humidity, temperature, and CO_2 concentration. The air inside the chamber is constantly being circulated and replaced with new air in order to maintain the desired set points. Once the air leaves the pressurized incubation chamber it passes through the back pressure regulator (Equilibar Precision Pressure Control – EB1LF1 Equilibar Back Pressure Regulator 5 – 50 psig). This back pressure regulator is responsible for maintaining the set point pressure and is manually adjusted using the reference pressure regulator discussed earlier. Beyond the back pressure regulator, the air is released back into the unpressurized incubation chamber (Figure 1).

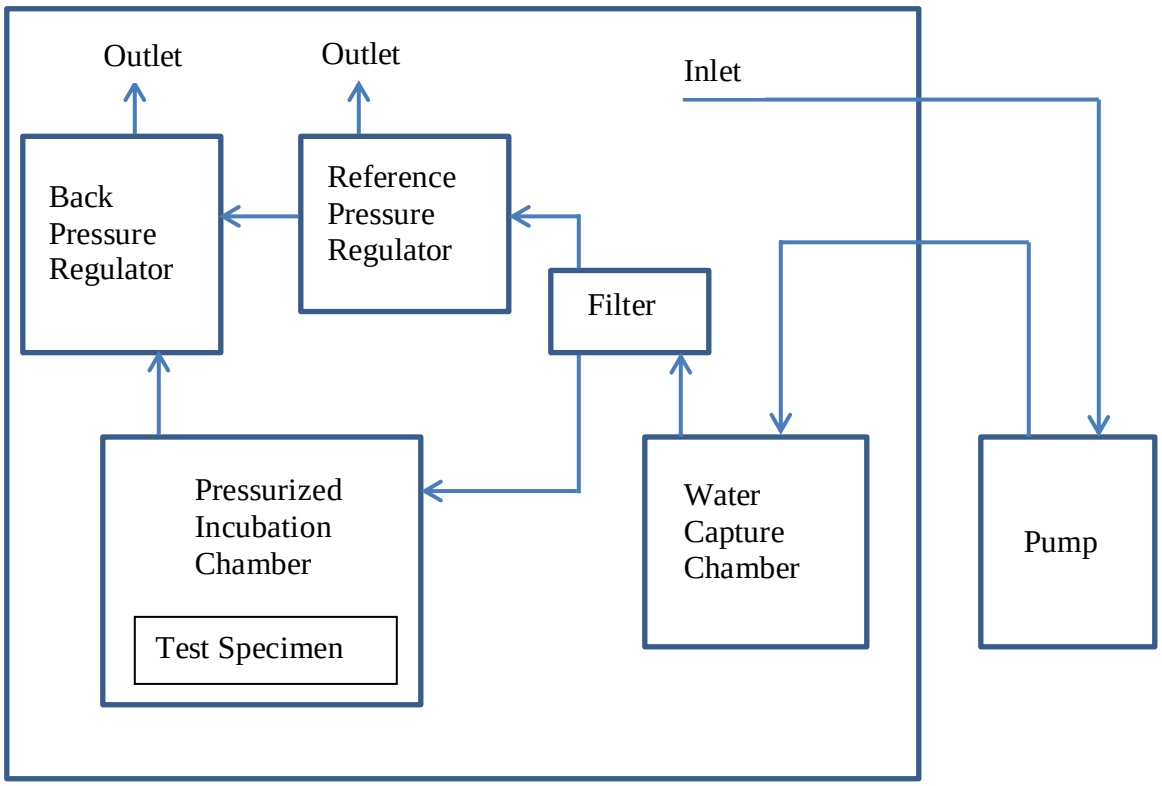

Figure 1 - Process flow diagram for PIC-1. The arrows represent the pathway for the 5% CO_2 air.

Since this chamber is dependent on a commercially available incubator, several restrictions exist that needed to be addressed in the design process. First was the size constraint of the entire system. The chambers, regulators, and tubing needed to all fit inside a standard laboratory incubator with room to spare such that during experiments, control samples could also be placed inside the same incubator but not inside the pressure chamber (Figure 2). Second design restriction was dictated by the necessity to place the pump outside of the incubation chamber because of the heat given off by running the pump long term (Figure 3). This required an incubation chamber with an access port to allow for air tubes to pass through the incubator chamber wall. The air tubes also needed to be insulted once outside the incubator in order to minimize heat loss from the air as it traveled to and from the pump. The pump was located as close to the chamber access hole as possible without having the pump on the same shelf as the incubator. The pump was not placed on the same shelf in order to minimize the vibrations that would be transferred to the incubation chamber.

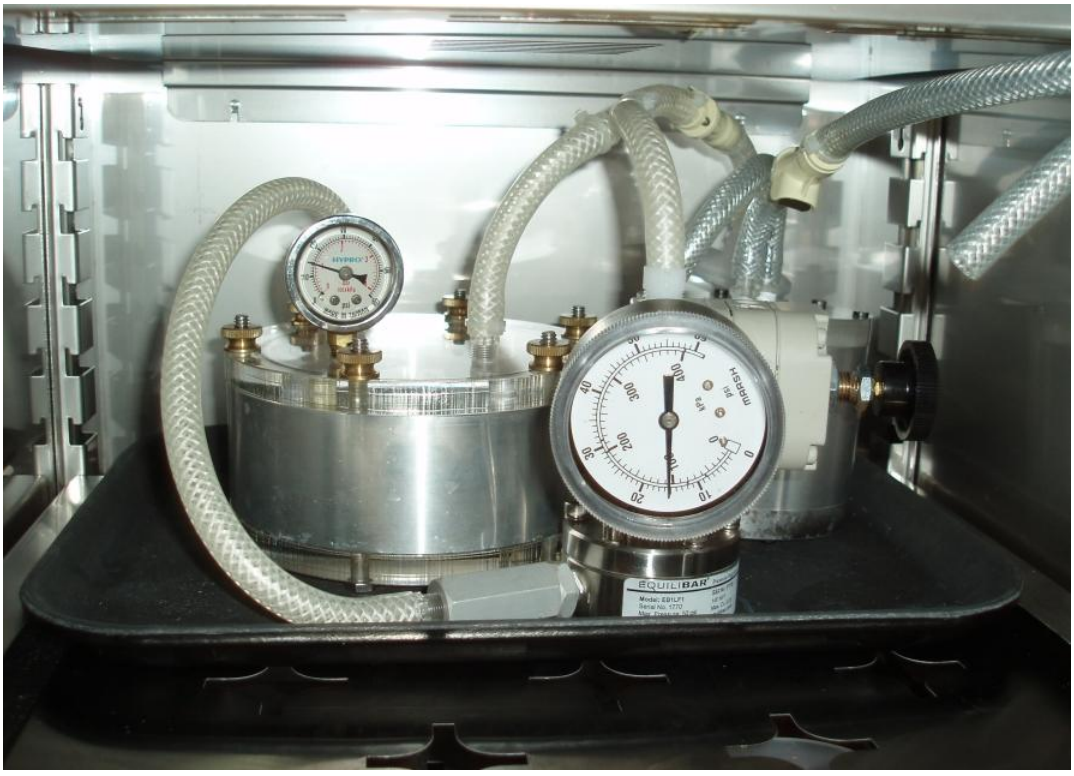

Figure 2 – PIC-1 inside standard incubator. Below the shelf which the pressure system is sitting on, there is room for control samples.

Figure 3 - Outside of VWR incubator with pump and insulated hoses going through the 1 inch access port built into the side of the incubator.

While many of the control devices were purchased, a suitable chamber could not be found. Therefore a custom fabricated chamber was needed. The main chamber wall was fabricated out of 0.75 inch thick 6061 – T6 Aluminum. The chamber lid and base were made of 0.5 inch thick cast acrylic (Figure 4). The entire chamber was held together with 6 bolts that sandwiched the assembly along with two o-rings to make it air tight. The air enters and exits the chamber through 1/8 NPT holes that have been threaded into the acrylic lid. The design was numerically simulated to withstand up to 50 psi. For a full look at the finite element analysis and design features, please refer to Appendix A.

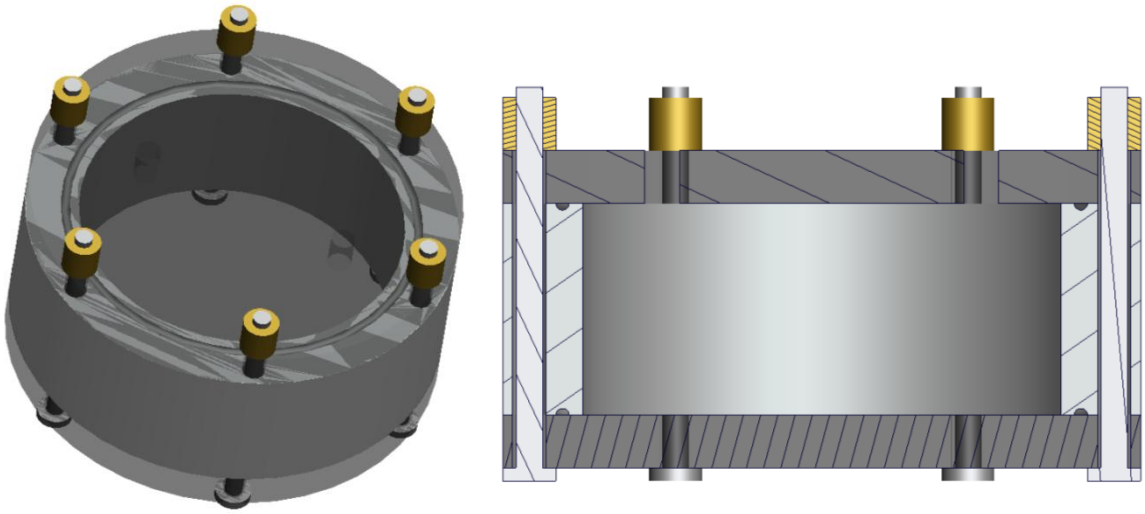

Figure 4 - CAD drawing of PIC-1

2.2.3. Pressurized Incubation Chamber 2 (PIC-2)

After the initial results from PIC-1, a desire for live imaging lead to the design of PIC-2. The major challenge with this chamber was to design it such that it fit within the constraints of a microscope and outside the controlled environment of a commercial incubator. This meant that temperature, humidity, and pressure would all need to be controlled while the 5% CO_2 air would be supplied by a pre-mixed 5% CO_2 compressed air cylinder. In addition, a view port would need to be designed such that live imaging of the pressurized cells could be executed.

The air mixture leaves the cylinder and is controlled by a two stage regulator (Air Liquide part #51-318C-CGA) which directly lowers the pressure to the desired set point for the experiment. The regulators control range is 4 – 150 psig. The air then passes through an inline miniature high pressure air filter (McMaster Carr #4414K32). Beyond the filter, the air mixture goes to the humidification and heating chamber. This chamber is filled with distilled water and acts as an initial heater for the cool dry air that comes from the gas cylinder. The air is directed to the bottom of the chamber through coiled tubing. As the air travels through the coiled tubing, it is heated by the surrounding water. The air is then deposited at the bottom of the chamber where it travels up through the water and it is humidified as it bubbles to the surface. The chamber temperature is elevated to ~37ºC by

an adhesive flexible silicone heater at 5 watts/in^2 (McMaster-Carr #35765K383). The heater is controlled by a cartridge style adjustable temperature switch (McMaster-Carr #7079K51). The pressurized, heated, and humidified air mixture now travels to the incubation chamber via an insulated tube. The incubation chamber is where the test specimens are housed. This chamber was designed to replace the insert plate of an Olympus IX2-SFR microscope stage. The chamber is heated by a low temperature heat cable (McMaster-Carr # 3597K72) wrapped around the base. This heat cable provides 10 watts of power to maintain consistent temperature within the incubation chamber. The temperature is monitored by a pipe plug resistance temperature detector (RTD) (Omega #RTD-NPT-72-E-1/8-MTP). The RTD and heater are connected to a proportional integral derivative (PID) (McMaster-Carr #3861K71) controller which measures the temperature from the RTD and adjusts the heater accordingly to maintain 37ºC. The pressurized air then leaves the incubation chamber and goes to a low flow compact flow meter (McMaster #5084K19) which maintains the desired flow rate between 0.04 – 0.42 standard cubic feet per hour. Once the air passes through the flow meter, it is released to the atmosphere (Figure 5).

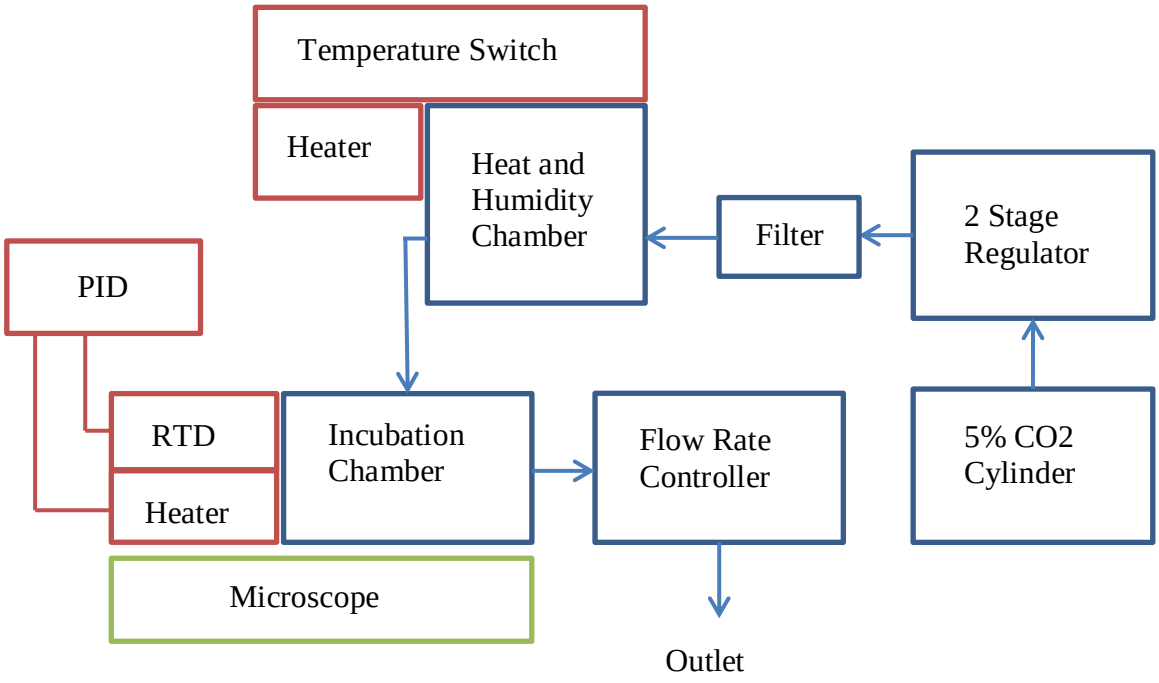

Figure 5 – Process Flow Diagram for PIC-2. Arrows represent the pathway for the 5% CO_2 air.

Alternatively, the same components can be rearranged such that the system may be used for atmospheric pressure control experiments (Figure 6).

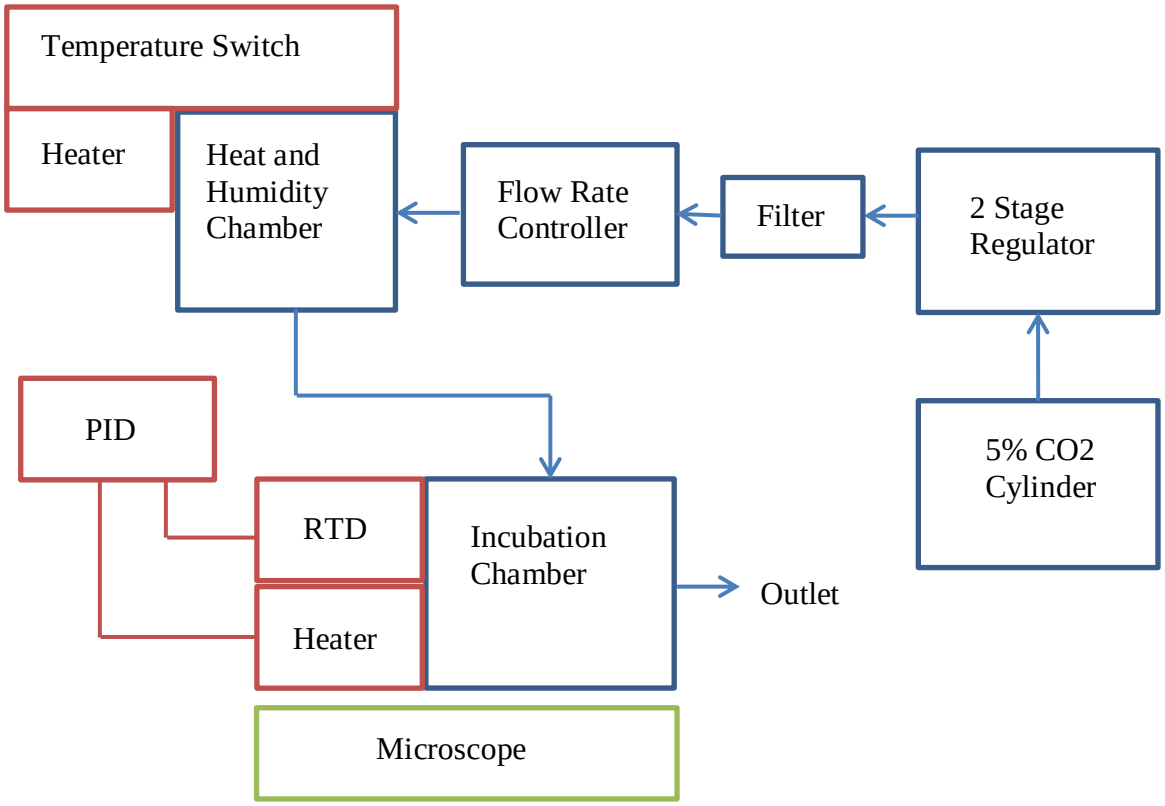

Figure 6 - Alternative PIC-2 process flow diagram for atmospheric pressure experiments. Arrows represent the pathway for the 5% CO_2 air.

PIC-2 was designed for a very specific application and as such, several of the parts including the incubation chamber and humidification chamber had to be fabricated. The incubation chamber wall was fabricated out of 0.5 inch thick 6061 – T6 Aluminum. The chamber lid was made of 0.5 inch thick cast acrylic to allow for the light source of the microscope to illuminate the sample. The chamber base was made of 316 stainless steel with a microscope viewport which was covered by a 0.125 inch thick quartz disc. The bottom plate of the chamber was held to the main body with 6 bolts that sandwiched an o-ring to make it air tight. The top plate was attached to the main body with knurled bolts that could easily be removed by hand in order to access the test specimen. There were 4 1/8 NPT ports in the side of the chamber for the RTD, pressure gage, air inlet, and air

outlet (Figure **7**). The height of the entire chamber assembly was designed to work with an Olympus IX2-MLWCD condenser which has a working distance of 1.77 inches (45mm). The microscope viewport was designed to work with the 20x Olympus objective LUCPLFLN20XPH which has a minimum working distance of 0.26 inches (6.6 mm). The design was numerically simulated to withstand up to 150 psi. The humidification chamber was fabricated out of 0.5 inch thick 6061 – T6 aluminum. The base was 0.5 in thick aluminum and the lid was 0.5 inch thick cast acrylic. The temperature switch and incoming/outgoing air ports were all installed through the lid. For a full look at the design and finite element analysis for the incubation chamber please refer to Appendix B.

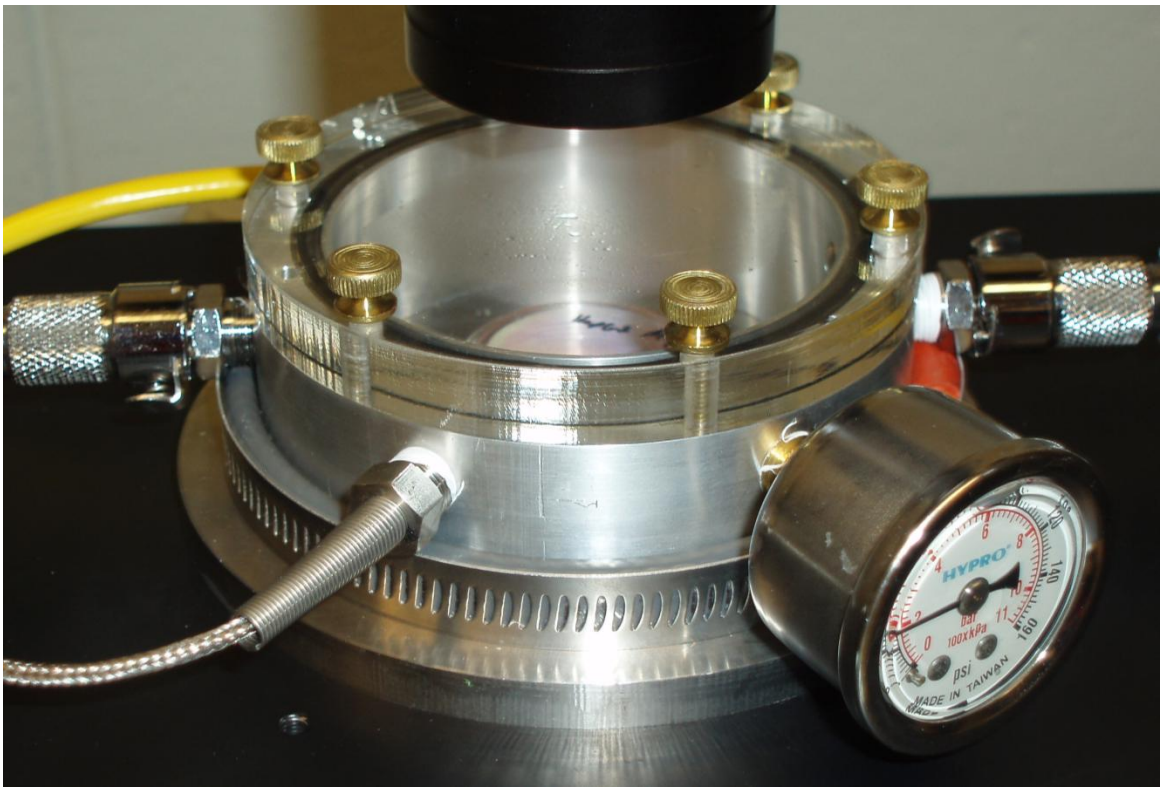

Figure 7 - Photo of PIC-2 sitting on microscope stage. 5% CO_2 air enters from the left port and exits through the right port. Pressure gage gives accurate reading directly from inside the chamber. The RTD measures temperature inside chamber. The Heater is wrapped around the base and held firmly in place with a worm-drive clamp.

Figure 8 - PIC-2 installed on microscope. Temperature and flow rate controllers are located in box sitting to the left of microscope. Humidification chamber is at the very left of picture.

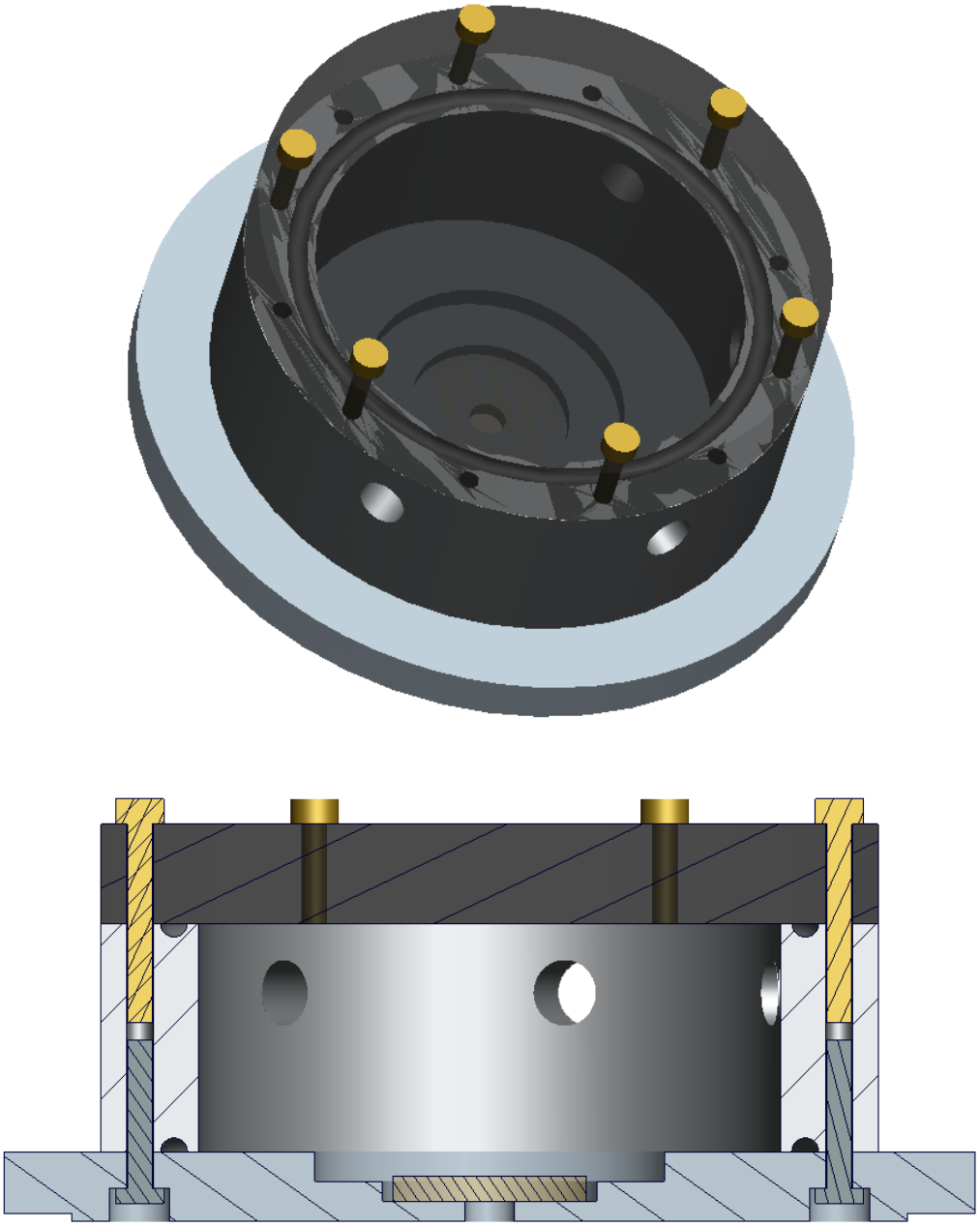

Figure 9 – CAD drawing of incubation chamber for PIC-2.

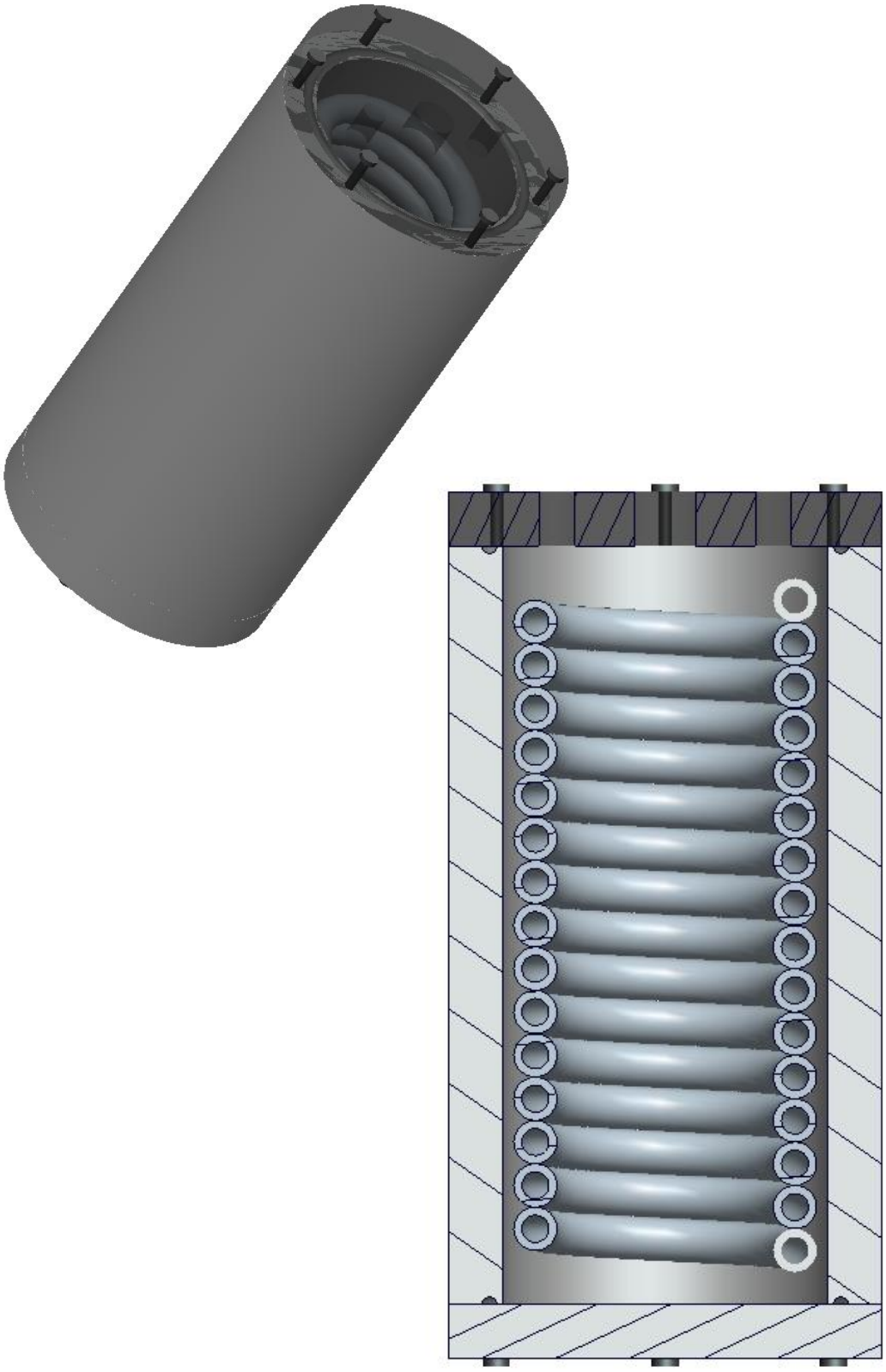

Figure 10 - CAD drawing of humidification chamber for PIC-2. Coiled tubing connects to a through wall connection in the lid.

2.3. Materials and Methods

2.3.1. HepG2 cells

Cells were received from Professor Kong at the University of Illinois at Urbana-Champaign. HepG2 are adherent, epithelial-like cells growing as monolayers and in small clusters. The HepG2 cell line was derived from the liver tissue of fifteen year old male with differentiated hepatocellular carcinoma. [38]

2.3.2. HepG2 Cell Culture

Cells were cultured using Eagle's Minimum Essential Medium (DMEM) supplemented with 10% Fetal Bovine Serum (FBS) and 1% Penicillin Streptomycin (Pen/Strep). Media was changed every 2-3 days depending on cell concentration. To passage cells, the cell monolayer is rinsed briefly with 1 x Phosphate Buffer Saline (PBS) and then incubated with pre-warmed (37°C) 0.05% Trypsin-EDTA solution for 5 - 7 minutes. Once the cell layer is detached from culture surface, the Trypsin is deactivated by adding equal volume of culture media. The cell suspension is transferred to a 15ml centrifuge tube and separated by centrifuging for 5 minutes at 500g. The supernatant is discarded and the pellet is re-suspended in culture media. Cells were split 1:4 every 3 - 4 days. Cultures were incubated at 37°C in humidified atmosphere with 5% CO_2.

2.3.3. HepG2 Cryo Preservation

HepG2 cells were cultured in 100mm petri dishes and allowed to grow to about 80% confluence. Culture plate was rinsed with 1 x PBS and then incubated with pre-warmed 0.05% Trypsin-EDTA for 5-7 minutes or until cells have detached from surface. Trypsin is deactivated by adding equal volume of culture media. The cell suspension is transferred to a 15ml centrifuge tube and separated by centrifuging for 5 minutes at 500g. The supernatant is discarded and the pellet is re-suspended in 950 µl and transferred to a cryo vial. Immediately before freezing, 50 µl of Dimethyl sulfoxide (DMSO) was added to the cell suspension. Initial freezing is done at -80°C for 24 hours and then transferred to liquid nitrogen (-196 °C) for long term storage.

2.3.4. Cell Counting

The purpose of this procedure is to determine the number of cells in a pressurized culture as compared to an atmospheric culture. About 290,000 cells were plated onto 18 – 35mm cell culture petri dishes using procedures described in section 2.3.2. All dishes were incubated for 1 day at atmospheric pressure to ensure cells had adhered to the dishes. 9 petri dishes were put into PIC-1 and the remaining 9 dishes were put into the same incubator but not inside PIC-1. Atmospheric control cells and pressure treated cells were counted after 3, 5, and 7 days. Culture media was changed every 2 days.

To count the cells, the cell monolayer is rinsed briefly with 1 x PBS and then incubated with 1 ml of pre-warmed (37°C) 0.05% Trypsin-EDTA solution for 5 - 7 minutes. Once the cell layer is detached from culture surface, the Trypsin is deactivated by adding equal volume of culture media and completely re-suspending the cells. 10 µl of the cell suspension is then added to the hemacytometer and the 4 corner squares were counted. Each square of the hemacytometer (with cover slip in place) represents a total volume of 0.1 mm^3 or 10^{-4} cm^3. Since 1 cm^3 is equivalent to 1 ml, the subsequent number of cells per culture dish is calculated.

2.3.5. Total DNA analysis

Total DNA analysis is performed in 96 well culture plates. In order for a plate to fit inside PIC-1, it must be cut in half. One half of the plate is placed in the pressure chamber and the other half is placed in the same incubator but not in the pressure chamber to act as a control sample. Once ready for analysis, the 2 halves of the plate are glued back together using a glass slide to support the plate. A fluorescence buffer consisting of 10mM Tris-HCl (pH 7.4), 1 mM EDTA, and 0.2 M NaCl is prepared in advance. The fluorescent solution of Bisbenzimide (Hoechst 33258) (0.2mg/ml stock) is prepared in advance and maintained at 4ºC and in a dark container. Once the experimental specimen is ready for processing, remove media and wash each well twice with PBS. Add 150µl DI water in washed wells to lyze cells. Freeze and thaw plate three times at -20ºC to further disrupt cell membrane and to release DNA from cell. In a clean test tube, prepare diluted bisbenzimide solution with 29µl DI water, 20µl fluorescence buffer, and 1 µl

bisbenzimide for each well. Add 50µl of solution to contents of each well and incubate for 30 minutes in the dark. Determine fluorescence with microplate reader: 356 nm excitation and 470 nm emission.

2.3.6. Flow Cytometry

Cells were prepared for flow cytometry according to the protocol laid out by Guava Technologies for specimen analysis using a Guava Personal Cell Analysis system. For full details on the protocol, please refer to Guava Technologies website [39]. The steps will be briefly outlined below.

Using trypsin as described above, remove cells from culture surface and obtain a cell suspension in a 15 ml centrifuge tube. Centrifuge the tube at 450 x g for 5 minutes. Remove and discard the supernatant. Add 10 ml of 1X PBS to each tube. Mix the cell sample by pipetting repeatedly to ensure a homogenous suspension. Centrifuge the tube at 450 x g for 5 minutes. Remove and discard the supernatant leaving approximately 500 µL of 1X PBS. Re-suspend the cells in the residual 1X PBS and add 10 ml of ice cold 70% ethanol. Refrigerate the cell preparation for at least 12 hours prior to staining.

After the minimum 12 hour wait, the cells are ready to be stained. Warm the cell cycle staining reagent (Guava Cell Cycle Reagent #4500-0220) to room temperature; shield from excessive light exposure. Centrifuge the ethanol fixed cells at 450 x g for 5 minutes. Remove and discard the supernatant being careful not to touch the pellet. Re-suspend the cells in 1 ml of 1X PBS. Let the cells stand at room temperature for one minute. Centrifuge at 450 x g for 5 minutes. Remove and discard the supernatant being careful not to touch the pellet. Add 200 µL of Cell Cycle Staining Reagent to each tube. Mix by pipetting up and down several times. Incubate at room temperature shielding away from light for 30 minutes. Acquire the sample on the Guava PCA system using the cell cycle analysis program. Photo multiplier voltage was set at 620 with a forward scatter gain of 8 and threshold of 50. The flow rate was set at 0.12 µl/s. Data was exported as an FCS file for analysis using Modfit software.

2.4. Results and Discussion

2.4.1. Chamber Measurement and Testing

The first step for the pressurized incubation chambers is to measure and calibrate the systems such that the appropriate temperature, CO_2, humidity, and pressure are maintained consistently through an experiment. To verify these parameters a CO_2, temperature, and humidity meter was purchased (co2meter.com #CM-0017). The measurement device was taking all measurements from the air immediately after it exited the pressure chamber and before it was released back into the commercial incubator. Pressure was manually verified with hourly checks of the pressure gage mounted directly to the chamber. Test results for PIC-1 can be seen in Figure 11 and Figure 12. The control parameters were quick to stabilize and very consistent for the duration of the test experiment. The approximately 15 minute stabilization period for the CO_2 and temperature is largely due to the commercial incubator stabilizing after the door had been opened to insert the pressure chamber and measurement device.

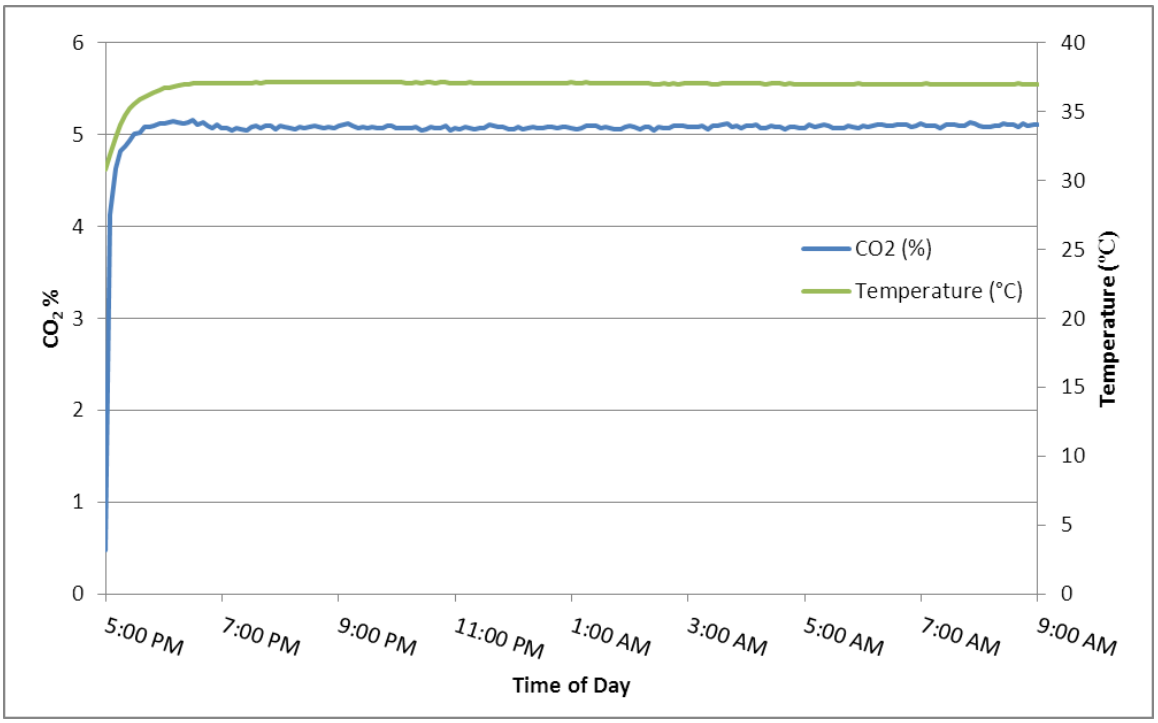

Figure 11 - CO_2 and Temperature for PIC-1

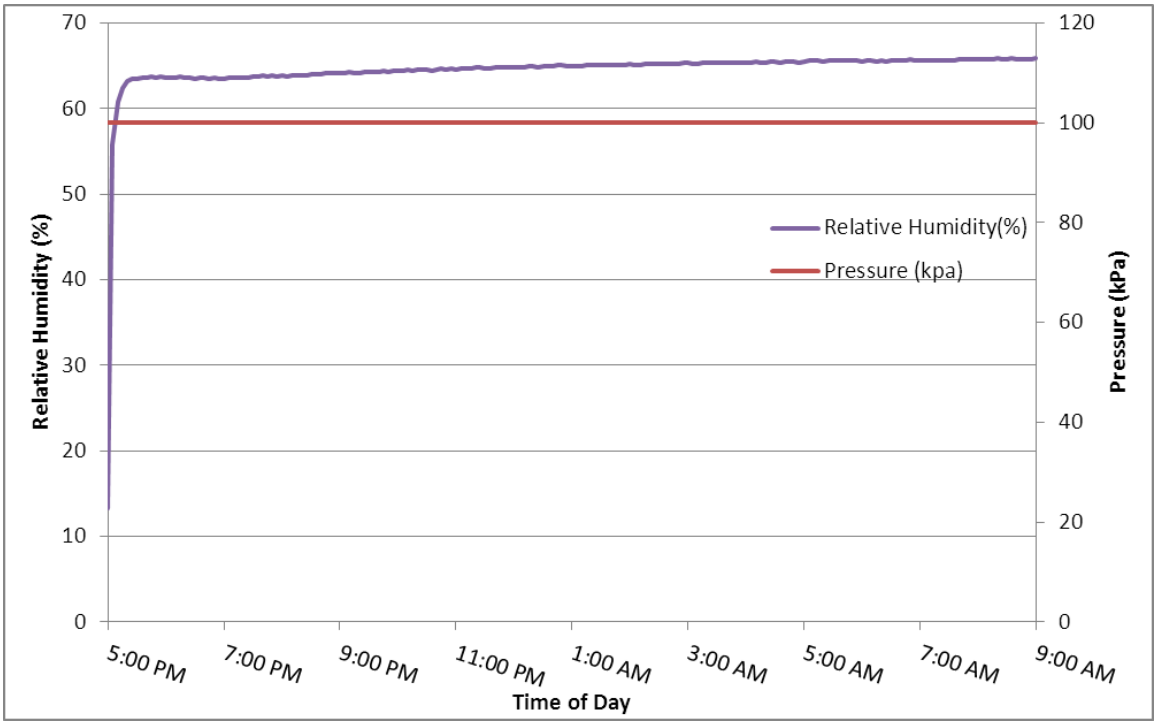

Figure 12 - Relative Humidity and Pressure for PIC-1

PIC-2 was slightly more complicated to measure the control variables because of the more exposed and less controlled environment. The 5% CO_2 was supplied by a cylinder of the same mixture which comes certified as such from the supplier. Measurements from our own CO_2 meter also confirmed the 5% CO_2 was accurate. Pressure was once again confirmed by frequently checking the pressure gage installed directly on the chamber. Temperature could not be measured at the output from the chamber in this case because the air had to first pass through the flow meter and tubing before being exhausted so any measured temperature would have been altered by the further distance that the air had to travel. Therefore, a thermocouple was used to measure the temperature of water which was in a petri dish inside the chamber. The chamber was pre-warmed for 1 hour and then was run for 6 hours and the temperature checked every 30 minutes. The temperature of the water was 36.9ºC ± 0.1ºC. Humidity for PIC-2 has not been accurately measured because the air begins cooling instantly once it leaves the chamber and condenses inside some of the tubes meaning that any measurement at the outlet is skewed by this condensation. The most important thing is that there is sufficient humidity such that culture media does not evaporate and this has not been a problem with PIC-2.

2.4.2. Cell Counting

Cell counting was used to see if there is a direct proliferation response of HepG2 cells due to the application of hydrostatic pressure. The cells were allowed one day to adhere to the culture plate under atmospheric pressure before being subjected to 100 kPa pressure. After 3 days of pressure, there is no difference in cell number between the pressurized and unpressurized. At 5 days and 7 days, a statistically significant difference is seen (Figure 13). This suggests that the cellular response to hydrostatic pressure may be a very slow mechanism.

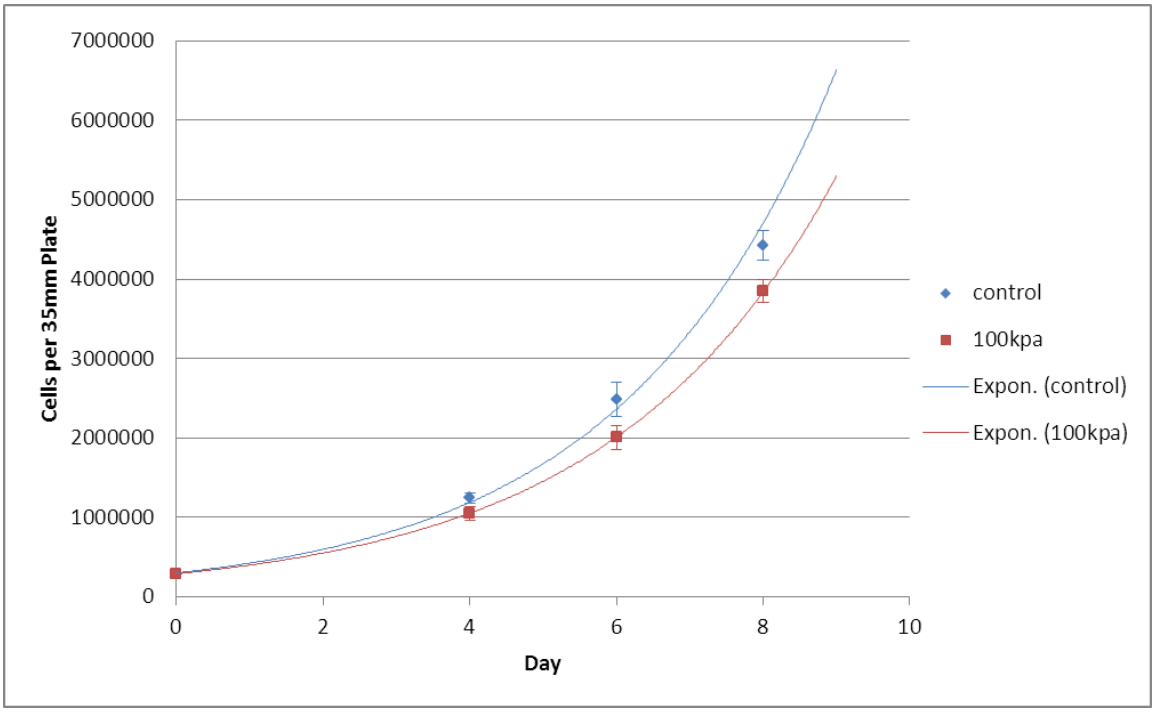

Figure 13 - HepG2 cell counting results. Error bars represent 1 standard deviation.

2.4.3. DNA Analysis

Another commonly used approach for determining cell proliferation is through DNA quantification. The DNA results show no difference between the pressurized and atmospheric pressure cells for any time point (Figure 14). This, together with the counting results suggests that some cells are becoming polyploidy. Polyploidy is the genomic condition in which cells have a raised number of chromosomes. It is been found to occur during evolution, development, cellular stress and disease. [40] The DNA is the same with

or without pressure so it is fair to say that the DNA synthesis is unaffected by pressure. Since the amount of DNA is the same but the number of cells is lower, it is assumed that the pressure is somehow affecting the HepG2 cells ability to divide.

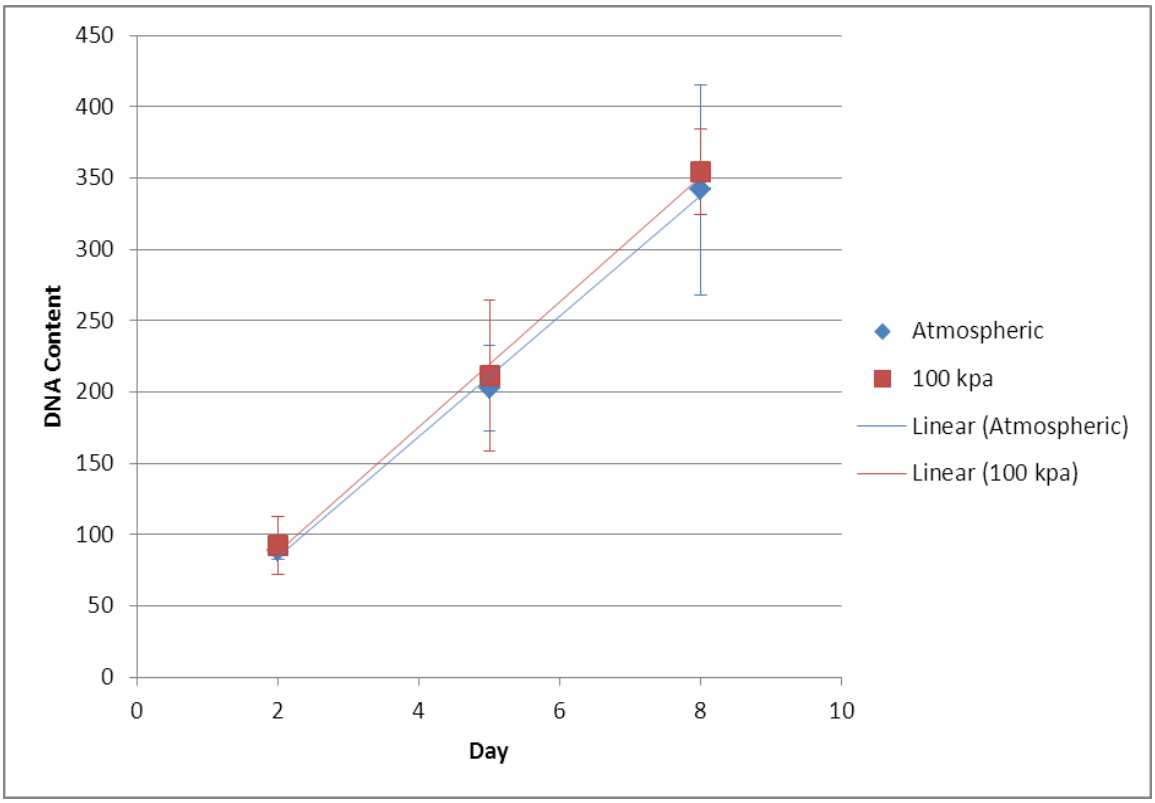

Figure 14 - DNA quantification for HepG2 cells

2.4.4. Flow Cytometry

Flow was performed for HepG2 cells after 2 days of pressure and after 5 days of pressure and the results were compared to atmospheric control cell cultures. The flow cytometry data was evaluated using Modfit as seen in Figure 15. Both the 2 day and 5 day pressure experiments show the same trend with a lower number of cells in the G1 phase and higher number of cells in the S phase as compared to the atmospheric conditions (Figure 16). This supports the evidence from the cell counting and DNA quantification because the cells seem to be getting stuck in the S phase of the cell cycle where the DNA is being replicated.

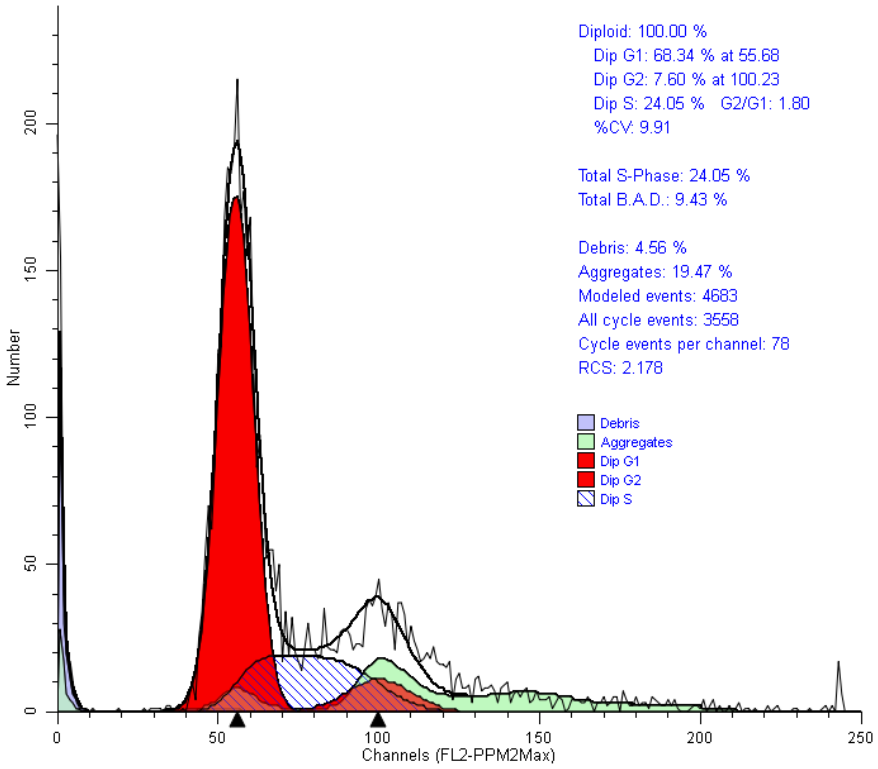

Figure 15 - Sample of Modfit Data analysis for 5 day pressurized sample.

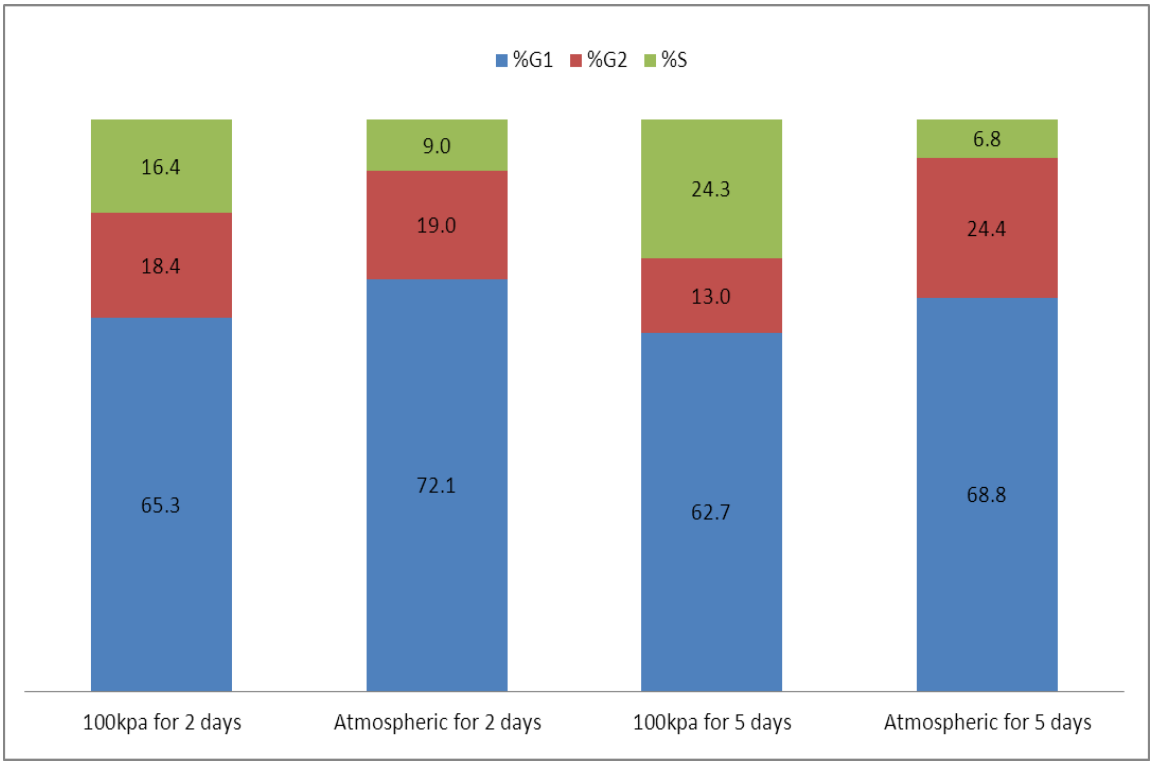

Figure 16 - Flow Cytometry results

2.4.5. Live Imaging

Using PIC-2, live imaging of HepG2 cells under 100kpa of hydrostatic pressure was carried out. Unfortunately, due to the cell type, the cell division and growth events are largely hidden inside the large clusters that the HepG2 grow in (Figure 17).

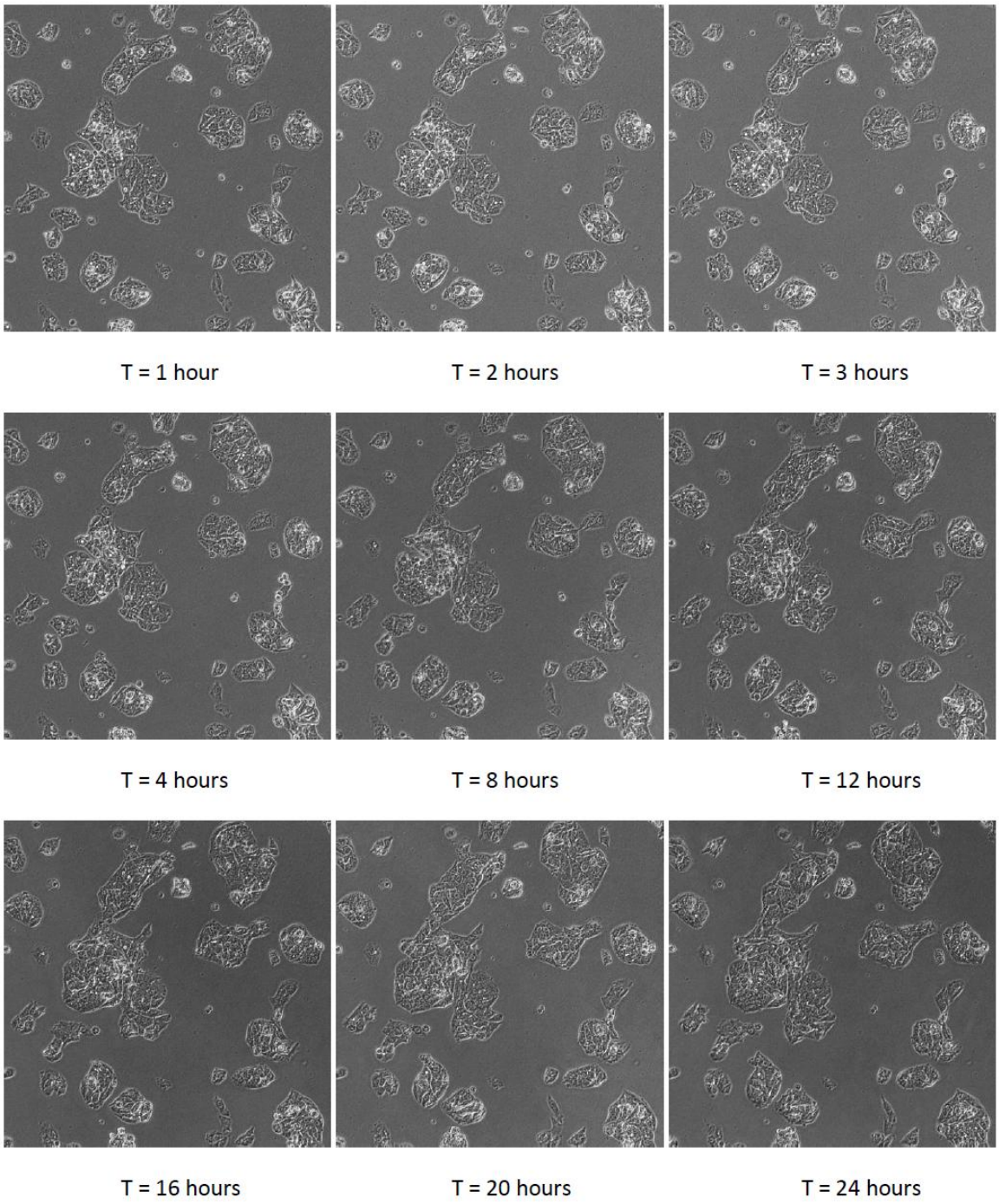

Figure 17 - Time lapse photos of HepG2 with 100 kPa of pressure

2.4.6. Conclusions

Hydrostatic pressure is a mechanical stimulus that is present naturally in cellular environments and therefore should not be overlooked when studying cell mechanics. The presented pressurized incubation chambers provide simple, tunable methods for studying cells exposed to hydrostatic pressure. PIC-1 provides a system with a larger specimen volume capacity and is therefore appropriate for long term experiments requiring larger samples. PIC-2 provides a system that works in tandem with Olympus microscopes and can be used for higher pressure experiments of up to 150 psi and for live microscope imaging.

Several previous experiments have shown some cellular responses to cyclical hydrostatic pressure but, the HepG2 experiments shown above are some of the first hydrostatic pressure studies to show that cells have a response to steady pressure. These initial results show that cell cycle is altered by 100 kPa pressure in as little as 2 days. With the counting, DNA quantification, and flow cytometry results all provide evidence that the pressure is causing polyploidy cells to form. The likely reason for this is that the hydrostatic pressure acting on the cell membrane is making it more difficult for the cells to divide.

2.4.7. Future Work

While the above work suggests that the cell cycle is being impacted simply by the physical forces preventing cell division, it is also highly likely that there are other mechanosensitive cellular responses being activated by this pressure. A major step in the study of pressure in cell mechanics is going to require concrete evidence of mechanosensitive channels or some other mechanosensitive pathway being activated by pressure. Thus far research has pressure related research has focused solely on the outcomes of pressure and the next step in this field of study is going to have to figure out the mechanism behind these response. Future work in this field will involve couple pressure experiments with stem cell research, biomaterial research, and 3 dimensional cell culture techniques.

CHAPTER 3: CELLULAR RESPONSE TO SURFACE TOPOGRAPHY

3.1. Scope of Research

3.1.1. Introduction

Unlike chapter 2 where we looked at applying external physical forces to cells, in this chapter we will impose physical constraints on cells by altering their mechanical environment. In the body, cells encounter an environment filled with signals, including topographical cues, in the form of the physical features of their surrounding extra cellular environment. In plating cells on an artificial topography the cells may respond by promoting adhesion, spreading, alignment, morphological changes, or changes in gene expression. An increased appreciation for, and understanding of, cellular responses to topographical cues may have implications in fields ranging from developmental biology to regenerative medicine. In this part of the thesis, we look at an innovative technique to produce nano and micro scale topography with unique shape characteristics. Using simple lab techniques involving PDMS, oxygen plasma, and a straining device we can fabricated anisotropic topography for cell studies. In the following section we will start by reviewing work that has been performed in this field of study.

3.1.2. Studying Cells using Topography

Substrate topography is a noninvasive and non-biological method for stimulating cellular response because the textured surfaces offer unique extracellular physical interactions without involving biomolecules. One pioneering experiment that exemplifies the importance of cell-substrate interaction is where scientists developed a technique to engineer cell shape and function using patterned adhesion molecules. They forced living cells to take on different shapes – spherical or flattened, round or square – by culturing them on adhesive islands. [5] Each island was surrounded by a surface that the cells could not adhere too. They found that by modifying the shape of the cell, they could switch the cells genetic program. Cells that were on larger islands were stretched and spread flat making them more likely to divide. Cells on small islands were prevented from spreading and formed a rounded shape. This led the cells to apoptosis. When cells were neither too

expanded nor constrained they would differentiate in a tissue specific manner. [5] The necessity for a better understanding of cell-matrix interactions has been a driving force behind topographical studies. The extracellular matrixes of various tissues are composed of complex mixtures of nano scale pits, pores, protrusions, striations, particulates, and fibers. [41] In exploring the cellular response to surface topography, two main categories of topography have become prominent: 1) Isotropic topography such as evenly or randomly distributed pits or protrusions, 2) Anisotropic such as ridges and grooves.

With isotropic patterns it is expected that the cells would show no directional order so for this classification of patterns it is more common to explore the collective cell function rather than individual cell response. The scale of the topography is a major determining factor in the type of cellular response, therefore precise control of the feature size is critical in understanding the outcome. Researchers found that fibroblasts grown on 2 µm and 5 µm protrusion arrays showed increased rates of proliferation and cell density as compared with same sized wells. In contrast, the 10 µm protrusions and wells did not prove to be statistically different from traditional smooth culture surfaces. [42] Human connective tissue progenitor cells were shown to have greater proliferation when cultured on PDMS with protrusions ranging from 5 µm to 40 µm when compared to smooth surface control conditions. [43] Other cell experiments even suggest nano scale sensitivity with human bone marrow cells. These osteoprogenitor populations showed that the nano topographies allowed control of cell adhesion, cytoskeleton, growth and production of the osteoblastic markers osteocalcin and osteopontin. [44] In addition to feature size, the spacing of these features has been shown to influence cell spreading, migration, and focal adhesion dynamics. Nano-patterned surfaces were fabricated which contained adherent gold dots, surrounded by non-adherent gaps. By varying the spacing between the dots, the clustering of the associated integrin binding sites was modulated. They showed that the formation of stable focal adhesions and persistent spreading is sensitive to pattern density. Thus cells plated with 108nm spacing between gold dots showed delayed spreading with repeated protrusion and retraction cycles compared to cells plated with 58nm spacing. [45] These studies have shown that cells have distinct responses to well defined surface topographies which have been fabricated using lithography techniques.

Other fabrication methods have also been explored which produced micron scale surface topographies in randomly generated patterns. Surface topography may be formed through sandblasting, grinding, or polishing. Studies exploring cellular response to surfaces created using these techniques have shown better osteoblastic adhesion, gene expression, and mineral deposition as a result of the micron scale topography. [46] [47] Nanometer scale surface roughness designed to mimic the roughness of bone has been shown to increase osteoblast function of human osteoblasts. [48] Micro and nano textured surfaces can induce positive stimulations in collective cell function and is therefore a promising method for exploring cellular mechanics and for cell interfacing biomedical technologies. Many different approaches have been explored with regards to isotropic topographies and results have been varied depending on feature size, feature density, and cell type.

Cellular response to anisotropic micro and nano topography has also been extensively studied. In general, cells cultured on anisotropic gratings exhibit lower proliferation rates than cells cultured on planar substrates. [49] Cell polarization, spreading, and migration along anisotropic ridges and grooves have been observed. [50] This is visible because of an elongated cell shape parallel to the direction of the topography and a cytoskeleton directional organization. Orientation in actin filaments or microtubules was identified as the first and primary cellular response event in contact guided cell alignment. [51] [52] As with isotropic topography, the scale of the features plays an important role in deciding cell alignment. Cell alignment generally increases with larger groove or ridge dimensions however if the spacing between features becomes too large as compared to the cell size, then a cell will only sense each feature as an individual topographical element. [53] Others have found that human corneal epithelial cells elongated and aligned along patterns of grooves and ridges with feature dimensions as small as 70 nm in width, 600 nm in depth and a spacing of 400 nm. [54] In the same experiment, it was determined that groove and ridge depth was the most prominent dimension in affecting cell alignment. Axonal outgrowth was observed to align on 100 nm to 400 nm wide nano imprinted grooves with a depth of 300 nm. The nerve cell processes were preferentially observed on ridge edges and elevations rather than in grooves. [55]

In addition to the alignment of cells with topographical features, another observed response dependent on feature size is if a cell bridges between two features or conforms to a single feature. The general trend is that increasing groove depth and decreasing groove width will cause cells to bridge without descending into the grooves. Epithelial cells cultured on a surface with grooves that are 150 nm deep and 2.1 μm wide would descend into the grooves. In the same experiment, with grooves less than 950 nm wide, the cells would form bridges over the grooves. [54] Other researchers who have observed the same bridging effect suggest that this is due to the membrane bending requirements being energetically unfavorable for smaller groves. [56]

In addition to the more obvious changes to cell shape and motility, gene expression and differentiation have also been explored. Fibroblast cells cultured on V-shape grooved surfaces were significantly elongated and orientated along the grooves of the substrate Further analysis revealed that on a per cell basis the grooved surface increased the amounts of fibronectin mRNA while the mRNA levels of gene glyceraldehyde-3-phosphate dehydrogenase (GAPD) were constant. The amount of secreted fibronectin on the grooved surface was also increased. [57] In fibroblasts cultured on grooves 12.5 μm wide and 2 μm deep, several genes involved with cell signaling, cytoskeleton, transcription and translation have shown to be increased after 24 hours but then down regulated after 5 days. [58] Human mesenchymal stem cells cultured on 350 nm gratings showed decreased expression of several integrin subunits when compared to control cells on un-patterned surfaces. This suggests that nano scale topography may be important in the organization of cytoskeleton, focal adhesions and thus stem cell differentiation. [59]

Anisotropic topographies induce noticeable morphological changes in cellular shape, cytoskeleton, and adhesions in addition to more subtle changes in gene expression. The mechanisms which cells use for these signaling responses to topography are still largely not understood. One proposed mechanism involves the same mechanosensitive channels introduced in chapter 2. A mechanosensitive channel embedded in the membrane of a cell is subject to tension and compression due to membrane bending. Therefore when a cell feels a topographical feature the resulting membrane deformation from cell-feature

contact may activate certain mechanosensitive channels and therefore trigger a response. Topography research to this point has been using photolithography techniques to producing nano scaled features. The major limitation of these techniques is that all of the features have sharp edges and the effect of the edge curvature has yet to be explored. In this part of the thesis we begin to look at a simple fabrication technique for producing nano scale features with varying curvature.

3.1.3. Micro and Nano Pattern Fabrication

Photolithography uses a light source to transfer a geometric pattern from a photomask onto a photosensitive material. This technique provides almost unlimited control and complexity for a prescribed pattern in 2 dimensions; however the major drawback is that the control of the 3rd dimension is limited. In order to explore the effects of curvature on cellular response, a technique of controlled thin film buckling is used to form surfaces with isotopic topography having controlled curvatures. Thin film buckling has been around for a long time but until recently it has always been considered a defect or problem that scientists have attempted to avoid. For example, the wrinkling of human skin happens because of the stiff epidermis on top of the soft dermis. When a deformation of the skin takes place, the 2 layers want to deform differently, however they are connected and any deformation that happens must satisfy the balance between them resulting in a buckled or wrinkled surface. In computer electronics, low dielectric constant polymers are being studying as inter-level dielectrics for on-chip interconnects and the deposition of thin film metals on these polymers resulted in unwanted buckling. [60]

More recently, researchers have started to use this spontaneous phenomenon as a novel nonconventional strategy to fabricate microstructure patterns. The formation of complex, ordered structures induced by the buckling of thin metal films owing to thermal contraction of an underlying substrate was shown to be well controllable. [61] The use of PDMS as the substrate and the growth of a stiff oxide layer using oxygen plasma treatment also lead to a buckled surface through thermal contraction of the substrate causing compressive force on the thin film. [62] [63] For a better controlled isotropic buckled surface, it is necessary to use a straining device to provide uniaxial pre-strain before the

oxygen plasma treatment. [64] This combination of pre-strain and an oxygen plasma grown oxide layer provides controllable, anisotropic buckling making it ideal for cellular mechanics and topography research.

3.2. Materials and Methods

3.2.1. Straining Device

A simple linear straining device (Figure 18) was needed to pre-strain the PDMS samples while they were being treated with oxygen plasma. The basic requirements were a controllable linear motion, a clamp to tightly hold specimens, and small enough to fit inside the plasma chamber. The linear motion was controlled by an acme threaded rod (McMaster Carr #99030A316) which gave the sliding clamp a travel of 0.25 inches per turn. The body was constructed of 0.5 inch thick 6061 – T6 aluminum. Bearings (McMaster Carr #60355K702) were used on both ends of the acme threaded rod to ensure smooth operation and to minimize the slop in the straining device to ensure accurate and repeatable strains.

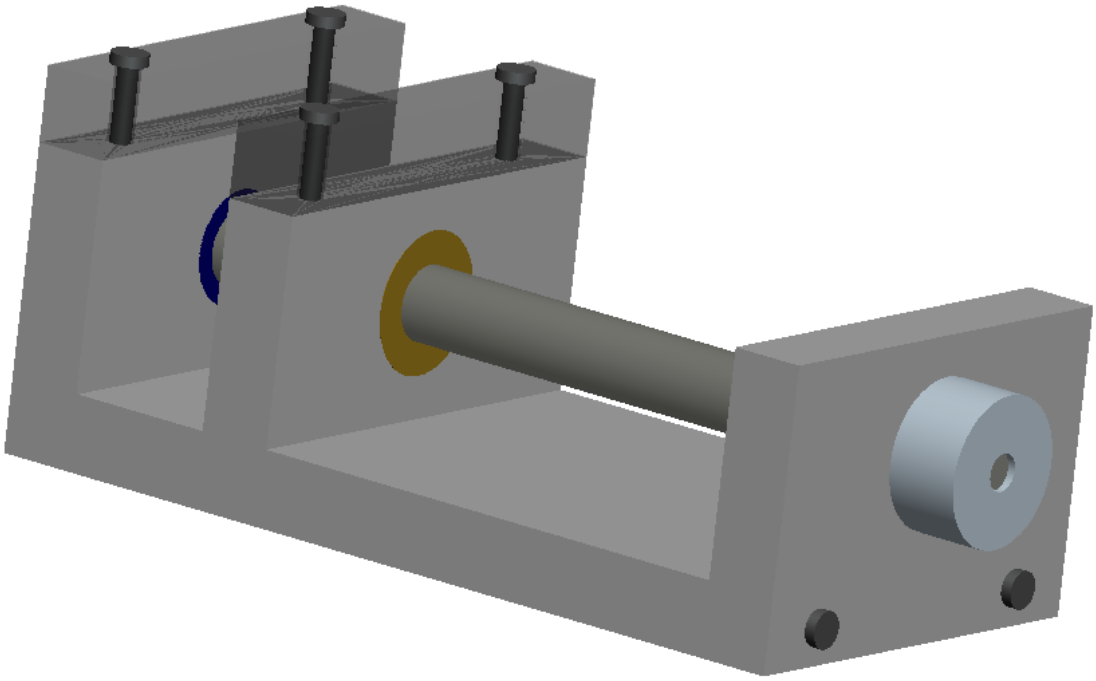

Figure 18 - CAD drawing of strain device

3.2.2. Buckled Surface Fabrication

PDMS (Sylgard 184, Dow Corning) sheets of 1 mm – 3 mm thickness were cast onto flat square petri dishes, degassed and cured overnight at ambient condition. The PDMS mix ratio was varied in the range of 10:1 to 20:1 (Base:Curing Agent) in order to make

samples with varying elastic moduli. The PDMS was then thermally cured at 75ºC for 2 h. Rectangular specimens of 3 cm x 1 cm were cut with a razor blade and mounted onto the strain device described above. Uni-axial strain was made by clamping the sample ends and stretching along the major axis, typically from 5% to 40%. [64] Surface treatment was carried by oxygen plasma oxidation (Diener Pico Standard Low Pressure Plasma) with prescribed power from 10W to 200 W and exposure time from 15 seconds to 20 minutes. After plasma treatment, the strain was slowly removed from the specimen and it was carefully transferred to a glass slide while being careful to bend the sample as little as possible in order to prevent cracks from forming in the brittle oxide layer. By varying the treatment parameters, specifically exposure time and power, we can tune the oxide layer thickness and by varying strain amplitudes, direct control the pattern wavelength and wave amplitude is possible. The cross-linked PDMS with a 10:1 mix ratio has a modulus of ~1.65 MPa [65] and Poisson ratio of 0.48–0.50.

The native buckled surface is not stable when exposed to culture media and therefore a mold of the buckled surface needs to be made when using for cell culture. To do this, PDMS is mixed at the appropriate ratio and then poured into the bottom of a 35 mm petri dish. The native buckled sample is then placed on top of the PDMS and depending on the desired thickness, weight can be applied. The PDMS is degassed and cured overnight at ambient condition. The two samples are then carefully pulled apart and an exact inversed pattern is achieved. If the initial pattern is desired, the molding process may be repeated with the newly made mold. If releasing the pattern from the mold is a problem, a release agent can be used to help make separating them easier.

3.2.3. Atomic Force Microscope (AFM) Surface Evaluation

Surface topography images were captured using an Asylum MFP-3D atomic force microscope. AFM tips were single beam cantilevers made from n-type silicon with an aluminum backside coating, resonant frequency of 325 kHz, and force constant of 40 N/m. The tip radius was 10 nm with a tip cone angle of 40 degrees. (MikroMasch #NSC15/Al BS/15)

3.2.4. AFM Data Processing

To evaluate the data provided by the AFM, a Matlab code was written which plots the surface contour. The wavelength was determined using a Fourier transform. The amplitude is measured from the contour plot and curvature of the valleys was calculated to ensure that the AFM tip was sufficiently sharp to get accurate measurements. For the full data processing Matlab code please refer to Appendix C.

3.2.5. Fibronectin Coating

Human fibronectin (BD Biosciences #354008) was used for functionalizing the surface of the PDMS samples. Fibronectin was re-suspended in 1 ml of sterile DI water for 30 minutes at room temperature to make a concentration of 1 mg/ml. Calcium and Magnesium free buffer solution used to further dilute the fibronectin solution to the working concentration of 50µg/ml. The culture surface was treated with 1 minute of oxygen plasma in order to better adhere the fibronectin to the surface. An appropriate amount of fibronectin solution was used to completely cover desired culture surface, after the plasma treatment, and the sample was incubated at room temperature for 1 hour. The remaining solution was aspirated and surface was rinsed gently using sterile DI water. Cells distributed in media were then pipetted onto the fibronectin activated surface and allowed to adhere for at least 4 hours.

3.2.6. C2C12 Cells

Cells were received as a gift from Professor Bashir at the University of Illinois at Urbana-Champaign. The cell line C2C12 is an immortal line of mouse skeletal myoblasts originally derived from satellite cells from the thigh muscle of a two month old female C3H mouse donor 70h after a crush injury. [66] From the C2s the immortal subline C2C12 was selected. These cells differentiate well into myocytes under appropriate culture conditions. The cells are adherent in culture and are grow well on culture dishes. They grow as undifferentiated myoblasts in growth medium (described below). Myogenic differentiation is initiated upon reaching confluence by switching the cells to medium containing horse serum instead of the FBS.

3.2.7. C2C12 Cell Culture

Cells were cultured using Eagle's Minimum Essential Medium (DMEM) supplemented with 10% Fetal Bovine Serum (FBS) and 1% Penicillin Streptomycin (Pen/Strep). Media was changed every 2-3 days depending on cell concentration. To passage cells, the cell monolayer is rinsed briefly with 1 x Phosphate Buffer Solution (PBS) and then incubated with pre-warmed (37°C) 0.05% Trypsin-EDTA solution for 5 - 7 minutes. Once the cell layer is detached from culture surface (5-7 min at 37°C), the Trypsin is deactivated by adding equal volume of culture media. The cell suspension is transferred to a 15ml centrifuge tube and separated by centrifuging for 5 minutes at 500g. The supernatant is discarded and the pellet is re-suspended in culture media. Cells were split 1:8 every 2 - 3 days. Cultures were incubated at 37°C in humidified atmosphere with 5% CO_2.

3.2.8. C2C12 Cryo Preservation

Cells were cultured in 100mm petri dishes and allowed to grow to about 80% confluence. Culture plate was rinsed with 1 x PBS and then incubated with pre-warmed 0.05% Trypsin-EDTA for 5-7 minutes or until cells have detached from surface. Trypsin is deactivated by adding equal volume of culture media. The cell suspension is transferred to a 15ml centrifuge tube and separated by centrifuging for 5 minutes at 500g. The supernatant is discarded and the pellet is re-suspended in 950 µl and transferred to a cryo vial. Immediately before freezing, 50 µl of Dimethyl sulfoxide (DMSO) was added to the cell suspension. Initial freezing done at -80°C for 24 hours and then transferred to liquid nitrogen (-196 °C) for long term storage.

3.3. Results and Discussion

3.3.1. Buckled Surface

Buckled surfaces were fabricated with varying wavelengths and amplitudes as controlled by pre-strain amount and oxygen plasma exposure time and intensity. Several defects occur during the buckling process. The first are cracks that form perpendicular to the buckling waves. These cracks can be attributed to Poisson's ratio because as the strain is released along the length of the specimen, the width of the specimen will also return to its original dimension therefore causing a tension on the brittle top surface resulting in cracks. The second type of defect is when two waves merge into a single wave which will be referred to as a merger defect. This happens repeatedly throughout the specimen as can be seen in Figure 19.

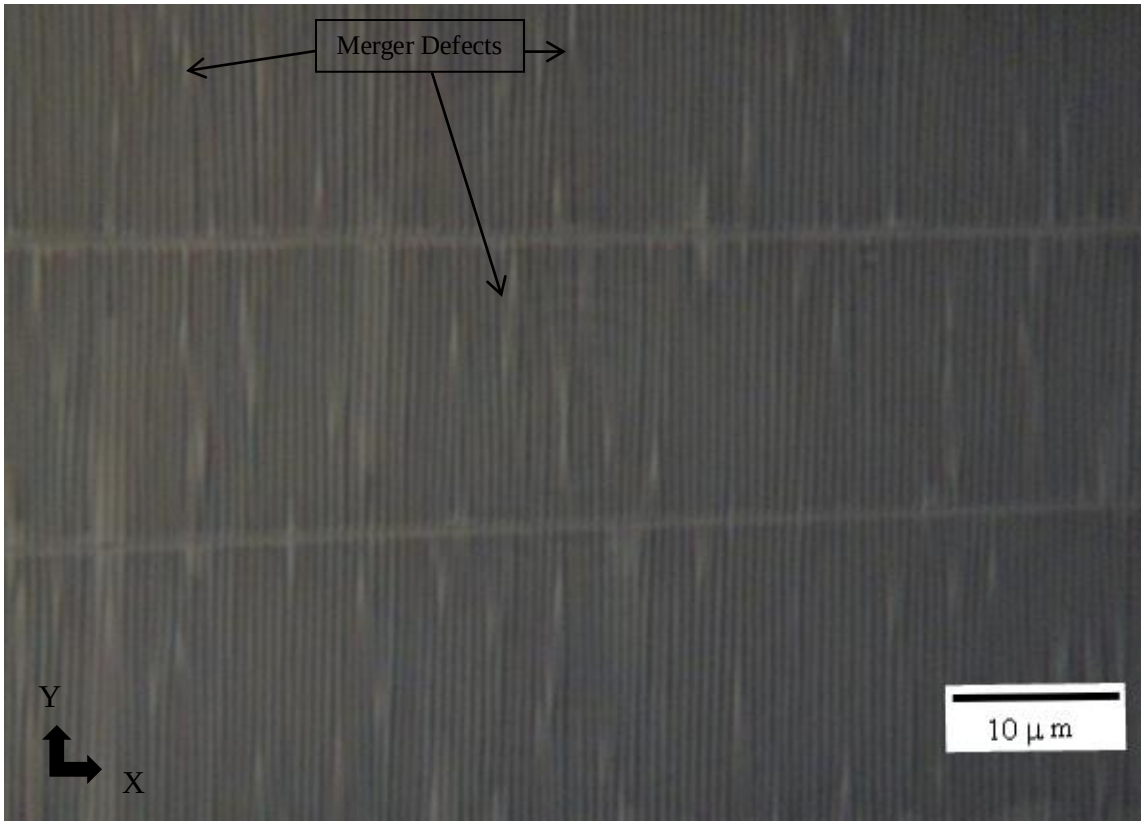

Figure 19 - Brightfield Image of Buckled surface. Buckled waves are parallel to the Y direction and 2 cracks can be seen parallel to the X direction. Merger Defects can be are all of the lighter colored spots throughout the image. PDMS with 10% pre-strain and 1 minute of oxygen plasma treatment at 100 Watts. Amplitude ~54 nm and wavelength ~500.

An atomic force microscope was used to characterize the nano scale features of the buckled surfaces. The buckled surfaces formed with lower curvature at the peaks as compared with the higher curvature found in the valleys meaning that they are not symmetric in the vertical direction Figure 20. Initial results showed that smaller strain percentages gave longer wavelengths, but the wave amplitude was relatively unaffected Figure 21.

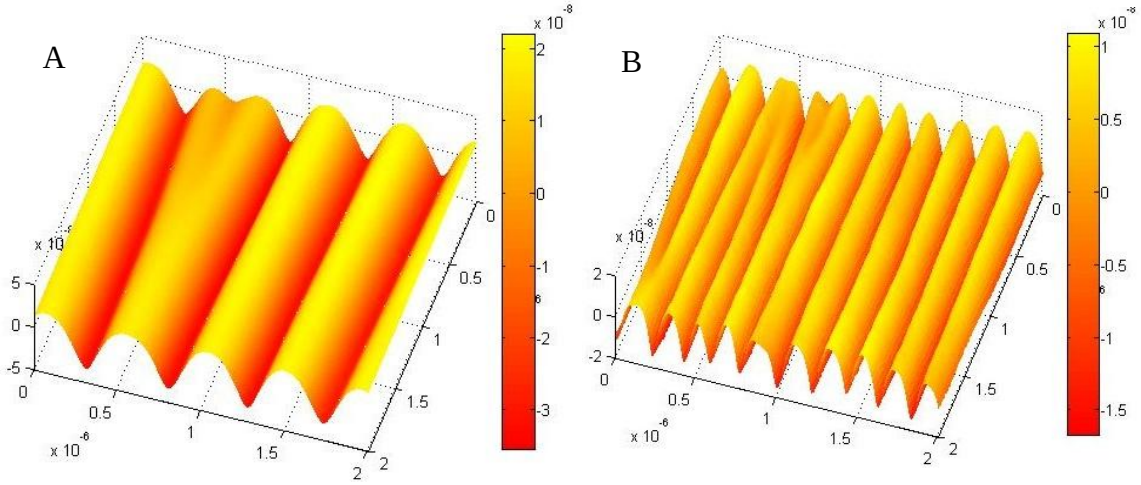

Figure 20 - AFM results for buckled surfaces. (A) PDMS with 10% pre-strain and 1 minute of oxygen plasma treatment at 100 Watts. Amplitude ~54 nm and wavelength ~500 nm. (B) PDMS with 25% pre-strain and 1 minutes of oxygen plasma treatment at 100 Watts. Amplitude ~25 nm and wavelength ~187 nm.

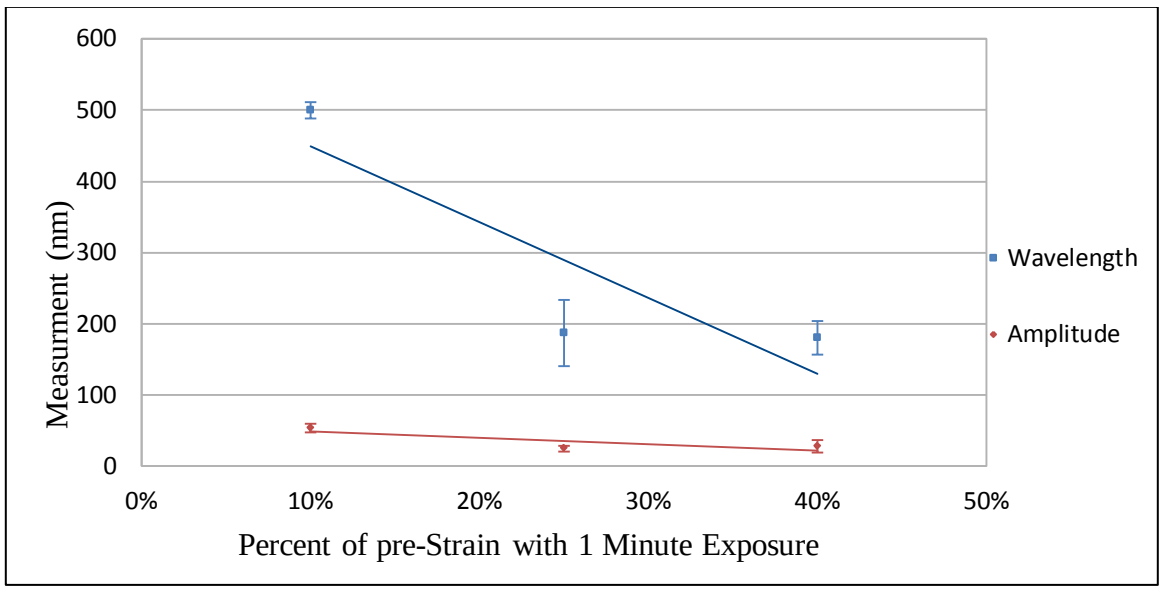

Figure 21 - Effect of Pre-strain amount on Wavelength and Amplitude. Error bars represent one standard deviation.

Next, the effect of varying oxygen plasma oxidation time was evaluated. Longer exposure times created a thicker oxide layer on the PDMS and thus also created larger wavelengths with longer exposure times. The combination of small strain and long plasma exposure created the largest wavelengths. The long plasma exposure time slightly increased the amplitude for samples with 10% strain, however the effect was not as significant as with the wavelength (Figure 22). Exposure times longer than 10 minutes created surfaces that became rough and the buckling patterns were irregular.

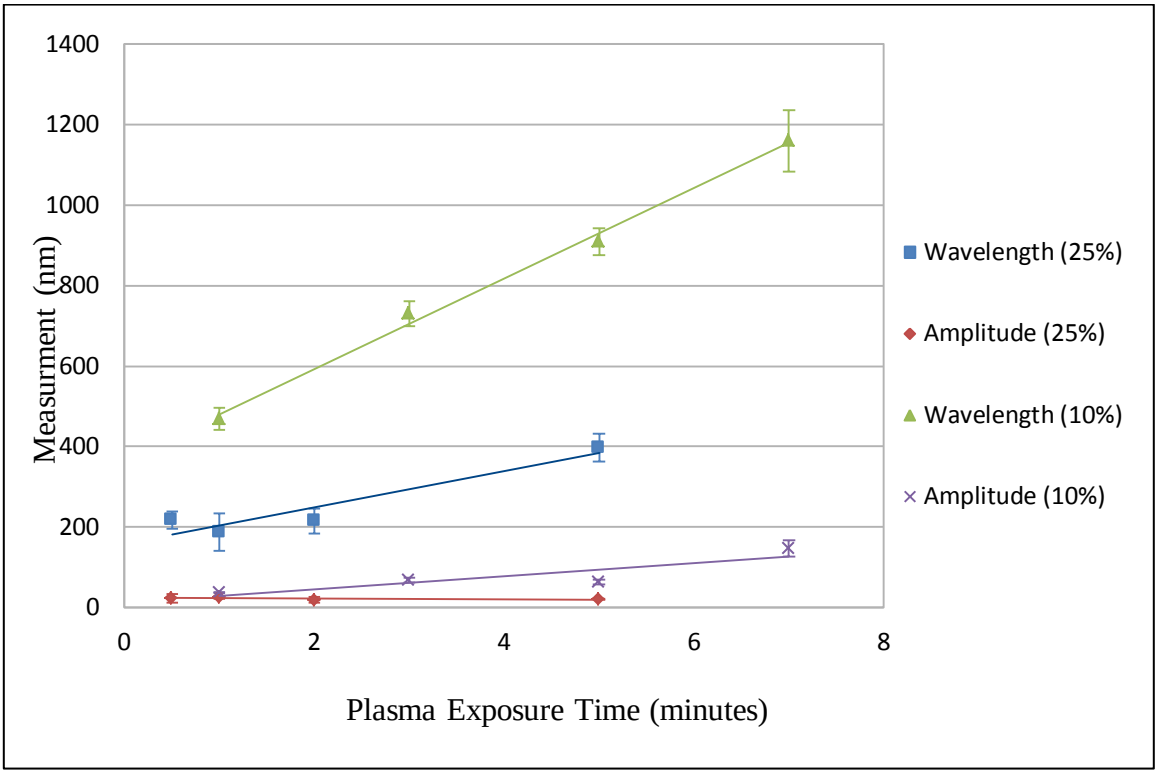

Figure 22 - Buckled surface Wavelength and Amplitude with Various exposure times. Error bars represent one standard deviation.

3.3.2. Fibronectin Coated Surfaces

Since we are using fibronectin to coat our topography with nano scale features, it was important to ensure that the coating was not significantly affecting the topography that would be felt by a cell. First, an AFM image of a flat PDMS sample with no surface treatment was taken (Figure 23-A). Second, the same PDMS sample was subjected to 1 minute of oxygen plasma treatment with power set at 100 watts which are the settings typically used for adhering the Fibronectin to the PDMS samples (Figure 23-B). Finally,

the oxygen plasma treated PDMS was coated with fibronectin and scanned again with AFM (Figure 23-C). The native untreated PDMS sample shows a perfectly flat surface with picometer scale roughness. After the oxygen plasma treatment, the roughness of the surface is still on the picometer scale. The final AFM scan with the fibronectin show that the proteins are less than 3 nm in size and as such are deemed to not influence a cell's ability to sense the topography which is on the scale of 100's of nanometers.

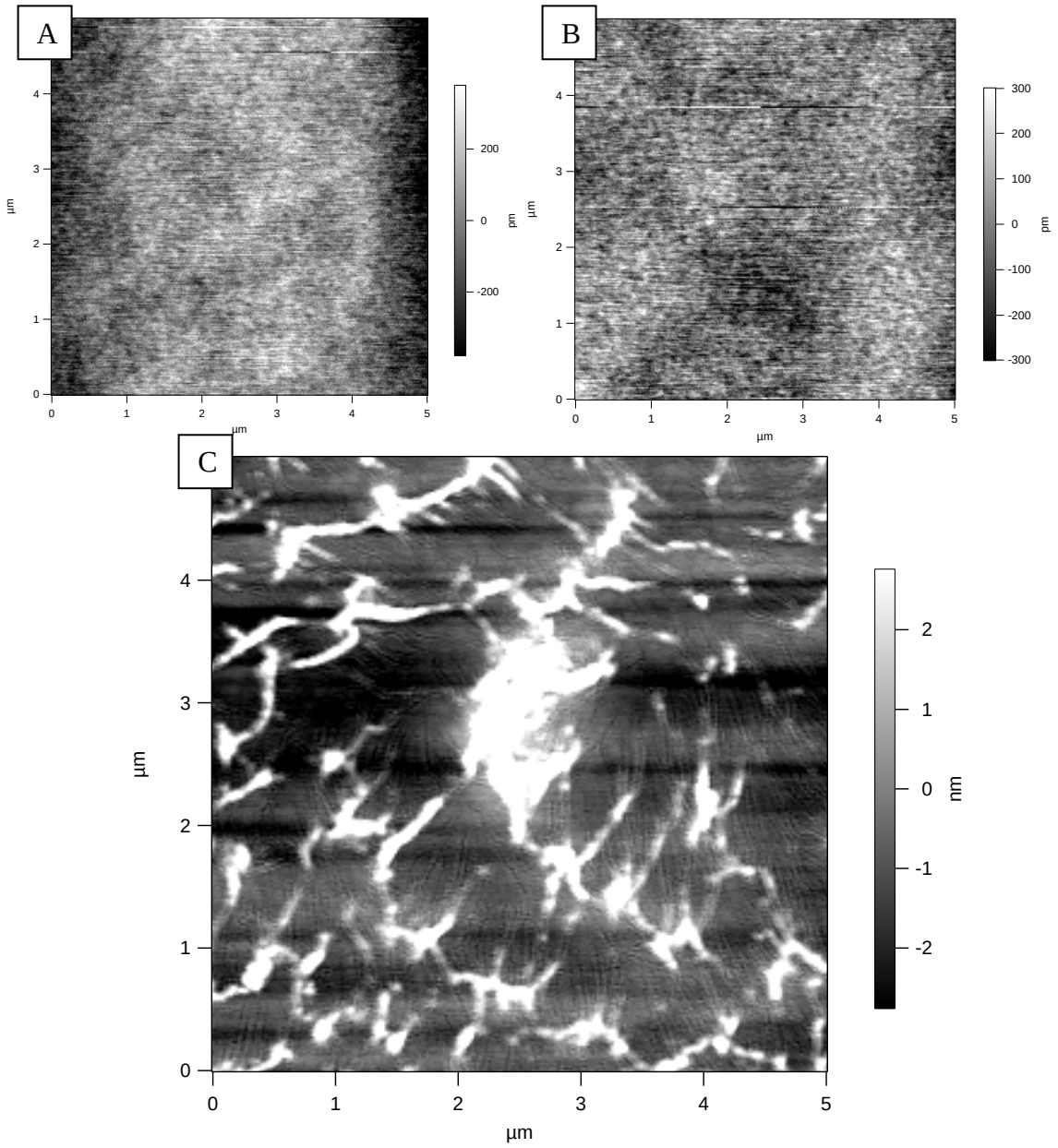

Figure 23 - AFM images of; (A) untreated PDMS, (B) Oxygen Plasma treated PDMS, (C) Fibronectin coated PDMS. Gray level scale bar indicates height of surface.

3.3.3. C2C12 Cells Plated on Wavy Surface

C2C12 cells were plated on the 2 µm wavy surface and they showed alignment with the pattern after only one day of culture (Figure 24). The cells did not show alignment with the smaller 833 nm and 417 nm wavelengths after only one day (Figure 25).

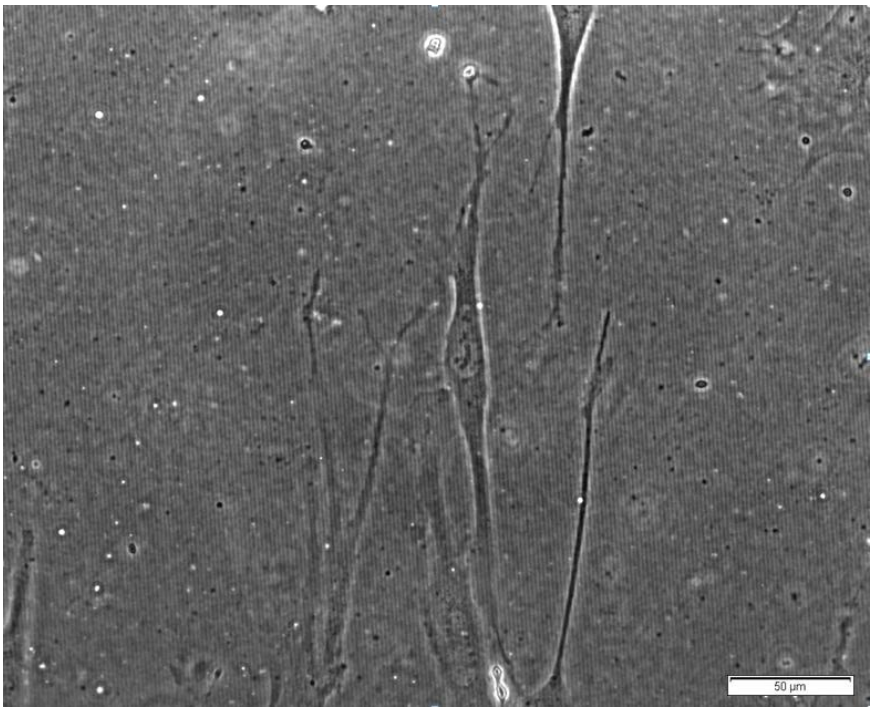

Figure 24 - C2C12 cells aligning with 2 µm waves after 24 hours.

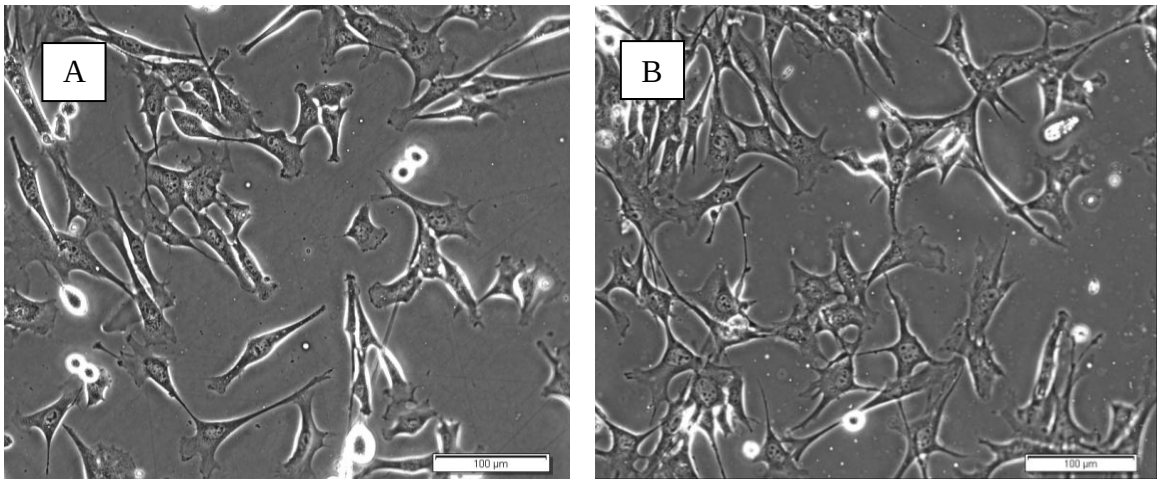

Figure 25 - C2C12 cells on (A) 833 nm and (B) 417 nm waves showing no alignment after 24 hours. Scale bars are 100 µm.

After allowing the cells to continue to grow on the buckled surfaces for an additional day, the smaller wavelength patterns which initially had little effect on cell orientation began to have a large effect. A very clear alignment of the cells with both the 833 nm and 417 nm wavelengths can be seen in Figure 26. This leads to two hypothesis; 1) cell contact guidance is enhanced when the cells have neighbors and so there is a collective sensing of the substrate, or 2) smaller features simply take longer for the cell responses to happen and therefore cell alignment is slower.

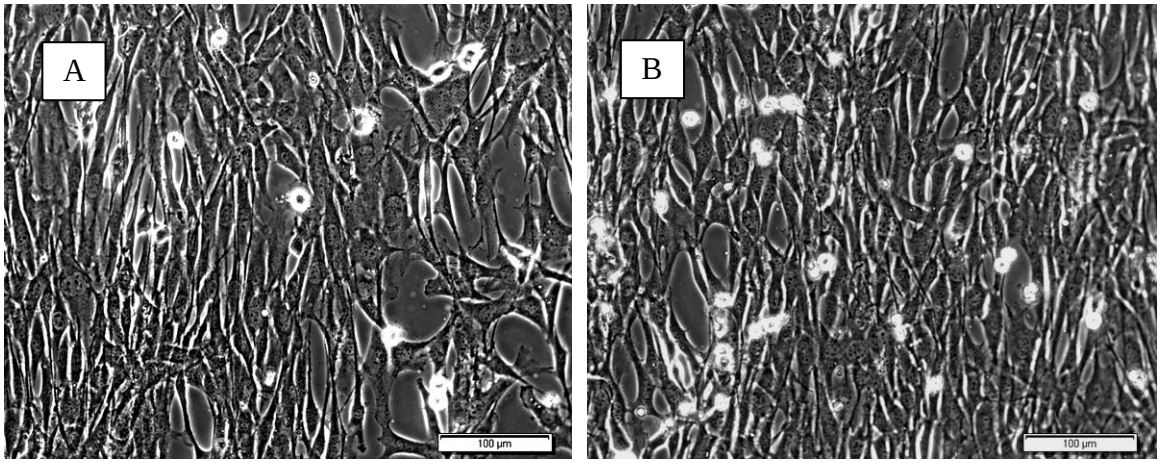

Figure 26 - C2C12 cells on (A) 833 nm and (B) 417 nm waves showing significant alignment after 48 hours. Scale bars are 100 µm.

3.3.4. Conclusions

The pre-strain induced pattern fabrication technique provides a simple, cost effective way for producing nano and micro scale features. The control of strain, plasma intensity, and plasma duration provide several ways to fine tune the wave length and amplitude. The simplicity of this technique and biocompatibility of PDMS makes this an ideal method to explore cell mechanics and the influence that curvature has on cellular response. The use of fibronectin is necessary to support cell adhesion and our AFM results show that despite the nano scale features possible using this method, the fibronectin is still relatively small and therefore should have negligible impact on a cells ability to sense the substrate. The immediate alignment shown by the C2C12 cells with the 2 µm topography and the delayed alignment with the smaller 833 nm and 417 nm topography suggests that curvature may influence cell sensing mechanisms. It is possible that the collective

substrate sensing sensitivity of the C2C12 cells increases with higher cell density but further studies are required to determine if this is the case. It may also be possible that the topography sensing mechanism of the cells just respond slower to smaller features.

3.3.5. Future Work

While topography and curvature have been shown to have substantial impact on cellular functions, the exact mechanism for cell substrate sensing still needs to be discovered. The use of these buckled surfaces will provide an alternative approach for the study of topographical influences. The use of these well-defined, optically clear PDMS substrates can be used for high resolution imaging techniques such as Spatial Light Interference Microscopy (SLIM) to explore cell force generation and Fluorescent Resonance Energy Transfer (FRET) to visualize and quantify signaling transduction in live cells cultured on these surfaces. Using topography as a means for cell alignment opens the door for many other types of cellular mechanics studies. Using the C2C12 cells, we may be able to align the cells using the topography such that when the cells are differentiated into myotubes, the myotubes will also be aligned. Using the aligned myotubes with an external stimulation such as an electric pulse, it may be possible to get a simultaneous contraction and the resulting contractions of every cell will cumulatively provide a net force. This alignment and cumulative contraction is a key component in the future development biobots and artificial muscle.

CHAPTER 4: DIFFUSION MODELING OF HYDROGEL ENCAPSULATED CELLS*

4.1. Scope of Research

4.1.1. Introduction

Revascularization has emerged as a promising strategy to treat various cardiovascular diseases and to recover function of tissue and organs damaged by injuries, traumas, and diseases. [67] [68] Blood vessels play a critical role in homeostasis, regeneration, and pathogenesis of tissues and organs, and their spatial organization is a major factor in influencing vascular function. [69] In this work we present finite element modeling of the diffusional characteristics of a 'living' microvascular stamp which releases multiple angiogenic factors and subsequently creates neovessels with the same pattern as that engraved in the stamp. The stamp consists of a cell encapsulating, hydrogel matrix that promotes cellular expression of angiogenic factors, and a three-dimensional geometry that localizes the angiogenic factors within an inscribed pattern. When the stamp is implanted on a target tissue, it created the desired pattern of neovessels based on its 3D geometry. Here we will look at the numerical simulation used to validate the experimental observations that the desired blood vessel patterns were formed under specific physical 3D designs of the stamp. Overall, the microvascular stamp would serve to direct the emergent cellular behavior towards vascularization, and further improve the quality of revascularization therapies. The numerical model developed in this study will help to better understand the interactions between cells, extracellular matrix, media, and the target tissue. The model can be used to optimize the design of microvascular stamps in order to best direct blood vessel growth.

4.1.2. Stamp Fabrication

The hydrogel was fabricated by photo crosslinking a mixture of fibroblast cells and pre-gel solution in a layer by layer fashion using a stereolithography apparatus. [70] 3D CAD models were generated and exported to stereolithography format for creating hydrogels

* Reprinted, with permission, from J. H. Jeong, V. Chan, C. Cha, P. Zorlutuna, C. Dyck, K. J. Hsia, R. Bashir, and H. Kong, ""Living" Microvascular Stamp for Patterning of Functional Neovessels; Orchestrated Control of Matrix Property and Geometry," *Advanced Materials*, vol. 24, pp. 58 – 63, 2012

containing various micro patterns. Stamps were 5 mm in diameter and 200 µm in height (Figure 27). The microchannel diameters were 300 µm, 500 µm, 750 µm, and 1000 µm. The microchannel spacing of 500 µm was held consistent for all channel diameters. These micro patterns guided the delivery of localized angiogenic factors to the tissue underneath the channel.

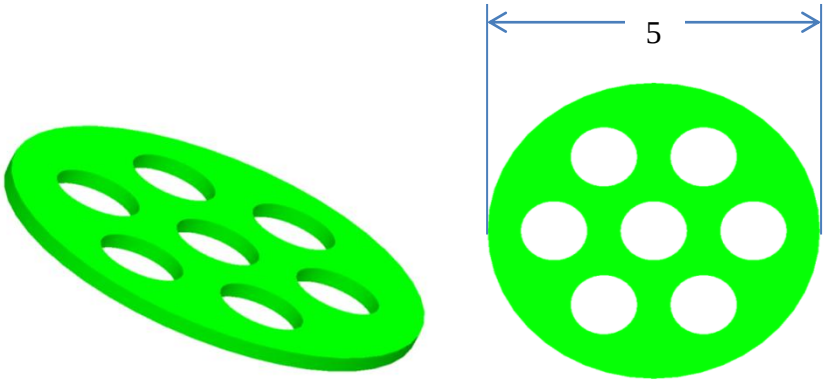

Figure 27 - 3D CAD model of microvascular stamp.

4.1.3. Experimental Method

The living microvascular stamp was implanted onto a chick embryo chorioallantoic membrane (CAM) to quantitatively examine the role of hydrogel properties and stamp geometry in creating neovessels within tissue covered by the stamp. Embryonic chicken eggs were incubated and on the 9th day of gestation, a small window was created on top of each egg. After one day of additional incubation to stabilize CAM and the embryos, a fibroblast-encapsulated hydrogel stamp was implanted on top of the CAM (Figure 28). After incubation for seven days, the membrane was fixed and evaluated.

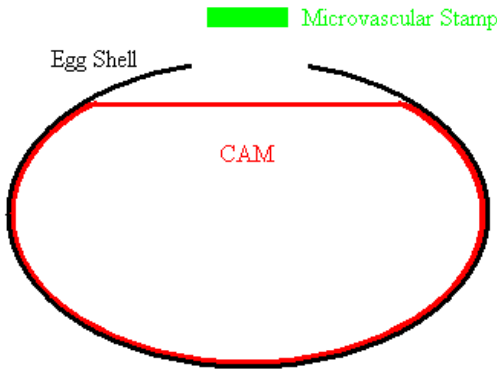

Figure 28 - Schematic of the Implantation of Microvascular Stamp onto CAM

4.2 Finite Element Diffusion Modeling

4.2.1. Model Setup

An axisymmetric finite element model was created using Abaqus/CAE version 6.8 - 4. It was assumed that the diffusional flow effects of each microchannel had a negligible impact on the neighboring microchannels and therefore the modeling focused on an individual microchannel of varying diameter. This assumption was based on the diffusion rate of the hydrogel being significantly slower than that of the media. This meant that the diffusion in the stamp far away from the channel would have little or no impact on the VEGF concentrations within the channel. Only the radius of the hole and the corresponding area of the tissue would be changed from one model to the next (Figure 29).

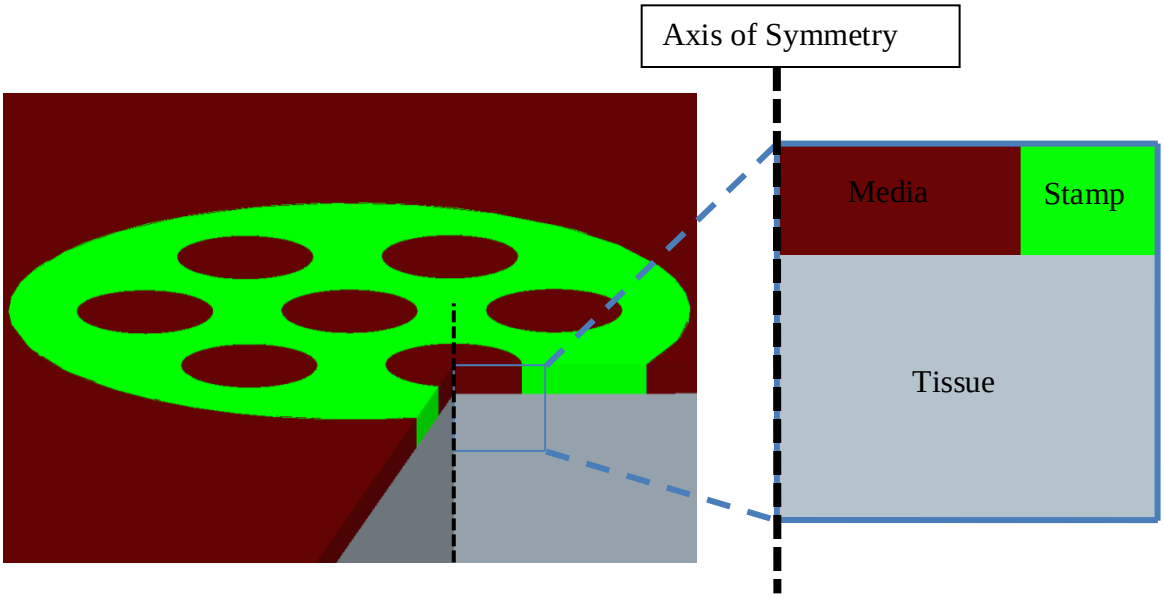

Figure 29 - Schematic of model setup

4.2.2. Model Parameters and Variations

The size of hydrogel stamp used in the model was held constant at 250 μm in width and 200 μm in height to correspond with the experimental stamp height and spacing between channels. A model was created for each of the experimental microchannel diameters of 300, 500, 750, and 1,000 μm using 3 node axisymmetric triangles for the mesh. The model was assumed to have no diffusional flow or loss through the top of the gel and

microchannel as was dictated by the experimental setup. The outer vertical surface was also assumed to have no diffusional flow in the horizontal direction outside of the control volume. The CAM membrane was modeled as being 400 μm thick with a constant concentration of zero at the lower boundary of the model. This constant concentration acted as a sink, thereby consuming the VEGF once it reached the bottom surface of the model. The diffusion in the hydrogel, the microchannels, and within the tissue were presumed to be governed by the diffusion coefficients following Fick's law of diffusion for isotropic materials with constant diffusion coefficients of 200 $\mu m^2/s$, 1.0 $\mu m^2/s$, and 0.1 $\mu m^2/s$ for the media, CAM, and hydrogel stamp, respectively. [71] The diffusion across the boundaries between different materials was assumed to be unobstructed. The interaction property for each of the boundaries was subsequently set as the average of the two materials involved. The stamp had a constant body flux of 3.1×10^{-14} $pg/\mu m^3 \cdot s$ which represented the constant production of VEGF by the fibroblasts (Figure 30). All simulations were in micrometers, seconds, and picograms. Each of the diameters was modeled to simulate a period of 7 days.

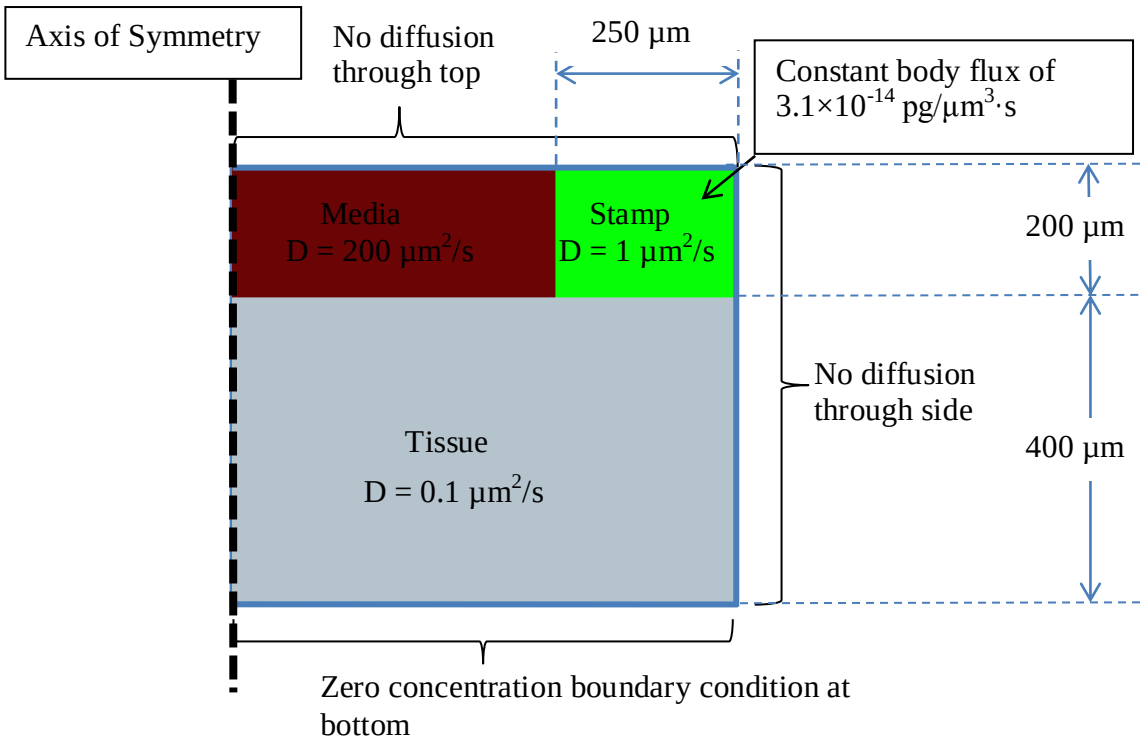

Figure 30 - Model Setup

4.2.3. Fick's Law of Diffusion

The central principle of Fick's 1st law is that the flux of particles 'J' is proportional to the gradient of the concentration. If the distribution of particles is spatially inhomogeneous at time 't', then in the absence of external driving forces, the particles will diffuse in order to decrease the concentration gradients. [72] The net flow of particles to reduce the concentration gradient is:

$$\boldsymbol{J_i = -\left[D_{ij}\right]\frac{\partial c}{\partial x_j}} \qquad \text{Equation 1}$$

Where the diffusion coefficient 'D' is a second-order tensor:

$$\boldsymbol{D_{ij} = \begin{bmatrix} D_{xx} & D_{xy} & D_{xz} \\ D_{yx} & D_{yy} & D_{yz} \\ D_{zx} & D_{zy} & D_{zz} \end{bmatrix}} \qquad \text{Equation 2}$$

For the isotropic materials explored in this thesis, the situation is less complex. All the off-diagonal terms are zero, and the diagonal terms are equal, $[D_{ij}] = D$. Equation 1 then becomes:

$$\boldsymbol{J_x = -D\frac{\partial c}{\partial x}}$$
$$\boldsymbol{J_y = -D\frac{\partial c}{\partial y}} \qquad \text{Equation 3}$$
$$\boldsymbol{J_z = -D\frac{\partial c}{\partial z}}$$

Since our problem is better suited for cylindrical coordinates, the Cartesian coordinate equations can be easily related. A point in the cylindrical coordinate system P(r, φ, z) is related to a point in Cartesian coordinate space P(x, y, z) such that z = z, y = r*sin(φ), and x = r*cos(φ). The fluxes in the appropriate directions may be written as:

$$\boldsymbol{J_r = -D\frac{\partial c}{\partial r}}$$
$$\boldsymbol{J_\varphi = -D\frac{\partial c}{\partial \varphi}\frac{1}{r}} \qquad \text{Equation 4}$$
$$\boldsymbol{J_z = -D\frac{\partial c}{\partial z}}$$

However, Fick's 1st law is valid under steady state diffusion conditions and does not provide direct information about specific time dependencies of the diffusion process. The concentration profile in stamp, media, and tissue depend explicitly on time and on position and therefore Fick's 2nd law must be employed to accomplish this: [72]

$$-\nabla \cdot \boldsymbol{J} = \frac{\partial c}{\partial t} \qquad \text{Equation 5}$$

Where if we substitute Fick's 1st law and simplify the cylindrical coordinates assuming that the Diffusion coefficient remains constant, we are left with Fick's 2nd law in cylindrical coordinates:

$$\frac{\partial c}{\partial t} = \frac{D}{r}\left[\frac{\partial}{\partial r}\left(r\frac{\partial c}{\partial r}\right) + \frac{\partial}{\partial \varphi}\left(\frac{1}{r}\frac{\partial c}{\partial \varphi}\right) + \frac{\partial}{\partial z}\left(r\frac{\partial c}{\partial z}\right)\right] \qquad \text{Equation 6}$$

In our case, the diffusion coefficient is assumed constant because of the low concentration of diffusants. With this assumption, the interactions between diffusants and interactions between the diffusants and the host environment are insignificant.

4.3 Results and Discussion

4.3.1. CAM Experimental Results

Implantation of the PEGDA-MA hydrogel containing microchannels of diameter smaller than 1000 μm stimulated the growth of neovessels with blood flow along its circular pattern (Figure 31a-2, a-3, b-2, and b-3). The spacing between the circular neovessels was the same as the spacing of the microchannels introduced into the hydrogel. The cells encapsulated in the stamps remained viable at the implant sites. In addition, the circularly patterned neovessels were interconnected to each other, which suggested that sprouting of new capillaries from one circular-shaped neovessel stimulated formation of the neighboring patterned neovessels. Such patterning of neovessels was neither achieved in the same hydrogel without cells, nor in the microchannel-free hydrogel loaded with cells (Figure 31a-1 and b-1). In addition, none of the neovessels replicated the circular pattern of microchannels when the diameter of the microchannels was increased to 1,000 μm (Figure 31a-4 and b-4). Most of the neovessels were formed along irregular and tortuous paths. Overall, the results demonstrate that the microvascular stamp with specific sized microchannels created mature and functional neovessels with the desired patterns in live tissue.

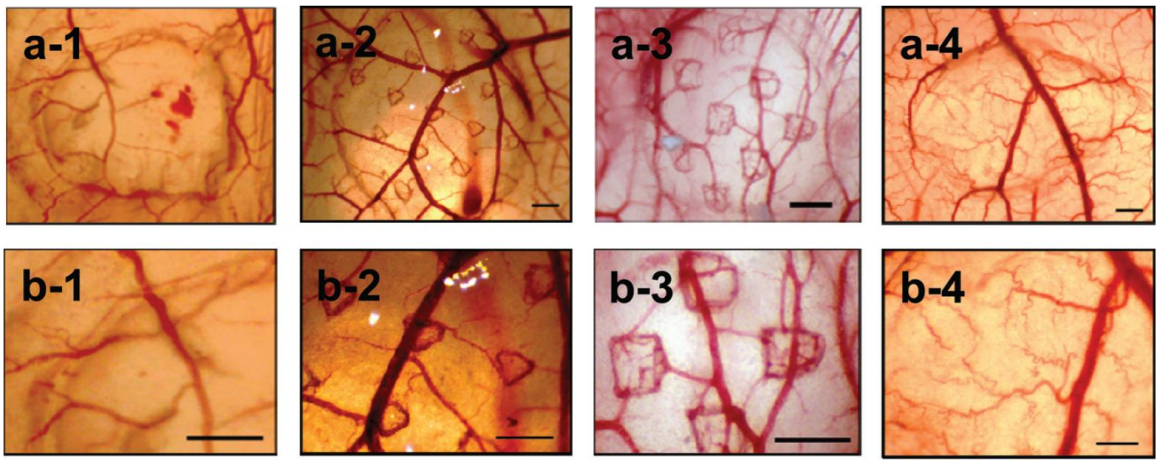

Figure 31 - Formation of patterned neovessels on chick chorioallantoic membrane (CAM). a) The bright field images of neovessels formed under PEGDA-MA hydrogels containing microchannels of diameters at 0 μm (a-1), 300μm (a-2), 500 μm (a-3), and 1,000 μm (a-4). The implant sites shown in (a) were further magnified in (b) (scale bars represent 500 μm). These images were captured seven days after implantation.

4.3.2. Modeling Results

The experimental results showed clear microchannel size dependence for blood vessel growth. The simulation results show that the concentration of VEGF below the smaller diameter of microchannel is much greater than that below the larger diameter of microchannel (Figure 32 and Figure 33). It is also clear that the concentration of VEGF directly below the stamp is lower than that below the channel, with every size microchannel explored in this experiment. This is due to the very slow diffusion rate in the hydrogel stamp compared to that in the media within the microchannels. The media acts as a transportation route taking the VEGF from the entire inner surface of the channel and routing it with a much higher diffusion rate to the surface of the tissue.

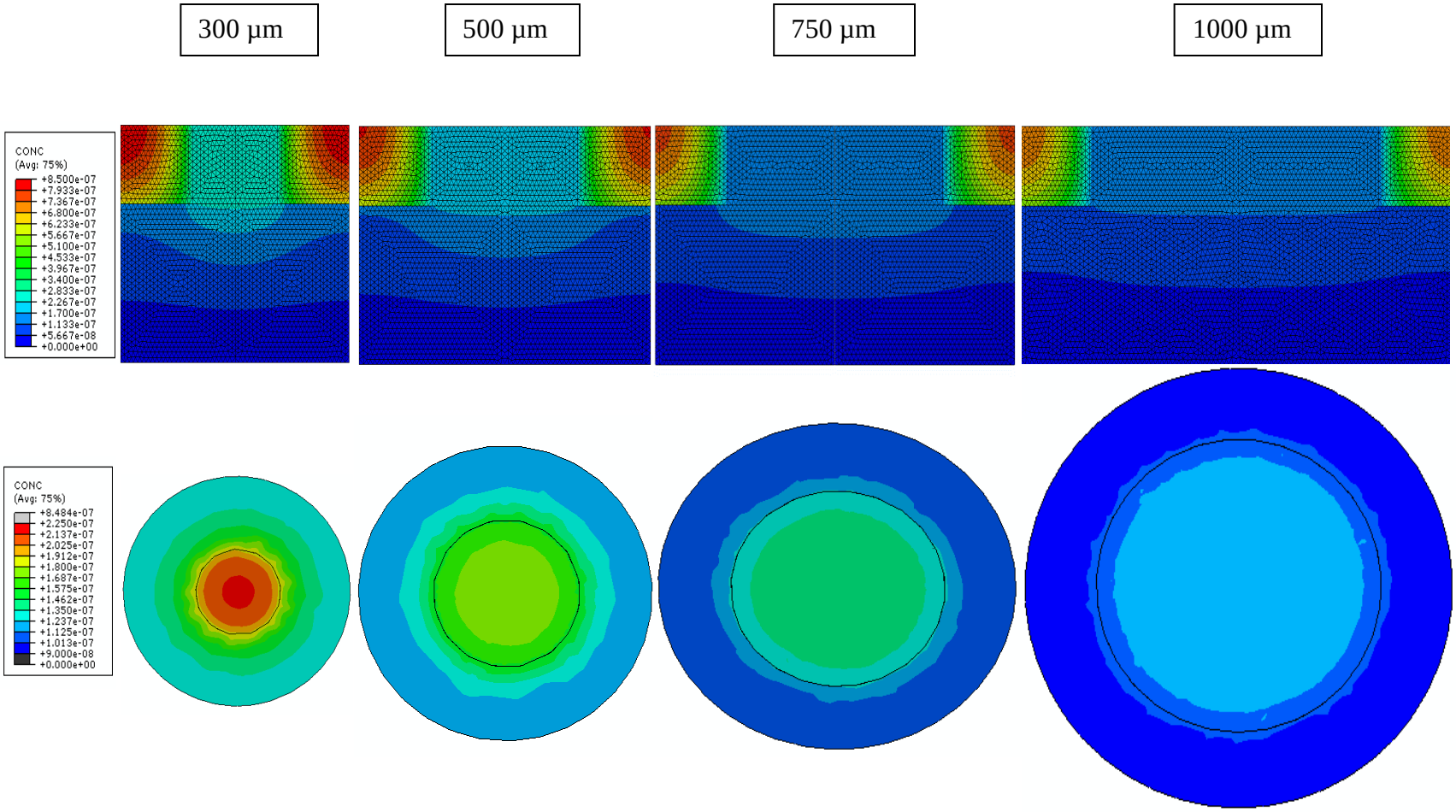

Figure 32 - Concentration of VEGF after 7 days of diffusion. Top view images show radial VEGF concentration 20 µm below the surface of the CAM.

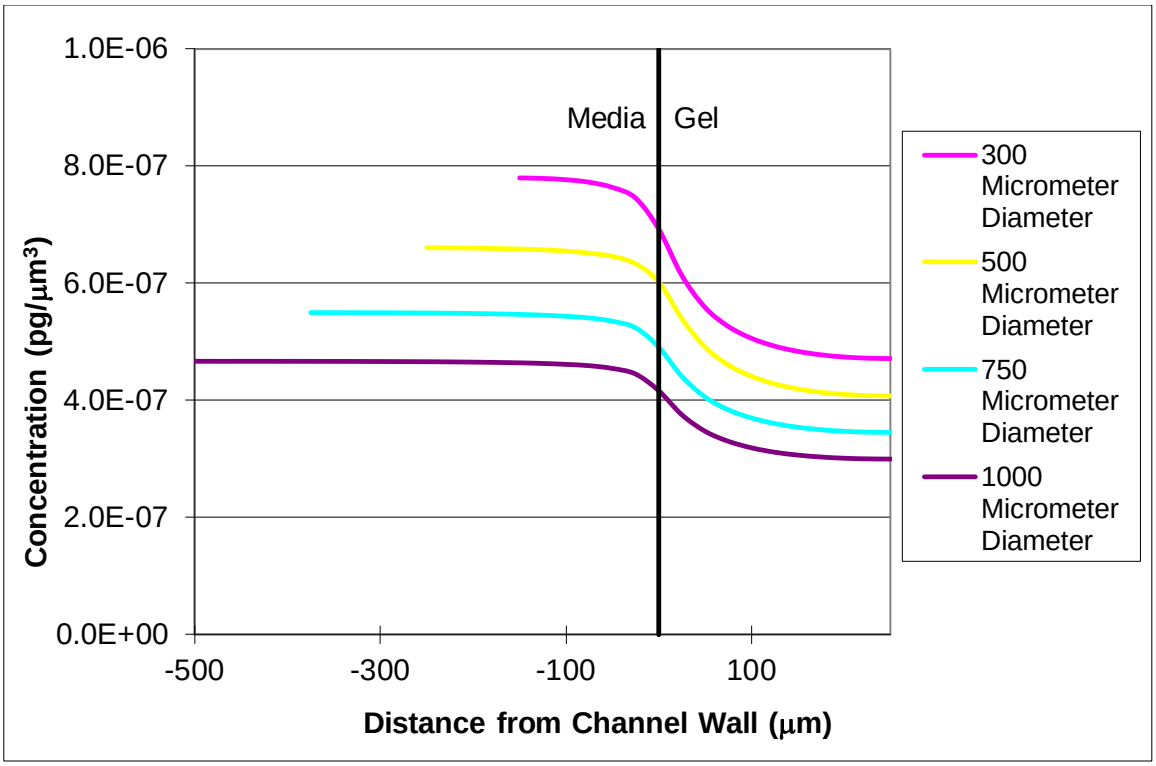

Figure 33 - Plot showing the concentrations of VEGF for each microchannel size at 20 micrometers below the CAM surface after 7 days.

Another advantage of the cell encapsulating hydrogel is the continued production and release of the angiogenic growth factors supplied by the living cells. In earlier experiments and models when only VEGF was incorporated in the hydrogel, no patterning of the neovessels occurred, which suggests the importance of the constant production of multiple growth factors in generating mature and functional blood vessels in the desired patterns. The modeling with only the VEGF incorporation showed a high early concentration which was quickly depleted as the VEGF was diffusively spread throughout the entire volume of the model and eventually consumed at the base. It is also possible that during the fabrication of the microvascular stamp, the high intensity laser was causing the VEGF to become denatured. Therefore, live cells provide an improved method for patterning the neovessels, because of their intrinsic properties of synthesizing and secreting multiple angiogenic factors in a sustained manner. This sustained production is evident in the time lapse model as seen on the next page in Figure 34.

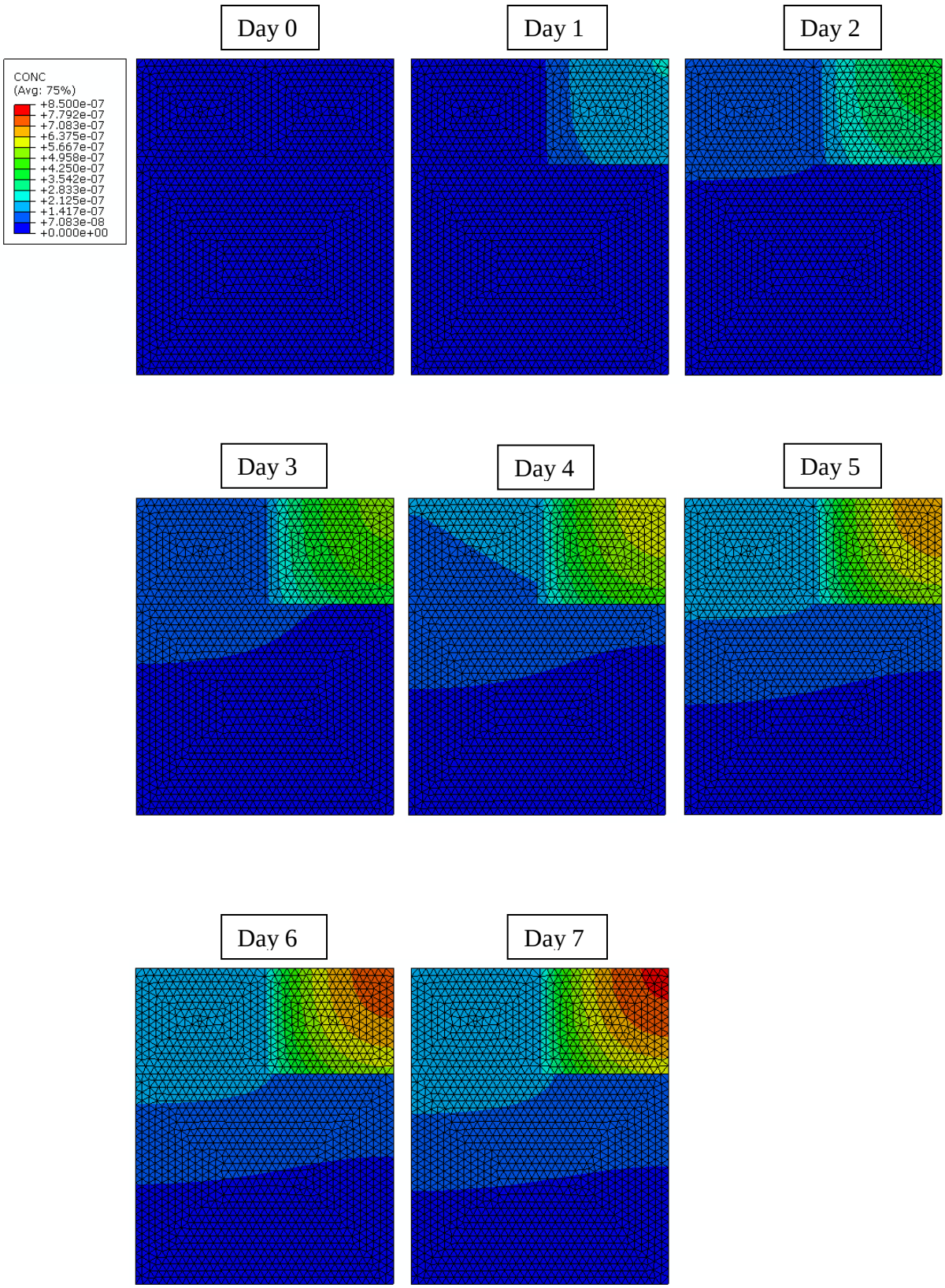

Figure 34 – Seven Day time lapse of concentrations in 500 micrometer channel.

In addition to the increased concentration below the microchannels, there is an increased mass flow rate at the circumference of the microchannels (Figure 35 and Figure 36), possibly explaining the patterning of the neovessels closer to the edges of the microchannels as experimentally observed. The increased molar flow rate of angiogenic factors into the tissue underneath the circumference of the microchannel wall was increased with the use of appropriate microchannel dimensions. The increased molar flow rate likely led to the local increase of the concentration of angiogenic factors within the tissue below the region surrounded by the microchannel wall. This local increase of the mass flow rate of angiogenic factors at the edges of the microchannel wall could be a key factor to initiate the growth of blood vessels. Consider that the model does not account for a growing blood vessel which would perceivably consume more growth factors than its surrounding tissue that lacks blood vessels. Since the flow rate is highest in the tissue immediately below the microchannel wall, when a blood vessel sprouts at this location, the growth factors consumed by it would be most quickly replenished at this location because of the high flow rate.

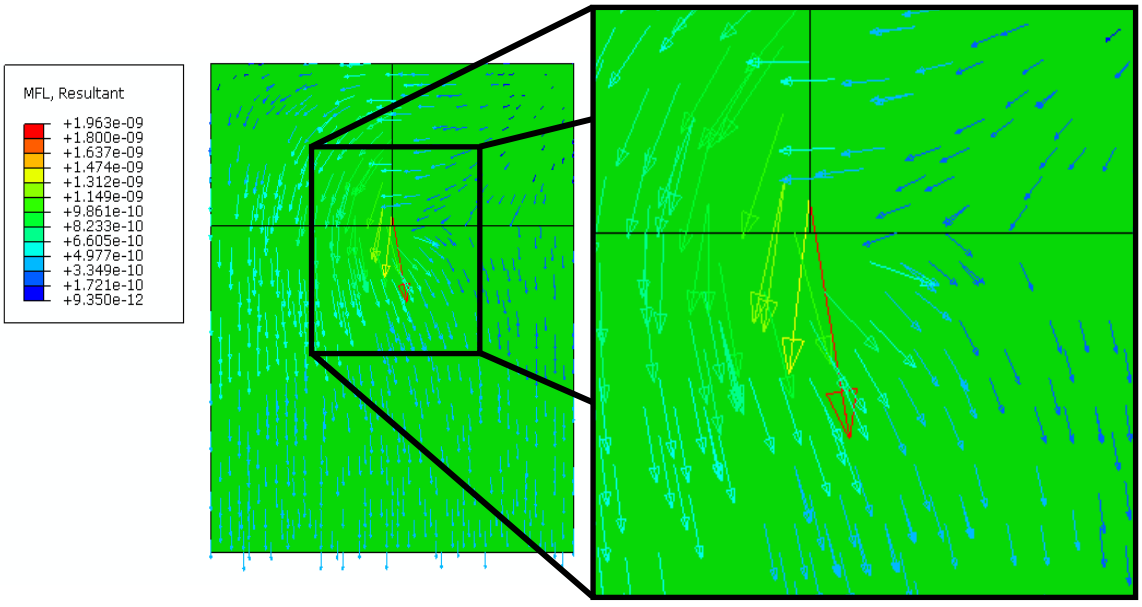

Figure 35 - Vector field showing mass flow rate of diffusing VEGF. Larger arrows represent higher mass flow rate.

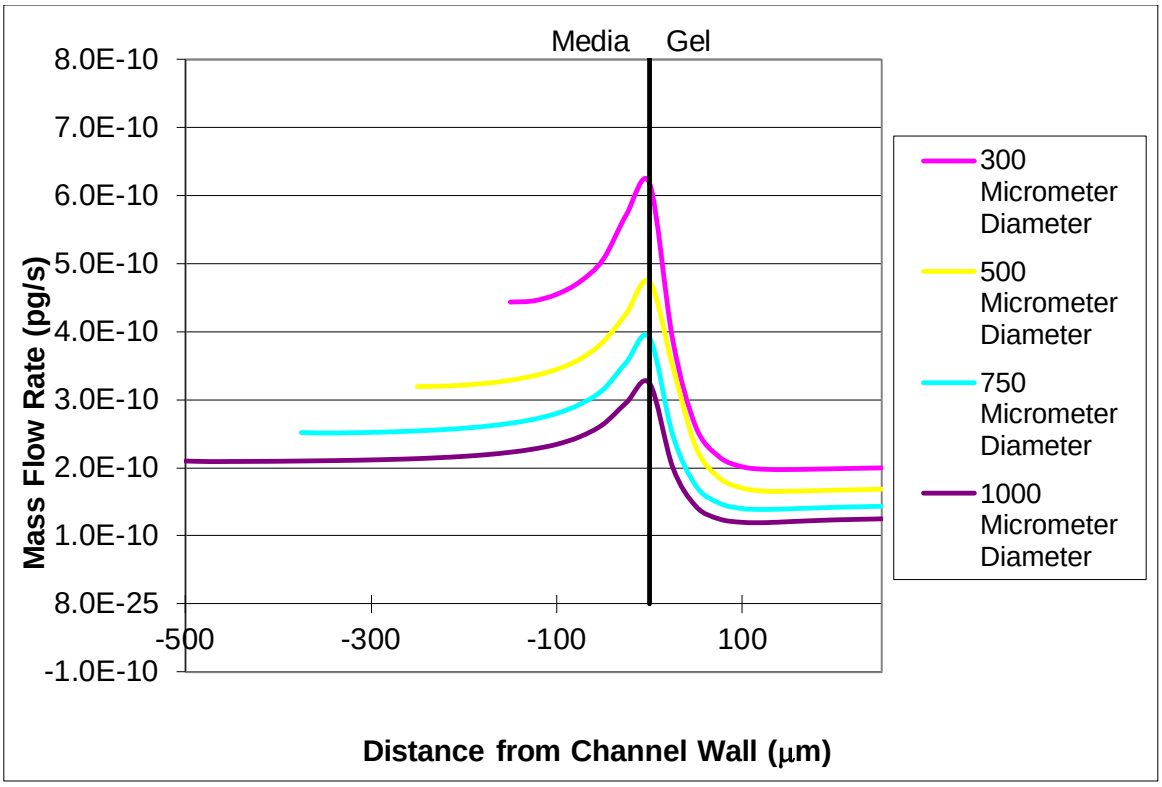

Figure 36 – Plot showing mass flow rate for all microchannel sizes at 20 micrometers below the surface of the CAM after 7 days

4.3.3. Conclusions

The microchannel dimension is a key factor in the patterning of the neovessels. The experimental and modeling results show a strong relationship between geometry and VEGF concentrations and flow rates. The ratio between microchannel diameter and height is the key dimensional property that governs blood vessel growth and controlled the molar flow rate of cell-secreted angiogenic factors into the tissue below microchannel wall edges. The experimental results suggest that at a diameter to height ratio of 5:1, the molar flow rate and concentration become too low to instigate blood vessel formation. This information, accompanied with the numerical simulations suggests that a mass flow rate of VEGF must be on the order of 4.0×10^{-10} pg/s and a concentration of VEGF must be on the order of 5.0×10^{-7} pg/μm^3 for blood vessel formation. With this particular hydrogel system, this concentration and mass flow rate are not possible without the use of transportation routes provided by the microchannels. The complicated system of diffusion that is present in experimental setup makes an analytical solution impossible to obtain.

This fact makes the use of a finite element model irreplaceable because in tandem with the experimental results, the modeling allows for a better understanding of the system dynamics and also allows for certain values to be calculated from the model.

4.3.4. Future Work

The model needs further development in order to more precisely simulate the consumption of growth factors. Based on the experimental and numerical results, the mass flow rate is a critical component in blood vessel formation and the modeling needs to be able to simulate this blood vessel formation and accompanying VEGF consumption. From this type of model we have been able to solve for threshold values necessary for the initiation of blood vessel growth. However, at this point, the values suggested in this thesis are merely a starting point and for more precise future simulations, more basic experiments must be carried out to better characterize the diffusion properties of the hydrogel, CAM, media, and all of the interfaces. The use of this model will also be an important tool for future, more complicated and optimized stamp designs that will no longer adhere to simple diameter versus height scaling laws. These more complicated shapes can be fabricated for better and more efficient VEGF delivery to the target tissue.

WORKS CITED

[1] D. Ingber, "Cellular Tensegrity Revisited I. Cell Structure and Hierarchical Systems Biology," *Cell Science*, vol. 116, pp. 1157-1173, 2003.

[2] T. Myers, *Anatomy Trains: Myofascial Meridians for Manual and Movement Therapists*.: Elsevier Limited, 2009.

[3] K. Yamada and B. Geiger, "Molecular Interactions In Cell Adhesion Complexes," *Current Opinion in Cell Biology*, vol. 9, pp. 76–85, 1997.

[4] D. Ingber, "Mechanobiology and the Diseases of Mechnotransduction," *Annals of Medicine*, vol. 35, pp. 564-577, 2003.

[5] A. Horwitz, "Integrins and Health," *Scientific American*, vol. 276, pp. 68-75, 1998.

[6] D. Ingber, "The Architecture of Life," *Scientific American*, vol. 278, pp. 48-57, 1998.

[7] M. Berridge. (2012) Cell Signalling Biology. [Online]. http://www.cellsignallingbiology.org/csb/002/csb002.pdf

[8] E. Haswell, R. Philips, and D. Rees, "Mechanosensitive channels: What Can They Do and How Do They Do It?," *Structure*, vol. 19, no. 10, pp. 1356 - 1369, 2011.

[9] D. Butcher, T. Alliston, and V. Weaver, "A tense situation: forcing tumour progression," *Nature Reviews Cancer*, vol. 9, pp. 108-122, 2009.

[10] K. Huang, R. Mukhopadhyay, B. Wen, Z. Gitai, and N. Wingreen, "Cell shape and cell-wall organization in Gram-negative bacteria," *PNAS*, vol. 105, pp. 19282-19287, 2008.

[11] H. Huang, R. Kamm, and R. Lee, "Cell mechanics and mechanotransduction: pathways, probes, and physiology," *American Journal of Physiology - Cell Physiology*, vol. 287, pp. C1-C11, 2004.

[12] R. Hochmuth, "Micropipette aspiration of living cells," *Journal of Biomechanics*, vol. 33, pp. 15-22, 2000.

[13] N. Wang and D. Ingbert, "Control of Cytoskeletal Mechanics by Extracellular Matrix, Cell Shape,and Mechanical Tension," *Biophysics Journal*, vol. 66, pp. 2181-2189, 1994.

[14] M. Radmacher, M. Fritz, and P. Hansma, "Imaging soft samples with the atomic force microscope: gelatin in water and propanol," *Biophysical Journal*, vol. 69, pp. 264-270, 1995.

[15] P. Davies et al., "Spatial relationships in early signaling events of flow-mediated endothelial mechanotransduction.," *Annual Review of Physiology*, vol. 59, pp. 527-549, 1997.

[16] W. Ahmed, M. Kural, and T. Saif, "A novel platform for in situ investigation of cells and tissues under mechanical strain," *Acta Biomaterialia*, vol. 6, pp. 2979–2990, 2010.

[17] N. Ho and B. Chan, "Effect of Dynamic Mechanical Compression on Actin Cytoskeleton Network of Human Mesenchymal Stem Cells (hMSCs) in Three Dimensional Collagen Constructs," in *International Conference on Nano/Molecular Medicine and Engineering*, Hong Kong, 2010, pp. 136-139.

[18] V. Chauhan, T. Stylianopoulos, Y. Boucher, and R. Jain, "Delivery of Molecular and Nanoscale Medicine to Tumors: Transport Barriers and Strategies," *Annual Review of Chemical and Biomolecular Engineering*, vol. 2, pp. 281–298, 2011.

[19] U. Hanson et al., "Combination of reduced oxygen tension and intermittent hydrostatic pressure: a useful tool in articular cartilage tissue engineering," *Journal of Biomechanics*, vol. 34, pp. 941-949, 2001.

[20] R. Smith et al., "In Vitro Stimulation of Articular Chondrocyte mRNA and Extracellular Matrix Synthesis by Hydrostatic Pressure," *Journal of Orthopaedic Research*, vol. 14, pp. 53-60, 1996.

[21] R. Smith et al., "Time-dependent effects of intermittent hydrostatic pressure on articular chondrocyte type II collagen and aggrecan mRNA expression," *Journal of Rehabilitation Research and Development*, vol. 37, pp. 153-161, 2000.

[22] J. Parkkinen et al., "Effects of Cyclic Hydrostatic Pressure on Proteoglycan Synthesis in Cultured Chondrocytes and Articular Cartilage Explants," *Archives of Biochemistry and Biophysics*, vol. 300, pp. 458-465, 1993.

[23] Y. Qin, T. Kaplan, A. Saldanha, and C. Rubin, "Fluid pressure gradients, arising from oscillations in intramedullary pressure, is correlated with the formation of bone and inhibition of intracortical porosity," *Journal of Biomechanics*, vol. 36, pp. 1427-1437, 2003.

[24] J. Nagatomi, B. Arulanandam, D. Metzger, A. Meunier, and R. Bizios, "Cyclic Pressure Affects Osteoblast Functions Pertinent to Osteogenesis," *Annals of Biomedical Engineering*, vol. 31, pp. 917-923, 2003.

[25] H. Ozawa et al., "Effect of a Continuously Applied Compressive Pressure on Mouse Osteoblast-like Cells (MC3T3-E1) In Vitro," *Journal of Cellular Physiology*, vol. 142, pp. 177-185, 1990.

[26] J. Roelofsen, J. Klein-Nulend, and E. Burger, "Mechanical Stimulation by Intermittent Hydrostatic Compression Promotes Bone-Specific Gene Expression in Vitro," *Journal of Biomechanics*, vol. 12, pp. 1493-1503, 1995.

[27] J. Nagatomi, B. Arulanandam, D. Metzger, A. Meunier, and R. Bizios, "Effects of Cyclic Pressure on Bone Marrow Cell Cultures," *Journal of Biomechanical Engineering*, vol. 124, pp. 308-314, 2002.

[28] J. Klein-Nulend et al., "Sensitivity of Osteocytes in Biomechanical Stress In Vitro," *The FASEB Journal*, vol. 9, pp. 441-445, 1995.

[29] J. Nagatomi, B. Arulanandam, D. Metzger, A. Meunier, and R. Bizios, "Frequency and Duration Dependent Effects of Cyclic Pressure on Select Bone Cell Functions," *Tissue Engineering*, vol. 7, pp. 717-727, 2001.

[30] H. Shin, M. Gerritsen, and R. Bizios, "Regulation of Endothelial Cell Proliferation and Apoptosis by Cyclis Pressure," *Annals of Biomedical Engineering*, vol. 30, pp. 297-304, 2002.

[31] P. Angele et al., "Cyclic hydrostatic pressure enhances the chondrogenic phenotype of human mesenchymal progenitor cells differentiated in vitro," *Journal of Orthopaedic Research*, vol. 21, pp. 451-457, 2003.

[32] O. Hamill and B. Martinac, "Molecular Basis of Mechanotransduction in Living Cells," *Physiological Reviews*, vol. 81, pp. 685-740, 2001.

[33] J. Gullingsrud, D. Kosztin, and K. Schulten, "Structural Determinants of MscL Gating Studied by Molecular," *Biophysical Journal*, vol. 80, pp. 2074–2081, 2001.

[34] M. Gao, D. Craig, V. Vogel, and K. Schulten, "Identifying Unfolding Intermediates of FN-III10 by Steered Molecular Dynamics," *Journal of Molecular Biology*, vol. 323, pp. 939–950, 2002.

[35] B. Geiger, A. Bershadsky, R. Pankov, and K. Yamada, "Transmembrane Extracellular Matrix–Cytoskeleton Crosstalk," *Nature Reviews Molecular Cell Biology*, vol. 2, pp. 793-805, 2001.

[36] Q. Zeng and W. Hong, "The Emerging Role of the Hippo Pathway in Cell Contact Inhibition, Organ Size Control, and Cancer Development in Mammals," *Cancer Cell*, vol. 13, pp. 188–192, 2008.

[37] D. Odde, L. Ma, A. Briggs, A. DeMarco, and M. Kirschner, "Microtubule bending and breaking in living fibroblast cells," *Journal of Cell Science*, vol. 112, pp. 3283-3288, 1999.

[38] D. Aden, A. Fogel, S. Plotkin, I. Damjanov, and B. Knowles, "Controlled synthesis of HBsAg in a differentiated human liver carcinoma-derived cell line," *Nature*, vol. 282, pp. 615-616, 1979.

[39] J. Ho, K. Gillis, and D. Fishwild. (2004, July) http://www.millipore.com.

[40] Z et al., "Genome-wide genetic analysis of polyploidy in yeast," *Nature*, vol. 443, pp. 541-547, 2006.

[41] R. Flemming, C. Murphy, G. Abrams, S. Goodman, and P. Nealey, "Effects of synthetic micro- and nano-structured surfaces on cell behavior," *Biomaterials*, vol. 20, pp. 573–588, 1999.

[42] A. Green, J. Jansen, J. van der Waerden, and A. von Recum, "Fibroblast response to microtextured silicone surfaces: Texture orientation into or out of the surface," *Journal of Biomedical Materials Research*, vol. 28, pp. 647-653, 1994.

[43] A. Mata, C. Boehm, A. Fleischman, G. Muschler, and S. Roy, "Growth of connective tissue progenitor cells on microtextured polydimethylsiloxane surfaces," *Journal of Biomedical Materials Research*, vol. 62, pp. 499-506, 2002.

[44] M. Dalby, D. McCloy, M. Robertson, C. Wilkinson, and R. Oreffoc, "Osteoprogenitor response to defined topographies with nanoscale depths," *Biomaterials*, vol. 27, pp. 1306–1315, 2006.

[45] E. Cavalcanti-Adam et al., "Cell Spreading and Focal Adhesion Dynamics Are Regulated by Spacing of Integrin Ligands," *Biophysical Journal*, vol. 92, pp. 2964–2974, 2007.

[46] K. Anselme et al., "Qualitative and quantitative study of human osteoblast adhesion on materials with various surface roughnesses," *Journal of Biomedical Materials Research*, vol. 49, pp. 155–166, 2000.

[47] J. Gough, I. Notingher, and L. Hench, "Osteoblast attachment and mineralized nodule formation on rough and smooth 45S5 bioactive glass monoliths," *Journal of Biomedical Materials Research*, vol. 68A, pp. 640–650, 2004.

[48] E. Palin, H. Liu, and T. Webster, "Mimicking the nanofeatures of bone increases bone-forming cell adhesion and proliferation," *Nanotechnology*, vol. 16, pp. 1828–1835, 2005.

[49] C. Bettinger, R. Langer, and J. Borenstein, "Engineering Substrate Topography at the Micro- and Nanoscale to Control Cell Function," *Angewandte Chemie International Edition*, vol. 48, pp. 5406-5415, 2009.

[50] T. Tzvetkova-Chevolleau et al., "The motility of normal and cancer cells in response to the combined influence of the substrate rigidity and anisotropic microstructure," *Biomaterials*, vol. 29, pp. 1541-1551, 2008.

[51] B. Wojciak-Stothard et al., "Role of the Cytoskeleton in the Reaction of Fibroblasts to Multiple Grooved Substrata," *Cell Motility and the Cytoskeleton*, vol. 31, pp. 147-158, 1995.

[52] C. Oakley and D. Brunette, "The sequence of alignment of microtubules, focal contacts and actin filaments in fibroblasts spreading on smooth and grooved titanium substrata," *Journal of Cell Science*, vol. 106, pp. 343-354, 1993.

[53] P. Clark, P. Connolly, A. Curtis, J. Dow, and C. Wilkinson, "Topographical control of cell behaviour I. Simple step cues," *Development*, vol. 99, pp. 439-448, 1987.

[54] A. Teixeira, G. Abrams, P. Bertics, C. Murphy, and P. Nealey, "Epithelial contact guidance on well-defined micro- and nanostructured substrates," *Journal of Cell Science*, vol. 116, pp. 1881-1892, 2003.

[55] F. Johansson, N. Danielsen P. Carlberg, L. Montelius, and M. Kanje, "Axonal outgrowth on nano-imprinted patterns," *Biomaterials*, vol. 27, pp. 1251–1258, 2006.

[56] X. Walboomers, W. Monaghan, A. Curtis, and J. Jansen, "Attachment of fibroblasts on smooth and microgrooved polystyrene," *Journal of Biomedical Materials Research*, vol. 46, pp. 212–220, 1999.

[57] L. Chou, J. Firth, V. Uitto, and D. Brunette, "Substratum surface topography alters cell shape and regulates fibronectin mRNA level, mRNA stability, secretion and assembly in human fibroblasts," *Journal of Cell Science*, vol. 108, pp. 1563-1573, 1995.

[58] M. Dalby, S. Yarwood, C. Wilkinson M. Riehle, and A. Curtis, "Nucleus alignment and cell signaling in fibroblasts: response to a micro-grooved topography," *Experimental Cell Research*, vol. 284, pp. 272–280, 2003.

[59] E. Yim, E. Darling, K. Kulangara, F. Guilak, and K. Leong, "Nanotopography-induced changes in focal adhesions, cytoskeletal organization, and mechanical properties of human mesenchymal stem cells," *Biomaterials*, vol. 31, pp. 1299-1306, 2010.

[60] F. Iacopi, S. Brongersma, and K. Maex, "Compressive stress relaxation through buckling of a low-k polymer-thin cap layer system," *Applied Physics Letters*, vol. 82, pp. 1380-1382, 2003.

[61] N. Bowden, S. Brittain, A. Evans, J. Hutchinson, and G. Whitesides, "Spontaneous formation of ordered structures in thin films of metals supported on an elastomeric polymer," *Nature*, vol. 393, pp. 146-149, 1998.

[62] D. Chua, H. Ng, and S. Li, "Spontaneous formation of complex and ordered structures on oxygen-plasma-treated elastomeric polydimethylsiloxane," *Aplied Physics Letters*, vol. 76, pp. 721-723, 200.

[63] D. Hyun and U. Jeong, "Substrate Thickness: An Effective Control Parameter for Polymer Thin Film Buckling on PDMS Substrates," *Journal ofApplied Polymer Science*, vol. 112, pp. 2683–2690, 2009.

[64] A. Chiche, C. Stafford, and J. Cabral, "Complex micropatterning of periodic structures on elastomeric surfaces," *Soft Matter*, vol. 4, pp. 2285–2528, 2008.

[65] C. Wu, H. Lin, J. Hsu, M. Yip, and W. Fang, "Static and dynamic mechanical properties of polydimethylsiloxane/carbon nanotube nanocomposites," *Thin Solid Films*, vol. 517, pp. 4895–4901, 2009.

[66] D. Yaffe and O. Saxel, "Serial Passaging and Differentiation of Myogenic Cells Isolated From Dystrophic Mouse Muscle," *Nature*, vol. 270, pp. 725-727, 1977.

[67] P. Carmeliet and R.K. Jain, "Angiogenesis in cancer and other diseases," *Nature*, vol. 407, pp. 249-257, 2000.

[68] N. Ferrara and R. Kerbel, "Angiogenesis as a therapeutic target," *Nature*, vol. 438, pp. 967-974, 2005.

[69] E. Silva and D. Mooney, "Effects of VEGF Temporal and Spatial Presentation on Angiogenesis," *Biomaterials*, vol. 31, pp. 1235-1241, 2010.

[70] V. Chan, P. Zorlutuna, J.H. Jeong, H. Kong, and R. Bashir, "Three-dimensional photopatterning of hydrogels using stereolithography for long-term cell encapsulation," *Lab on a Chip - Miniaturisation for Chemistry and Biology*, vol. 10, pp. 2062-2070, 2010.

[71] F. Gabhann, J. Ji, and A. Popel, "Computational model of vascular endothelial growth factor spatial distribution in muscle and pro-angiogenic cell therapy," *PLoS Computational Biology*, vol. 2, pp. 1107-1120, 2006.

[72] P. Green, *Kinetics,Transport, and Structure in Hard and Soft Materials*. Boca Raton, Florida: Taylor & Francis Group, 2005.

[73] J. Davis, Ed., *Metals Handbook Desk Edition*, 2nd ed.: ASM International, 1998.

[74] H. Kuhn and D. Medlin, *ASM Handbook: Mechanical Testing and Evaluation*, 8th ed.: ASM International, 2000.

[75] M. Gauthier, Ed., *Engineered Materials Handbook Desk Edition*.: ASM International, 1995.

Appendix A: Pressurized Incubation Chamber One FEA

PIC-1 was designed to house up to three 10 cm or nine 3.5 cm petri dishes. The chamber wall was fabricated of 0.75 inch thick 6061 – T6 aluminum with an inner diameter of 4.5 inches (11.4 cm). The entire pressure chamber assembly is held together with 6 bolts which pass through the base plate, wall, and top plate. Knurled brass nuts are threaded onto the ends of the bolts to sandwich all the pieces along with two o-rings (Figure 37). The back pressure regulator purchased for this pressure chamber is designed for a maximum pressure of 50 psi and therefore the wall and plates of the pressure chamber were simulated using Pro/Engineer finite element analysis to ensure structural integrity under pressure up to 50 psi. A safety factor of 3 was included in all analysis.

Figure 38 shows the result of the FEA for the chamber wall with 150 psi of pressure to account for the factor of safety. The model is constrained by having a fixed displacement in every direction on the inside of each of the bolt holes. The fixed displacement is reasonable because the plates on both top and bottom of the chamber would act to resist and displacement at the bolts. The maximum resulting Von Mises stress is 909 psi which is significantly less than the yield strength of the 6061 – T6 aluminum of 37000 psi. [73] The wall of the chamber was knowingly overbuilt since the thick wall allowed for greater simplicity during fabrication.

Figure 39 shows the result of the FEA for the top lid of the chamber with 150 psi of pressure to account for the factor of safety. The pressure is applied only inside the 4.6 inch radius of the o-ring which is used to seal the pressure chamber. The lid is constrained by the inner surface of each of the bolt holes. The maximum resulting Von Mises stress is 6138 psi which is significantly less than the yield strength of the Cast Acrylic Disc of 10,000 psi. [74] Since the base plate is the exact same dimensions as the top plate and does not have extra holes for the inlet and outlet ports, it is safe to assume that the base plate will safely meet the criteria without further analysis.

The water capture chamber was designed with smaller dimensions but also with the same wall and plate thicknesses. For that reason, no FEA is required because the stresses will be lower for this chamber.

Bill of Materials

1 – Brass Round Knurled Thumb Nut. ¼" – 20 thread size, 5/8" Head Diameter. (McMaster Carr #92741A160)

2 – Clear Cast Acrylic Disc. 0.5 inch thick, 6 inch diameter. (McMaster Carr #1221T39)
Yeild strength – 10 ksi [74]
Elastic Modulus – 1 x 10^6 ksi [74]
Heat Deflection Temperature - 200ºF [74]

3 – Buna-N O-ring. AS568A Dash Number 248. (McMaster Carr #5018T285)

4 – 6061 T6 Aluminum Body. 4.5 inch I.D. 6 inch O.D.
Yeild strength – 37 ksi [73]
Elastic Modulus – 10 x 10^6 psi [73]

5 – 18-8 Stainless Steel Hex Head Cap Screw. ¼" – 20 thread size, 3.5 inch length.

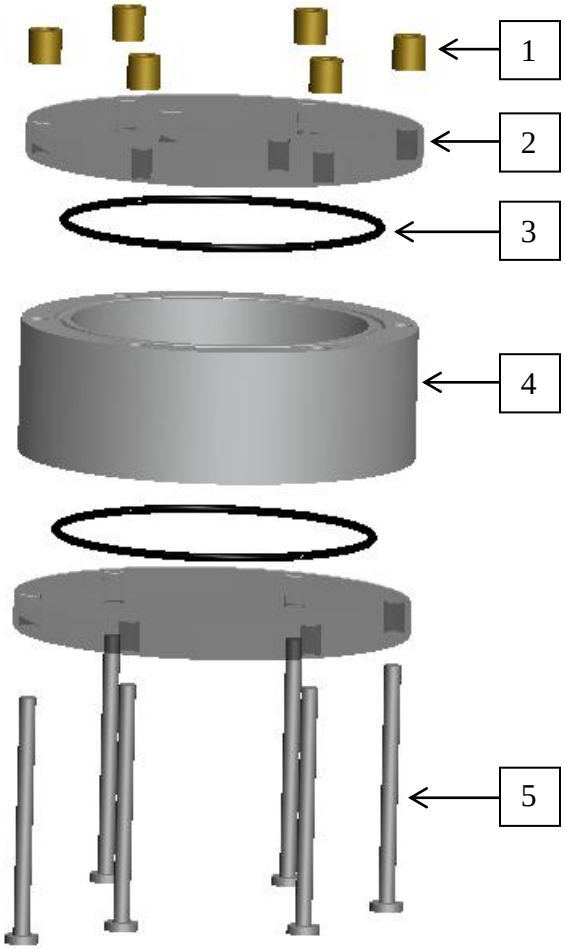

Figure 37 - PIC-1 CAD drawing, Bill of Materials with material properties, and Exploded view.

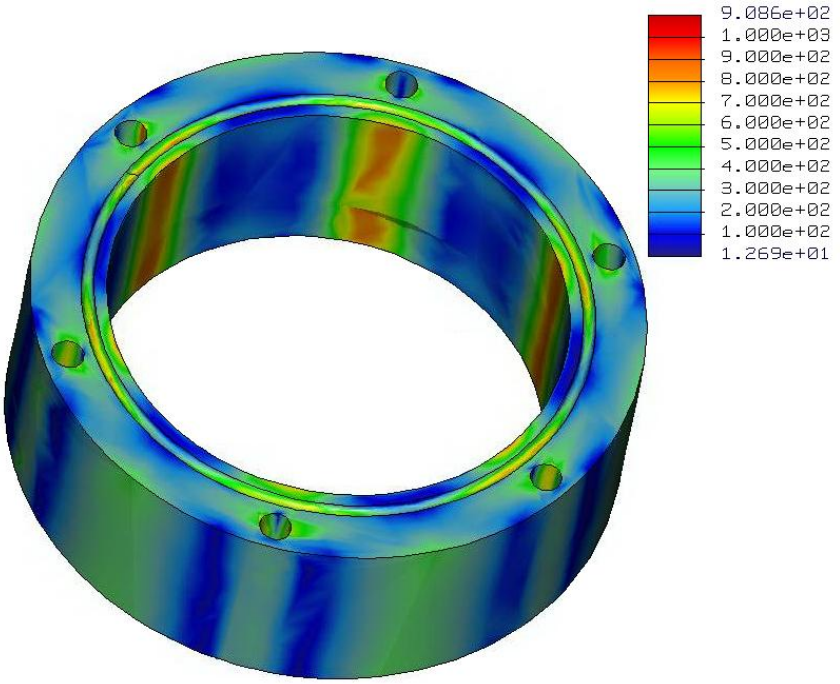

Figure 38 - FEA of chamber wall for PIC-1.

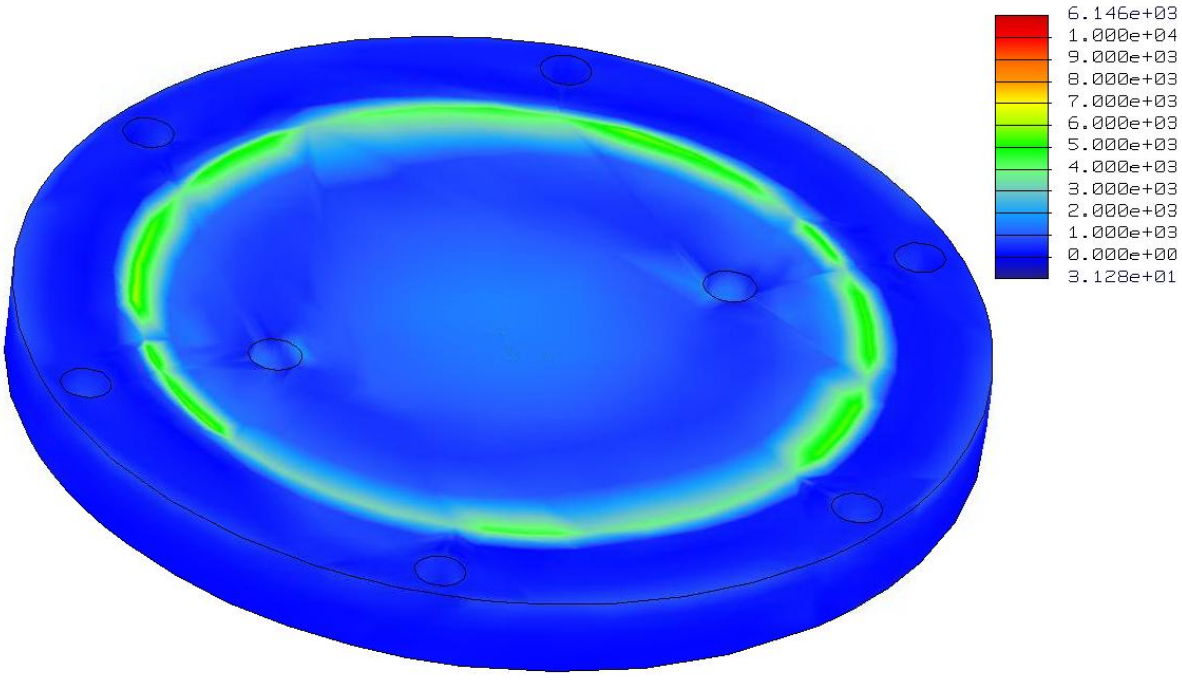

Figure 39 - FEA of lid for PIC-1.

Appendix B: Pressurized Incubation Chamber Two FEA

PIC-2 was designed to house a single 3.5 cm petri dish for live imaging experiments. The chamber wall was fabricated of 0.5 inch thick 6061 – T6 aluminum with an inner diameter of 3 inches. The base was fabricated of 316 stainless steel with a quartz view port cover and the lid was made from acrylic. The base is attached to chamber wall with 6 bolts and the top plate is attached with 6 knurled thumb bolts (Figure 40 and Figure 41). The design goal for this pressure chamber was 150 psi and therefore the wall, base, top plate and quartz window were all simulated using Pro/Engineer finite element analysis to ensure structural integrity under pressure up to 150 psi. A safety factor of 3 was included in all analysis.

Figure 42 shows the result of the FEA for the chamber wall with 450 psi of pressure to account for the factor of safety. The model is constrained by having a fixed displacement in every direction on the inside of each of the bolt holes. The fixed displacement is reasonable because the plates on both top and bottom of the chamber would act to resist and displacement at the bolts. The maximum resulting Von Mises stress is 6257 psi which is significantly less than the yield strength of the 6061 – T6 aluminum of 37000 psi. [73] The wall of the chamber was knowingly overbuilt since the thickness allowed for greater simplicity during fabrication.

Figure 43 shows the result of the FEA for the top lid of the chamber with 450 psi of pressure to account for the factor of safety. The pressure is applied only inside the 3.1 inch radius of the o-ring which is used to seal the pressure chamber. The lid is constrained by the inner surface of each of the bolt holes. The maximum resulting Von Mises stress is 7663 psi which is less than the yield strength of the Cast Acrylic Disc of 10,000 psi. [74]

Figure 44 shows the dimensioned drawing for the base plate. Due to the complicated nature of the interaction between the base plate and the quartz view glass, the FEA was performed on the two parts as an assembly rather than individually. The result of the FEA for the base and the quartz, with 450 psi of pressure is shown in Figure 45, Figure 46, and

Figure **47**. The pressure is applied only inside the 3.1 inch radius of the o-ring which is used to

seal the pressure chamber. The base is constrained by the inner surface of each of the bolt holes. The maximum resulting Von Mises stress for the base is 20880 psi which is less than the yield strength of the 316 stainless steel of 35000 psi. Some stress concentrations exist on the inside edges that are a result of singularities from the analysis (Figure 46). The maximum resulting Von Mises stress for the quartz is 6823 psi which is less than the yield strength of the quartz of 10000 psi.

The humidification chamber was designed with the same dimensions for the wall and plate thicknesses. For that reason, no FEA is required specifically for the humidification chamber because the stresses will be the same.

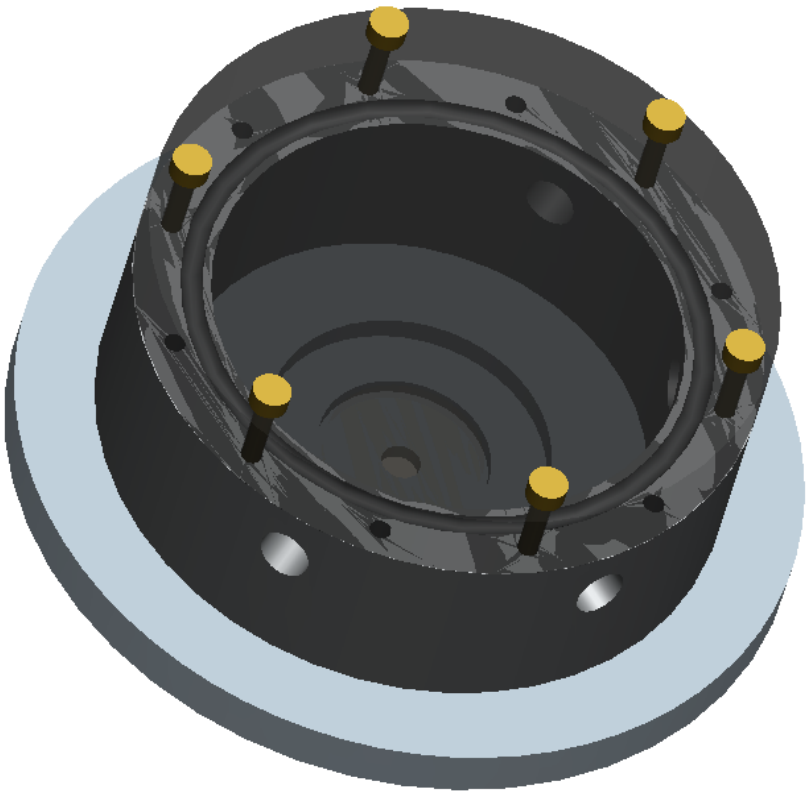

Figure 40 - CAD drawing of PIC-2

Bill of Materials

1 – Brass Knurled Head Thumb Screw
8-32 thread, 1 inch length.
(McMaster Carr #92421A199)

2 – Clear Cast Acrylic Disc
0.5 inch thick, 4 inch diameter.
(McMaster Carr #1221T37)
Yield strength – 10 ksi [74]
Elastic Modulus – 1 x 10^6 ksi [74]
Heat Deflection Temp. - 200ºF [74]

3 – Buna-N O-ring
AS568A Dash Number 235.
(McMaster Carr #2418T19)

4 – 6061 T6 Aluminum Body
3 inch I.D. 4 inch O.D.
Yield strength – 37 ksi [73]
Elastic Modulus – 10 x 10^6 psi [73]

5 – Quartz Disc
1 inch diameter, 1/8 inch thick.
(McMaster Carr #1357T21)
Yield strength – 10 ksi [75]
Elastic modulus – 10.6 x 10^6 psi [75]

6 – 316 Stainless Steel Disc
5 inch diameter, 0.5 in thickness.
(McMaster Carr #9260K71)
Yield strength – 35 ksi [73]
Elastic modulus – 28 x 10^6 psi [73]

7 – Low Head Socket Cap Screw
8-32 thread, 1 inch length.
(McMaster Carr #92220A156)

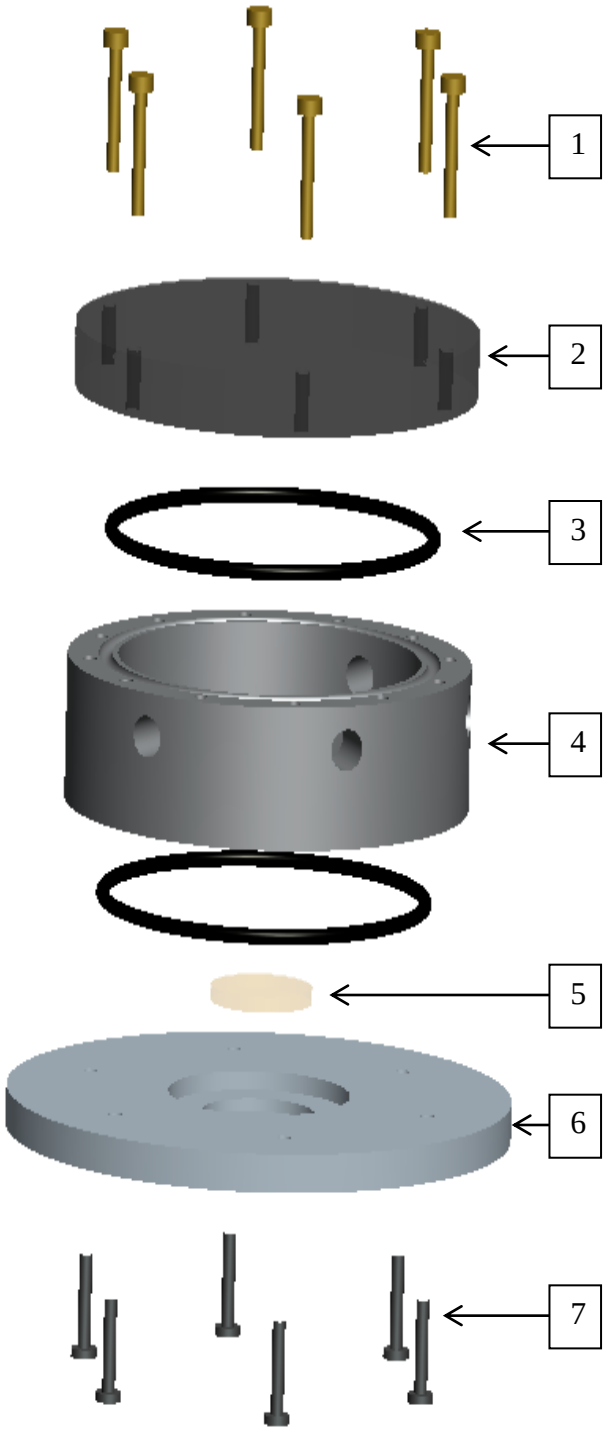

Figure 41 - Bill of Materials and exploded view for PIC-2

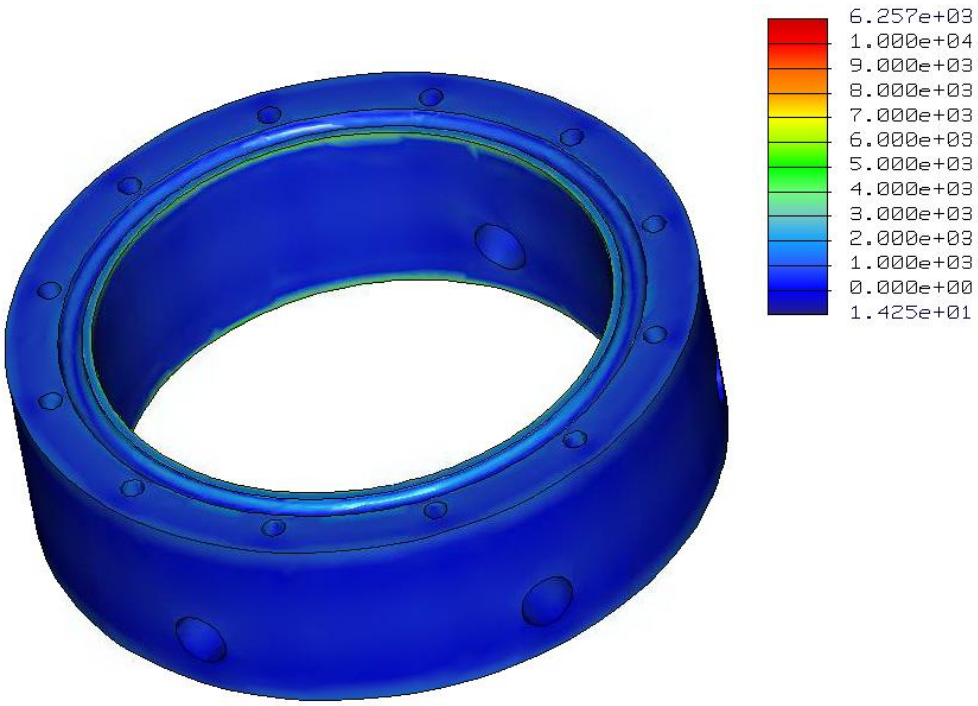

Figure 42 - FEA results for PIC-2 chamber wall

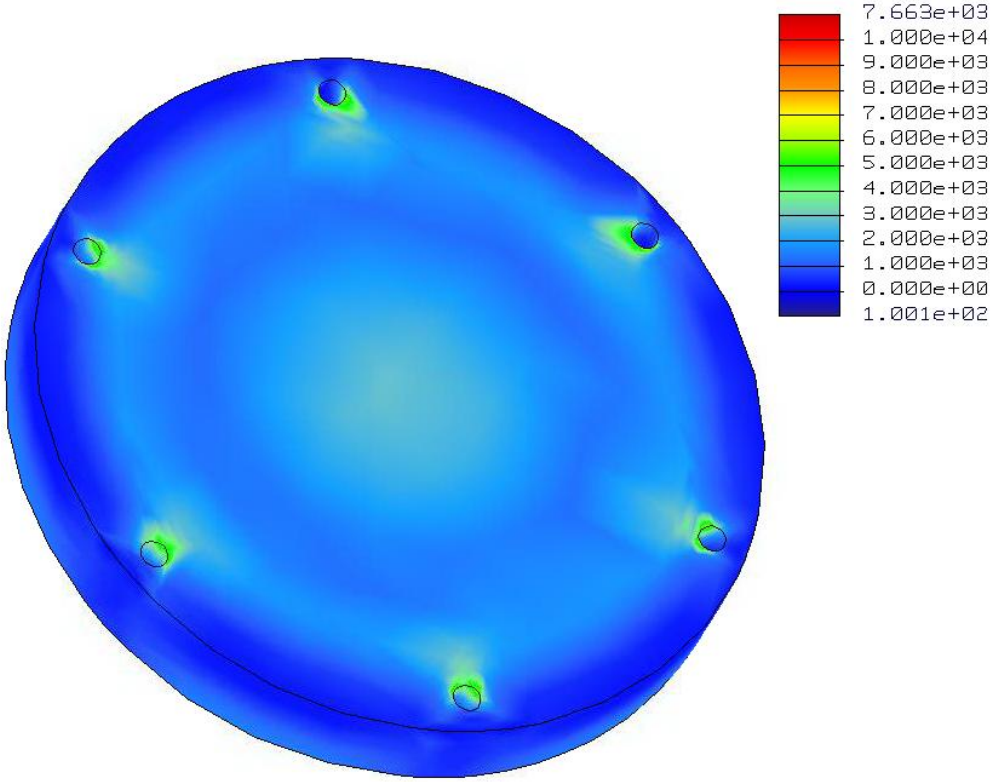

Figure 43 - FEA results for PIC-2 lid

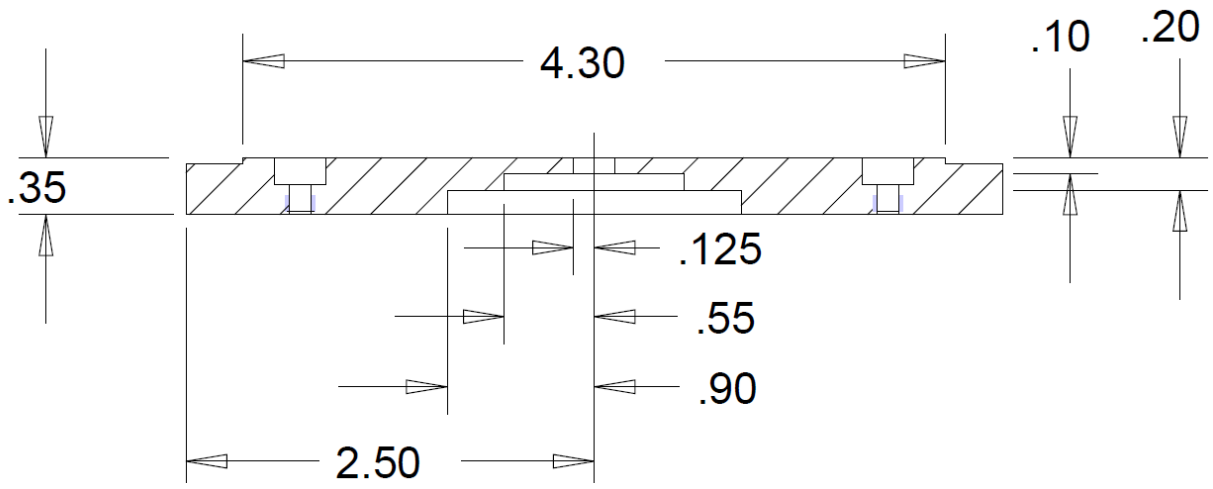

Figure 44 - Dimension drawing for 316 stainless steel base.

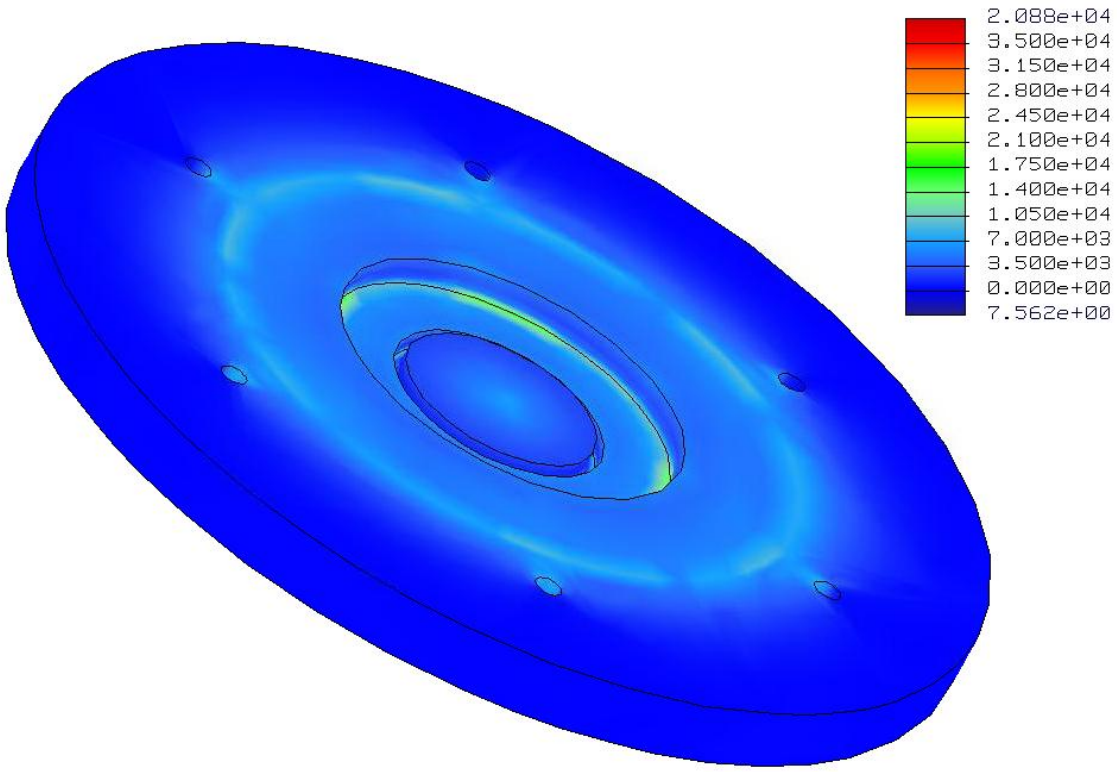

Figure 45 - FEA for base and quartz view port.

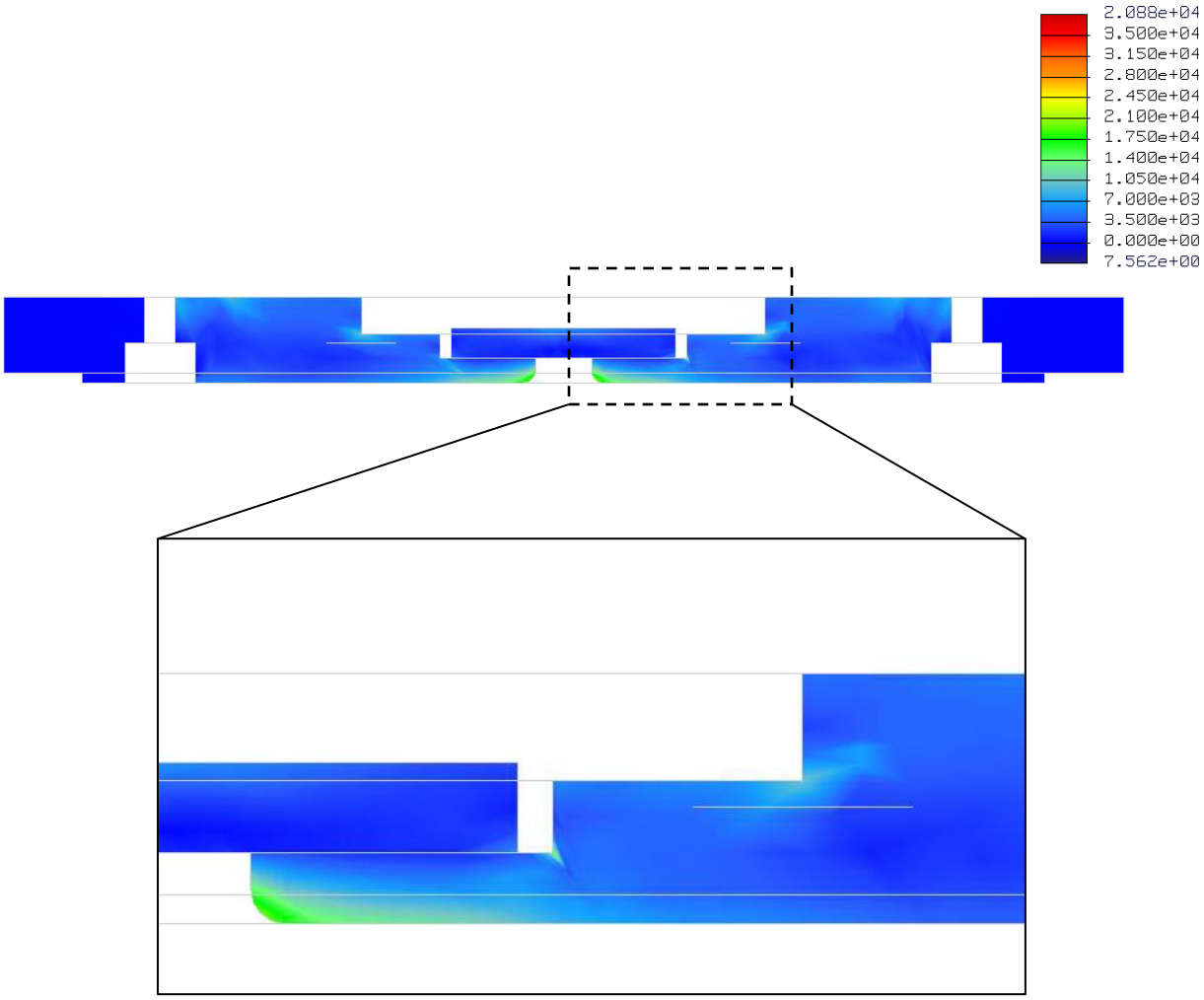

Figure 46 - Cut through middle of base and close up of stress concentration location.

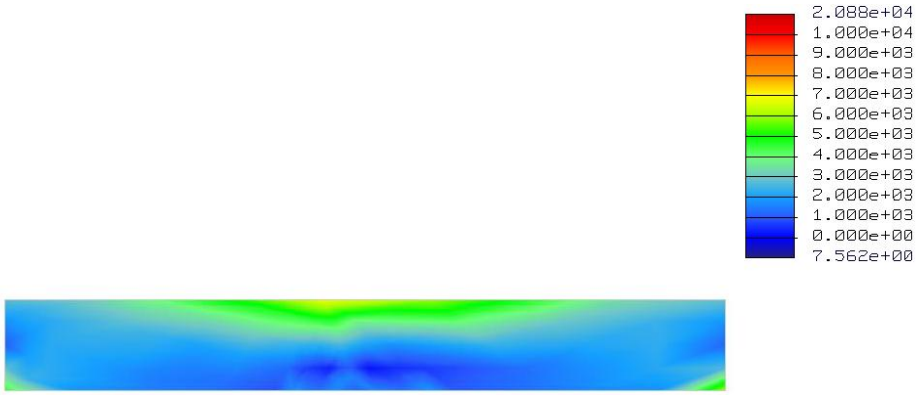

Figure 47 - Close up of FEA for quartz disc.

Appendix C: AFM Data Analysis Matlab Code

```
            % Input Parameters
fid = fopen('X1min_10percent0000.txt','r');   %open file to be read

p=256;        %Adjust this to match the number of data points recorded by AFM
L=20E-6;      %Adjust this to match scan size from AFM
j=150;        %location of 2D cross sectional plot

%%%%%%%%%%%%%%%%%%%%%%%%%%%%%%%%%%%%%%%%%%%%%%%%%%%%%%%%%%%%%%%%%%%%%%%%%%%%%%%
            % Extracts data from txt file created by Asylum AFM
for i=1:p                   %indexes from 1 to p
    A = fscanf(fid,'%f',p); %scans the data file for p number of numbers
    data(i,:)=A';           %places data into appropriate row
end
%data=data';                %This can be used to see data in other direction

%%%%%%%%%%%%%%%%%%%%%%%%%%%%%%%%%%%%%%%%%%%%%%%%%%%%%%%%%%%%%%%%%%%%%%%%%%%%%%%
            % Plot the 3D surface from AFM results
X=linspace(0,L,p);    %Length of scan divided evenly by number of scan points
Y=X;                  %Sets length of Y axis equal to x axis

h=surf(X,Y,data);                       %plots 3D surface plot
colorbar                                %adds color bar to plot
set(h,'edgecolor','none')               %hides lines on 3D plot
colormap(autumn)                        %color of plot
view(108,72)                            %orientation of plot

%%%%%%%%%%%%%%%%%%%%%%%%%%%%%%%%%%%%%%%%%%%%%%%%%%%%%%%%%%%%%%%%%%%%%%%%%%%%%%%
            % Plot a 2D cross section at specified Location j
figure(2)
plot(X,data(:,j))               %plotting 2D data for a single line of data
axis([0 L -L/2 L/2])            %setting the axis for 2D plot

%%%%%%%%%%%%%%%%%%%%%%%%%%%%%%%%%%%%%%%%%%%%%%%%%%%%%%%%%%%%%%%%%%%%%%%%%%%%%%%
            % Spectrum Analysis
nfft= 2^(nextpow2(length(X))+5);    %Use next highest power of 2 greater than
                                    %or equal to length(X) to calculate FFT.

fftx = fft(data,nfft);              %Take fft, padding with zeros so that
                                    %length(fftx)is equal to nfft

NumUniquePts = ceil((nfft+1)/2);    %Calculate the number of unique points

fftx = fftx(1:NumUniquePts);        %FFT is symmetric, throw away second half

mx = abs(fftx)/length(X);           %Take the magnitude of fft of x and scale
                                    %the fft so that it is not a function of
                                    %the length of X

mx = mx.^2;                     %Take the square of the magnitude of fft of X.

 %Since we dropped half the FFT, we multiply mx by 2 to keep the same energy.
 %The DC component and Nyquist component, if it exists, are unique and
```

```
 %should not be multiplied by 2.
if rem(nfft, 2) %odd nfft excludes Nyquist point
  mx(2:end) = mx(2:end)*2;
else
  mx(2:end -1) = mx(2:end -1)*2;
end

f = (0:NumUniquePts-1)*p/nfft;      %This is an evenly spaced frequency
                                    %vector with NumUniquePts points.

f=L./f;                             %Converts from frequency to wavelength
mx=(mx/sum(mx));

figure(3)                           %Generate the plot, title and labels.
plot(f,mx);
axis([0 1e-5 0 (max(mx)*1.1)])      %Scales the axis appropriately for the
                                    %given data
title('Spectrum Analysis of PDMS sample');
xlabel('Wavelength (meter)');

[p,f2]=max(mx);
wavelength=f(f2);
pmax=p;

text(wavelength,pmax,['\leftarrow Wavelength =
',num2str(wavelength)],'FontSize',14)

%%%%%%%%%%%%%%%%%%%%%%%%%%%%%%%%%%%%%%%%%%%%%%%%%%%%%%%%%%%%%%%%%%%%%%%%%%%%%%%
        %Find Max Curvature
[o,I]=min(data(:,j));
P1=[data((I-1),j),X(I-1)];
P2=[o,X(I)];
P3=[data((I+1),j),X(I+1)];
Radius_of_Curvature = 1/(2*det([P2-P1;P3-P2])/(norm(P2-P1)*norm((P3-
P2)*norm(P3-P1))))

%%%%%%%%%%%%%%%%%%%%%%%%%%%%%%%%%%%%%%%%%%%%%%%%%%%%%%%%%%%%%%%%%%%%%%%%%%%%%%%
        %Find amplitude
Amplitude=max(data(:,j))-o
```